

MOLECULAR SIMULATION AND EXPERIMENTAL STUDIES
ON STRUCTURES AND PROPERTIES OF POLYMER
NANOCOMPOSITE ELECTROLYTE



A Thesis Submitted in Partial Fulfillment of the Requirements for the
Degree of Master of Science in Chemistry
Suranaree University of Technology
Academic Year 2023

การจำลองระดับโมเลกุลและการศึกษาเชิงทดลองเกี่ยวกับโครงสร้างและ
คุณสมบัติของอิเล็กโทรไลต์แบบพอลิเมอร์นาโนคอมโพสิต



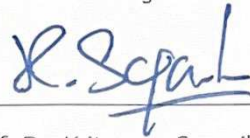
นางสาวกนกพร เรืองศรี

วิทยานิพนธ์นี้เป็นส่วนหนึ่งของการศึกษาตามหลักสูตรปริญญาวิทยาศาสตรมหาบัณฑิต
สาขาวิชาเคมี
มหาวิทยาลัยเทคโนโลยีสุรนารี
ปีการศึกษา 2566

MOLECULAR SIMULATION AND EXPERIMENTAL STUDIES ON STRUCTURES
AND PROPERTIES OF POLYMER NANOCOMPOSITE ELECTROLYTE

Suranaree University of Technology has approved this thesis submitted in partial fulfillment of the requirements for a Master's Degree.

Thesis Examining Committee



(Prof. Dr. Kritsana Sagarik)

Chairperson



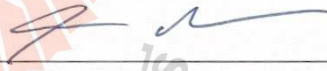
(Assoc. Prof. Dr. Visit Vao-soongnern)

Member (Thesis Advisor)



(Assoc. Prof. Dr. Kamonwad Ngamchuea)

Member



(Assoc. Prof. Dr. Chaiwat Ruksakulpiwat)

Member



(Assoc. Prof. Dr. Yupaporn Ruksakulpiwat)

Vice Rector for Academic Affairs

and Quality Assurance



(Prof. Dr. Santi Maensiri)

Dean of Institute of Science

กนกพร เรื่องศรี : การจำลองระดับโมเลกุลและการศึกษาเชิงทดลองเกี่ยวกับโครงสร้างและคุณสมบัติของอิเล็กโทรไลต์แบบพอลิเมอร์นาโนคอมโพสิต (MOLECULAR SIMULATION AND EXPERIMENTAL STUDIES ON STRUCTURES AND PROPERTIES OF POLYMER NANOCOMPOSITE ELECTROLYTE) อาจารย์ที่ปรึกษา : รองศาสตราจารย์ ดร.วิไลษฐ์ แวสูงเนิน, 101 หน้า.

คำสำคัญ: การจำลองระดับโมเลกุล, การตกผลึก, นาโนฟิลเลอร์

วิทยานิพนธ์นี้มีการใช้ทั้งการจำลองระดับโมเลกุลและการทดลองเพื่อศึกษาปัญหาเกี่ยวกับปัจจัยสำคัญในการควบคุมการตกผลึกและการนำไอออนิกของอิเล็กโทรไลต์นาโนคอมโพสิตพอลิเมอร์ วิทยานิพนธ์นี้มีสี่ส่วน หัวข้อแรกคือการศึกษาเชิงทดลองเกี่ยวกับผลของการเติมนาโนฟิลเลอร์ต่อการตกผลึกและสัญญาณวิทยาของพอลิเอทิลีนออกไซด์ หรือ PEO ที่มีน้ำหนักโมเลกุลสูง โดยการเติมซิลิกานาโนฟิลเลอร์ลงในพอลิเมอร์ PEO ซิลิกานาโนฟิลเลอร์ที่เติมลงไปนั้นประกอบด้วยซิลิกาปกติที่ไม่มีการดัดแปลง (SiO_2), ซิลิกาที่เคลือบด้วยสารคู่ควบไซเลน (SiI-SiO_2), ซิลิกาที่ดัดแปลงด้วยหมู่อะมิโน (A-SiO_2), โพลีฮีตรอลโอลิโกเมอร์ซิลิโคนออกเซน (POSS) และ มอนต์มอริลโลไนต์ (MMT) จากผลการทดลอง MMT สามารถทำหน้าที่เป็นสารหน่วงที่ดีในการตกผลึกของพอลิเมอร์ คาดว่าเป็นเพราะพอลิเมอร์สามารถเข้าไปแทรกตัวในชั้นของ MMT

ส่วนที่สองของวิทยานิพนธ์ มีการใช้การจำลองระดับโมเลกุลเพื่อศึกษาพฤติกรรมการตกผลึกของพอลิเอทิลีน (PE) แบบจำลองมอนติคาร์โลอย่างหยาบของ PE นาโนคอมโพสิตได้พัฒนาขึ้นเพื่อศึกษาผลกระทบของรูปร่างนาโนฟิลเลอร์ (ทรงกลม, แผ่น, แท่ง) เมื่อดูการตกผลึกของ PE พอลิเมอร์นาโนคอมโพสิตที่เติมนาโนฟิลเลอร์แบบแท่งและแบบแผ่นมีแนวโน้มที่จะกระตุ้นให้เกิดการก่อตัวของผลึกได้รวดเร็วและระเบียบมากขึ้นโดยเฉพาะอย่างยิ่งสำหรับนาโนฟิลเลอร์แบบแผ่น ในทางตรงกันข้าม PE นาโนคอมโพสิตที่ใส่นาโนฟิลเลอร์แบบทรงกลมจะมีการตกผลึกช้าลงและมีสัดส่วนความเป็นทรานส์ต่ำกว่า ซึ่งส่งผลให้โครงสร้างมีความเป็นระเบียบน้อยกว่า

นอกจากนี้การจำลองระดับโมเลกุลยังใช้เพื่อตรวจสอบพฤติกรรมของสายโซ่พอลิเมอร์ที่ถูกจำกัดอยู่ระหว่างกำแพงฟิลเลอร์แบบแผ่นทั้งหมดสองแผ่นซึ่งมีแรงดึงดูดระหว่างพื้นผิวกำแพงและพอลิเมอร์ที่แตกต่างกัน สำหรับฟิล์ม PE ที่มีแรงดึงดูดระหว่างผนังพอลิเมอร์กับผนังที่แข็งแรง ความหนาแน่นในบริเวณกลางฟิล์มจะลดลง และพอลิเมอร์มีแนวโน้มที่จะเคลื่อนที่มาอยู่ใกล้กับพื้นผิวผนัง สำหรับคุณสมบัติไดนามิก พอลิเมอร์ในพื้นที่ด้านในมีความคล่องตัวของโซ่ค่อนข้างเร็วกว่าเนื่องจากมีความหนาแน่นต่ำกว่า ไดนามิกของพอลิเมอร์ลดลงอย่างมากจากการดึงดูดจากพื้นผิวผนัง

ส่วนสุดท้ายของวิทยานิพนธ์ มีการใช้การจำลองโมเลกุลแบบมัลติสเกลเพื่อศึกษาเกี่ยวกับ โยสต์พอลิเมอร์ชนิดใหม่ที่สามารถนำมาทำเป็นพอลิเมอร์อิเล็กโทรไลต์ พอลิเมอร์ดังกล่าวคือ พอลิโพรพิลีนออกไซด์ หรือ PPO เป็นพอลิเมอร์ออสัญฐานและที่น่าสนใจเนื่องจากมีโครงสร้างคล้ายกับ PEO เป็น $-\text{CH}_2\text{CH}(\text{CH}_3)\text{O}-$ เมื่อผสมเกลือ LiSCN และ KSCN ลงใน PPO โครงสร้างการละลายและ ไดนามิกของไอออนของอิเล็กโทรไลต์ PPO/LiSCN และ PPO/KSCN ได้รับการศึกษาโดยใช้การ จำลองแบบทางพลวัตเชิงโมเลกุล ผลที่ได้แสดงให้เห็นว่าไอออน Li^+ แสดงการแพร่กระจายเร็วกว่า K^+ ในทางกลับกัน K^+ มีโครงสร้างการละลายที่จับกับออกซิเจนได้ดีกว่า Li^+



สาขาวิชาเคมี
ปีการศึกษา 2566

ลายมือชื่อนักศึกษา กนกพร เรืองศรี
ลายมือชื่ออาจารย์ที่ปรึกษา วิชัย เกตุพันธ์

KANOKPORN RUEANGSRI : MOLECULAR SIMULATION AND EXPERIMENTAL STUDIES ON STRUCTURES AND PROPERTIES OF POLYMER NANOCOMPOSITE ELECTROLYTE THESIS ADVISOR : ASSOC. PROF. VISIT VAO-SOONGNERN, Ph.D. 101 PP.

Keyword: Molecular simulation, crystallization, nanofiller

Both molecular simulation and experiment were employed to study the fundamental factors to control the crystallization and ionic conductivity of polymer nanocomposite electrolytes. There are four parts in this thesis. The first topic is the experimental study on the effect of adding nanofillers on the crystallization and morphology of high molecular weight poly(ethylene oxide), PEO. Five types of silica-based nanofiller and PEO were studied including unmodified silica (SiO_2), silica treated with silane coupling agents ($\text{Si}-\text{SiO}_2$), silica modified with amino groups ($\text{A}-\text{SiO}_2$), Polyhedral Oligomeric Silsesquioxane (POSS) and Montmorillonite (MMT). From the results, MMT can act as a good retarding agent for polymer crystallization assuming that intercalation occurs.

For the second part of the thesis, molecular simulation was employed to study the crystallization behavior of polyethylene (PE). A Monte Carlo simulation of coarse-grained models of PE nanocomposites was developed to study the effect of nanofiller shapes (nanosphere, nanoplate and nanostick) on polymer crystallization. PE nanocomposites filled with nanostick and nanoplate tend to induce earlier crystalline formation and have more ordered structures, especially nanocomposites with nanoplate filler. In contrast, PE nanocomposites filled with nanospheres exhibit slower crystallization with a lower amount of trans fraction and, as a result, form less ordered structures.

Next, molecular simulation was also used to investigate the behavior of dense polymer chains confined between two nanoplates with different polymer-surface interactions. For PE films with stronger polymer-wall interaction, densities in the bulk region are decreased and the chains tend to stay close to the wall surface. For dynamic properties, chains in the inner region have relatively faster chain mobility due to lower

density. Chain dynamic decreases significantly due to attractive interaction with the wall surface.

In the final part of the thesis, multiscale molecular simulation was used to create the amorphous structure of a new polymer host for electrolytes. Poly(propylene oxide), PPO, is a fully amorphous polymer with a repeating unit similar to PEO as $-\text{[CH}_2\text{CH(CH}_3\text{)O]}-$. Upon mixing LiSCN and KSCN salt with the PPO matrix, the solvation structures and ion dynamics of PPO-KSCN electrolytes were studied by molecular dynamic (MD) simulation of the fully atomistic models. Li^+ ions show faster diffusion than K^+ . On the other hand, K^+ exhibits a stronger solvation structure than Li^+ .



School of Chemistry
Academic Year 2023

Student's Signature กนกพร เว็ลล์ตรี
Advisor's Signature วิชัย วัฒนกุล

ACKNOWLEDGEMENTS

My sincere gratitude goes out to Associate Professor Dr. Visit Vao-soongnern, my adviser, for all of his support and inspiration. I genuinely appreciate all of the learning opportunities he has provided for me. This project could not be completed without the support of my classmates. I cannot express enough thanks to them. I would like to thank DPST scholarship for supporting my study at Suranaree University of Technology (SUT). I thank SUT for providing the working space and computer resources for this research project.

Special thanks to Prof. Go Matsuba, Department of Polymeric and Organic Material Engineering (DPOME), Yamagata University, Japan, for his valuable suggestions, instruments and good experiences. I would like to express my gratitude to the members of the Laboratory of Computational and Applied Polymer Science (LCAPS) as well as all graduate students at the School of Chemistry, SUT, for their support and help in making this memorable experience.

Lastly, I would want to thank my wonderful family for their love, encouragement, and belief.

Kanokporn Rueangsri

CONTENTS

	Page
ABSTRACT IN THAI	I
ABSTRACT IN ENGLISH	III
ACKNOWLEDGEMENTS	V
CONTENTS	VI
LIST OF TABLES	IX
LIST OF FIGURES	X
LIST OF ABBREVIATIONS	XIV
CHAPTER	
I INTRODUCTION	1
1.1 Research objectives.....	3
1.2 Scope and limitation	3
1.2.1 Experiments	3
1.2.2 Molecular Simulation	4
II LITERATURE REVIEWS	5
2.1 Experiment: Effect of Si-based nanofillers	5
2.2 Coarse-grained polymer nanocomposite models: Effect of nanofiller shapes on polymer crystallization from the melts	6
2.3 Coarse-grained polymer nanofilm models between impenetrable walls: Effect of surface affinity	9
2.4 Multiscale simulation of Poly(propylene oxide).....	10
III RESEARCH METHODOLOGY	14
3.1 Experiment: Effect of Si-based nanofillers	14
3.1.1 Apparatus	14
3.1.2 Chemicals	14
3.1.3 Sample preparation	14
3.1.4 Differential Scanning Calorimetry (DSC)	15

CONTENTS (Continued)

	Page
3.1.5 Polarized optical microscopy (POM)	15
3.1.6 Small-angle X-ray scattering (SAXS)	16
3.2 Coarse-grained polymer nanocomposite models: Effect of nanofiller shapes on polymer crystallization from the melts	17
3.2.1 Monte Carlo simulation (MC)	17
3.2.2 Nanocomposite Models with different nanofiller shapes	20
3.3 Coarse-grained polymer nanofilm models between impenetrable walls: Effect of surface affinity	23
3.3.1 Nanofilm models	23
3.4 Multiscale simulation of Poly(propylene oxide).....	24
3.4.1 Rotational Isomeric State (RIS) model	24
3.4.2 Long-Range Interaction	26
3.4.3 Monte Carlo simulation of coarse-grained PPO model	27
3.4.4 Reverse-mapping procedure of PPO to fully atomistic model ...	27
3.4.5 System Description	29
IV RESULTS AND DISCUSSION	30
4.1 The Effect of Adding Si-based Nanofillers on Polyethylene Oxide	30
4.1.1 Polarized Optical Microscopy (POM)	30
4.1.2 Differential Scanning Calorimeter (DSC).....	35
4.1.3 Small Angle X-ray Scattering (SAXS)	40
4.2 Coarse-grained polymer nanocomposite models: Effect of nanofiller shapes on polymer crystallization from the melts	41
4.2.1 Equilibration	41
4.2.2 Energy	43
4.2.3 Conformation	45
4.2.4 Chain dimension	47
4.2.5 Global orientation order parameter	51

CONTENTS (Continued)

	Page
4.2.6 Bond orientation correlation function	53
4.3 Coarse-grained polymer nanofilm models between impenetrable walls:	
Effect of surface affinity	55
4.3.1 Chain dynamics and structural relaxation	55
4.3.2 Density profiles	60
4.3.3 Bond orientation	64
4.3.4 Chain properties	65
4.3.5 Chain orientation.....	68
4.3.6 Energetics	69
4.4 Monte Carlo simulation of coarse-grained PPO model	71
4.4.1 Structural equilibration	71
4.4.2 Conformational dependent properties of PPO	73
4.4.3 Chain dimension	74
4.4.4 Conformational statistics	75
4.4.5 Solubility Parameters	78
4.4.6 Structures	79
4.4.7 Scattering	80
4.4.8 Dynamics of alkaline metal salts in PPO.....	82
4.4.9 Structure of alkaline metal salts in PPO	83
V CONCLUSION	85
REFERENCES	87
APPENDIX	96
CURRICULUM VITAE	101

LIST OF TABLES

Table	Page
3.1 Parameters for polymer-polymer and polymer-nanofiller interaction	22
3.2 Description of the simulated systems	22
3.3 Energy parameters and geometry for two RIS models of PPO	26
3.4 The simulation's charge parameters.....	29
4.1.1 Growth rate of polymer nanocomposite with 10% filler at 52°C	35
4.1.2 Half-time of polymer nanocomposite with 10% filler	38
4.2.1 The mean square end-to-end distance and the mean square radius of gyration for PE chains in the bulk and nanocomposites with different nanofiller geometry	50
4.3.1 The mean square end-to-end vector, the mean square radius of gyration, the ratio of three principal axes, the acylindricity and asphericity of confined polymer chains between two walls	66
4.4.1 Comparison of various PPO conformation-dependent characteristics calculated and actual values	74
4.4.2 The mean square end-to-end distance, The mean square radius of gyration and the characteristic ratio (C_n) of PPO models	75
4.4.3 Population of the conformational states for PPO models	78
4.4.4 Parameter characterizing the first peak of RDFs	84

LIST OF FIGURES

Figure	Page
2.4.1 Rotational Isomeric State (RIS) model by Abe (1979)	11
2.4.2 9 x 9 matrices for bond a, b and c (C-O, O-C and C-C, respectively).....	12
3.1 Differential Scanning Calorimetry (DSC) instrument	15
3.2 Optical microscopy (POM) instrument	16
3.3 Small angle X-rays scattering (SAXS) instrument	16
3.4 Transition from diamond lattice to <i>SNND</i> lattice.....	17
3.5 Polyethylene chain represented on the <i>SNND</i> lattice and its detailed conformation corresponding to the diamond lattice	19
3.6 The geometry of nanofillers used in this simulation S1-nanostick S2-nanoplate and S3-nanosphere	23
3.7 The reduction of 9 x 9 matrices	25
3.8 A particular snapshot from the coarse-grained PPO Monte Carlo simulation on the <i>2nnd</i> lattice.....	28
3.9 Specific snapshot from the Monte Carlo simulation of fully atomistic PPO on the <i>2nnd</i> lattice with the addition of (a) LiSCN and (b) KSCN	28
4.1.1 PEO/SiO ₂ nanocomposite film optical micrographs using crossed polarizers during isothermal crystallization at 52°C	30
4.1.2 Spherulite radius plots for SiO ₂ /PEO nanocomposites versus time with different crystallization temperatures	31
4.1.3 Plots of logarithm of spherulite growth rate versus crystallization temperature for SiO ₂ /PEO nanocomposites as a function of SiO ₂ content	32
4.1.4 Optical micrographs of PEO/SiO ₂ nanocomposite films after isothermal crystallization at 52 °C with crossed polarizers	33
4.1.5 Plots of spherulite radius versus time for PEO nanocomposites at 52°C	34
4.1.6 DSC thermograms at various cooling rates: 2 °C/min, 4 °C /min and 8 °C /min	36

LIST OF FIGURES (Continued)

Figure	Page
4.1.7 Plots of X_t versus time for crystallization of at various cooling rates.....	37
4.1.8 Plots of $t_{1/2}$ versus scan rate	39
4.1.9 Semicrystalline PEO with silica-base nanofiller Lorentz-corrected SAXS as a function of the scattering vector, q	40
4.2.1 The orientational auto-correlation function of (a) polymer chains and (b) bonds, the mean-squared displacement of (c) polymer chains and (d) individual monomers at 298 K	43
4.2.2 (a) Intramolecular and (b) intermolecular energy of PE chains in bulk and PNC at 473 K, 400 K, 350 K and 298 K	44
4.2.3 The final snapshots of PE chains (nanofillers are removed for clarity) at 298 K after 100 million MCS run for (a) S0-bulk (b) S1-nanostick (c) S2-nanoplate and (d) S3-nanosphere systems	45
4.2.4 The evolution of <i>trans</i> conformation of PE chains in the neat bulk and with nanofillers of different geometry at 473 K, 400 K, 350 K and 298 K	46
4.2.5 The evolution of (a) the mean square radius of gyration (b) the mean square end-to-end distance (c) the ratio of the mean square end-to- end distance and the mean square radius of gyration (d) the largest component of the mean square radius of gyration for PE chains.....	49
4.2.6 The evolution of the global orientation order parameter of PE chains in the bulk and PNCs with different nanofillers	52
4.2.7 Intramolecular bond orientation as a function of the separated bond index at 298 K	53
4.2.8 Local intermolecular bond orientation correlation functions of PE chains in the neat bulk and nanocomposites at 298 K	54
4.3.1 (a) The overall mean square displacement of the chain center of the mass (MSD) (b) in the parallel direction to the wall, MSD_{xy} (c) in the perpendicular direction to the wall, MSD_z and (d) the orientation autocorrelation functions (OACF) of the chain end-to-end vector	57

LIST OF FIGURES (Continued)

Figure	Page
4.3.2 Fraction of the centers of mass of polymer chains which stay in their original bin in the middle and interface regions as a function of MCS	57
4.3.3 Normalized end-to-end vector autocorrelation function of the chains starting in middle and interface regions as a function of MCS	58
4.3.4 Apparent diffusivity in different bins of polymer film	60
4.3.5 The representative snapshots of polymer-wall systems with different polymer-wall interactions	61
4.3.6 Density profiles of confined PE nanofilms with different wall interactions	62
4.3.7 The distribution of chain center of mass for the confined polymers between two interactive walls	62
4.3.8 (a) Normalized end-bead and (b) middle-bead densities in the confined polymer films between two interactive walls	63
4.3.9 The local orientation of (a) the middle bonds and (b) the end bonds of PE chains with different wall interaction	64
4.3.10 (a) The parallel (XY) and (b) the perpendicular (Z) components of the mean-squared radius of gyration and (c) the longest and the shortest principal axes of polymer chains	67
4.3.11 The order parameter of (a) the longest and (b) the shortest principal axes of polymer chains	69
4.3.12 The average (a) intramolecular and (b) intermolecular energies of the confined polymers	70
4.4.1 (a) The mean-square displacement for the chain center of mass and (b) The orientation autocorrelation functions (OACF)	72
4.4.2 Example of the snapshot of (a) coarse-grained and (b) fully atomistic PPO models	73
4.4.3 Population of the backbone torsional angles for the CG and fully atomistic PPO models	77

LIST OF FIGURES (Continued)

Figure	Page
4.4.4 The total radial distribution function for different pairs of elements	79
4.4.5 (a) X-rays and (b) Neutron scattering for PPO model	81
4.4.6 The mean square displacement of alkaline metal salts in PPO	82
4.4.7 Ion-atoms radial distribution functions in PPO chains	83



LIST OF ABBREVIATIONS

PE	Polyethylene
PEO	Poly(ethylene oxide)
PPO	Poly(propylene oxide)
SPEs	Solid polymer electrolytes
SAXS	Small Angle X-ray Scattering
DSC	Differential Scanning Calorimetry
POM	Polarized optical microscopy
POSS	Polyhedral Oligomeric Silsequioxane
MMT	Montmorillonite
Sil-SiO ₂	Silica treated with silane coupling agents
A-SiO ₂	Silica modified with amino group
RIS	Rotational Isomeric State
LJ	Lennard-Jones
$\langle R_E^2 \rangle$	Mean Square End-to-End distance
$\langle R_g^2 \rangle$	Mean Square Radius of Gyration
$\langle m(t).m(0) \rangle$	Orientational autocorrelation function of bond vector
$\langle R(t).R(0) \rangle$	Chain end-to-end vector orientational autocorrelation
2 nd	The Second Nearest Neighbor Diamond
Å	Angstroms
k _B	Boltzman constant
B ₂	Second Virial Coefficient
C _n	Characteristic Ratio
K	Kelvin
L ₁ , L ₂ , L ₃	Primary Axis, Secondary Axis, Tertiary Axis
LJ	Lennard-Jones
MC	Monte Carlo
MCS	Monte Carlo Step
nm	nanometer

LIST OF ABBREVIATIONS (Continued)

MSD	Mean Square Displacement
Mw	Weight average molecular weight
OCAF	Orientation Autocorrelation Function
PCF	Pair Correlation Function
R_g	Radius of gyration
S_G	Global orientation order parameter
S_L	Local intermolecular
$t_{1/2}$	Crystallization half-time



CHAPTER I

INTRODUCTION

In many facets of our lives, energy is essential. A rising area of academic research and industrial application is energy generation and storage because of the modern world's continually expanding energy needs. A device used for electrochemical energy storage is a battery. Each contains positive and negative electrodes, both of which are submerged in an electrolyte, either liquid or solid.

Polymers are materials made up of several repeating subunits organized into enormous molecules (Billmeyer, 1984). In addition to their significance in a broad range of industrial applications, they are fascinating from a basic scientific perspective as well. Polymeric materials are generally recognized for their insulating qualities. In addition, they can be modified to become materials that are partially conductive in batteries. After being altered by dissolving alkali salts in an appropriate polymer matrix, solid polymer electrolytes (SPEs) reveal an ionic conductivity. Battery, fuel cell, electrochromic device, sensor, and electrochemical switching are merely some of the many electrochemical uses for SPEs (Quartarone, 1998; Song, 1999; Dias, 2000).

Prior to now, the majority of SPE research has employed matrix polymers made of poly(ethylene oxide), PEO, and its variants (Bruce, 1995; Chintapalli, 1996). Both the flexible macromolecular structure of PEO and its ether coordination sites provide efficient ionic transport and contribute to the dissociation of ions in polymeric materials (Nishimoto, 1999). Unfortunately, since crystalline domains obstruct ionic transport, PEO-based polymer electrolytes exhibit poor ionic conductivity at room temperature. In polymer electrolytes, ionic conductivity and the movement of ions depend on the amorphous phase due to the fact that ionic mobility is accompanied by polymer chain mobilities (Dias, 2000). SPEs can be made more ionic conductive by decreasing their crystalline domains and enhancing their ionic transport on main-chain segmental movements (Song, 1999). In this thesis, we attempt to reduce the quantity of polymer crystallinity through the incorporation of nanofiller into the polymer matrix

to create the so-called polymer nanocomposite and modify the polymer host. The structure and characteristics of polymer nanocomposite electrolytes were studied using both molecular modeling and experiments to further our understanding of these materials.

The effect of adding nanofillers on the crystallization and morphology of high molecular weight PEO was studied using thermal analysis, X-ray scattering (SAXS), differential scanning calorimetry (DSC) and polarized optical microscopy (POM). High molecular weight (4×10^6 g/mol) poly(ethylene oxide), PEO, is used as the host polymer and there are three types of silica nanofiller with different surface affinity with PEO including the unmodified silica (SiO_2), silica treated with silane coupling agents (Si-SiO_2) and silica modified with amino group (A-SiO_2). Moreover, Polyhedral Oligomeric Silsesquioxane (POSS) and Montmorillonite (MMT) were added to concern on the effect of nanofiller shape.

Related to the experimental work, the second part is about the study by molecular simulation to gain a deeper understanding of the effect of surface affinity and the shape of nanoscale fillers on the crystallization of polymer nanocomposites. Monte Carlo (MC) simulation of coarse-grained models of polyethylene (PE) nanocomposites was developed to study the effect of nanofiller shapes (nanosphere, nanoplate and nanostick) on the early stage of polymer crystallization under stepwise cooling from the melts. The “*polymer forcefield*” to describe intra- and intermolecular interaction is composed of the rotational isomeric state (RIS) model of PE and the Lennard-Jones (LJ) potential energetics of ethylene units, respectively. Crystallization is monitored using the fraction of *trans* state and the orientation order parameter at the bond and chain scale.

The behavior of dense polymer chains sandwiched between two nanofillers (walls) with various polymer-surface interactions should be studied using molecular modeling. The influence of the polymer-wall affinity (the same, more repulsion and more attraction relative to polymer-wall non-interaction) was examined using Monte Carlo (MC) simulation of coarse-grained models of polyethylene (PE) nanocomposites.

For a deeper comprehension of the conductivity and ion-polymer interaction of SPEs, the polymer's conformation is significant. Here, amorphous PPO will be the

subject of multiscale molecular simulation development. Due to the additional methyl group in the repeating unit of PEO, PPO naturally contains more amorphous phase than PEO, hence adding PPO might prevent the matrix polymer from crystallizing. The Rotational Isomeric State (RIS) theory will be examined to investigate the conformational characteristics and conformational dependent properties of polymers. This theory allowed fast and accurate calculations by producing properties specific to a single chain and a precise depiction of the conformational statistics of chains for molecules (Tao, 1999). Generate statistical weight matrices first (Sasanuma, 1995). PPO chains will then be coarse-grained and mapped onto the second nearest neighbor diamond ($2nnd$) lattice. By using the reverse mapping process to retrieve the missing atoms, fully atomistic PPO structures can eventually be produced. These atomistic PPO models will be confirmed by determining and comparing molecular and material parameters with data from experiments.

1.1 Research objectives

- 1.1.1 To gain more understanding for the effect of nanofillers/films on structural and material properties of polyether-based electrolytes
- 1.1.2 To predict structural and materials properties of polyether-based electrolytes by multiscale molecular simulation and compare to experimental data.

1.2 Scope and limitation

Here there are two different parts of research as follows:

1.2.1 Experiments

Three groups of nanofillers: montmorillonite (MMT), surface-modified nanosilica (neat, silane, NH_2) and Polyhedral oligomeric silsesquioxane (POSS) will be mixed with PEO. The crystallization and morphologies of these samples will be investigated using various techniques. The list of all instrumental characterization of polymer nanocomposite includes:

- 1.2.1.1 **Differential Scanning Calorimeter (DSC):** To evaluate polymeric material crystallization behavior.
- 1.2.1.2 **Polarized optical microscopy (POM):** Polarizing filters are used to gather significant optical property data of the polymer samples under observation.
- 1.2.1.3 **Small-angle X-ray scattering (SAXS):** to ascertain the nano- and mesoscale structure of polymer materials.

1.2.2 Molecular Simulation

- 1.2.2.1 **Coarse-grained polymer nanocomposite models:** Nanofillers with of different shapes (nanosphere, nanoplate and nanostick) will be simulated using coarse-grained polyethylene-like model which one bead represents a monomer unit i.e. $-\text{CH}_2\text{CH}_2-$ unit. The simulation will be performed using Lennard-Jones (LJ) parameter of $\epsilon/k_B = 185 \text{ K}$, $\sigma = 4.4 \text{ \AA}$ for polymer-polymer interaction
- 1.2.2.2 **Coarse-grained polymer nanofilm models:** “*polyethylene-like*” melt confined between two impenetrable walls that had different surface affinity (neutral, more attractive and more repulsive surface) will be simulated using coarse-grained model.
- 1.2.2.3 **Multiscale simulation of PPO:** The RIS models, conformational dependent properties and fraction of bond conformer will be calculated and compared with experimental data. The RIS models will be used for the next step of development the coarse-grained amorphous PPO model at bulk density. Determination of the structures *i.e.* chain dimension (R_g), structure, scattering, and dynamics will be determined.

CHAPTER II

LITERATURE REVIEWS

2.1 Experiment: Effect of Si-based nanofillers

One of the methods to enhance the ionic conductivity of SPEs is to add nanofillers. A class of hybrid materials known as polymer nanocomposites (PNCs) employs nanomaterial as the filler and polymer as the matrix. The filler includes Silicon dioxide nanoparticles (SiO_2), Polyhedral Oligomeric Silsesquioxane (POSS) and Montmorillonite (MMT).

In this work, there are three types of silicon dioxide including silicon dioxide nanoparticles (SiO_2), silicon dioxide nanoparticles treated with silane coupling agents (SiO_2 -Silane) and silicon dioxide nanoparticles surface modified with amino group (SiO_2 - NH_2). Different surfaces were modified to represent different interactions between polymer-nanofiller corresponding to my previous publication 'Monte Carlo simulation of the effect of nanofiller size and surface affinity on the crystallization of polymer nanocomposites' (Rueangsri, 2023).

One of the most efficient nanofillers and a great cross-linking compound is polyhedral oligomeric silsesquioxane (POSS). Different from most fillers, POSS is a blend of inorganic and organic components with an exterior organic substituent and an internal inorganic silicon and oxygen core ($\text{SiO}_{1.5}$)_n, which may be used to make them compatible with a wide range of polymers. POSS nanostructures have dimensions ranging from 1 to 3 nm. The molecular-level dispersion of rigid POSS in the polymers improved the conductivity, mechanical strength, and decreased combustibility when POSS nanoparticles were incorporated into the polymer (Li, 2001; Kuo, 2011; Jung, 2015; Chabane, 2022). Its large volume additionally allows it to preserve or lower the glass transition temperature (T_g) by altering the polymer chain structure and giving the polymer chains more free volume (Kwon, 2014).

In this study, POSS-poly(ethylene glycol) (POSS-PEG) has been produced by functionalizing POSS cages with ethylene glycol monomethyl ethers from Hybrid

Plastics, Incorporated. Zhang group reported on the mixing of POSS-PEG with methylcellulose or high molecular weight PEO enhanced conductivity (Zhang, 2006).

An inorganic filler with the ability to intercalate is a clay mineral. The intercalating polymer in layered clay host can produce polymer electrolyte nanocomposite, with a huge interfacial area. Higher interfacial area maintains the mechanical properties of this semi-crystalline PEO-based electrolyte while simultaneously reducing the crystallinity of PEO chains, which raises ionic conductivity. The most widely utilized multilayer silicates are Montmorillonite (MMT) which is structured as $(M_x(Al_{4-x}Mg_x)Si_8O_{20}(OH)_4)$. Tetrahedral-substituted and octahedral-substituted structures are the two types of structures seen in layered silicates. Tetrahedrally substituted layered silicates have a negative charge on their surface, which makes it easier for polymer matrices to interact with them than with octahedrally substituted material.

2.2 Coarse-grained polymer nanocomposite models: Effect of nanofiller shapes on polymer crystallization from the melts

Polymer nanocomposites (PNC) are hybrid materials that can exhibit high performance and better properties compared to conventional polymeric materials (Sheng, 2004; Coleman, 2006; Koo, 2006; Allegra, 2008). Investigation of structures and properties of PNC has been performed for both fundamental studies and technological applications with good progress over the past two decades (Mittal, 2012; Kumar, 2017; Fu, 2019). These additive nanofillers can come in different quantities, sizes and shapes which can induce enhanced properties of the final product. Although the reinforcement mechanism for property improvement is still on the way for investigation, it is generally accepted that the nanofiller-polymer interaction, the homogeneous distribution of nanofillers in the polymer matrix and the interparticle spacings are crucial factors (Flandin, 2001; Anderson, 2010).

In general, nanofillers can be categorized into three types according to their geometry: spherical, cylindrical and layered. Most early studies are based on layered fillers especially natural clays because of their low cost and usually have high

reinforcement capability, better barrier properties and low flammability (Pinnavaia, 2000). Carbon nanofiber and nanotubes are examples of cylindrical nanofillers with remarkable mechanical properties and act as promising reinforcements in enhancing the mechanical properties of PNC (Sandler, 2003). Nanofillers with spherical shapes such as silica, alumina, and zinc oxide are normally used in the preparation of PNC because they can be optically transparent, and improve mechanical/rheological properties (Ajayan, 2003). When the chain dimension is comparable to the nanofiller size, the geometric confinement can have influenced the orientation of the polymer chains and molecular mobility (Solar, 2015). Specific polymer-nanofiller interactions can also impact the chain conformation and orientation near the interface which should be governed by the nature of chain chemistry and the characteristics of the nanofiller (Barrera, 2022).

Nanofillers can significantly influence the nature of the polymer crystallization in PNC (Nie, 2011). Nanofillers with optimum size and a suitable amount can speed up the heterogeneous nucleation of polymer near the interface. There are some past reports on experimental studies for the effect of nanofiller characteristics on the chain crystallization in PNC. For example, the crystallization of isotactic propylene (iPP) caused by shear stress can be affected by the shape of the coloring agent used. The planar shape of Cu-phthalocyanine (CuPc) colorant leads to different morphology from those mixed with the spherical shape of sodium aluminosulfosilicate (Zhu, 2009). Another investigation was focused on the effect of nanofiller composition, size and shape (mainly spherical and oblate particles) on the crystallization of iPP with the nucleating particles in quiescent. Experimental results suggest that when the oblate ratio of the particles becomes large, the crystallization time is reduced (D'Haese, 2013). When carbon-based nanofillers are added to the polymer matrix, they can induce nucleation and speed up the crystal formation (Moniruzzaman, 2006). Nevertheless, there are still some remarks that the role of nanofiller addition cannot be explained completely and the role of nanoparticles on polymer crystallization remains complex.

Although experiments have been focused on various nanocomposites, the main problem is the difficulty to control the particle shape precisely which makes it more challenging to determine the impact of the shape of nanofillers during polymer

crystallization. Moreover, larger particles often form aggregates with a rough surface. On the other hand, computer modeling provided an alternative method to investigate polymer crystallization under control conditions. For example, molecular dynamic (MD) simulation was applied to determine the early stage of structural formation and there was an increase in the global order parameters after the chain elongation to some extent (Fujiwara, 1999). In addition, simulation for polymers filled with an isolated nanoparticle shows that the crystallization is decreased with increasing nanofiller content (Yang, 2009). In addition to the MD method, Monte Carlo (MC) simulations were also applied to study the chain folding during crystallization in the solution phase (Chen, 1998). Another example is the MC simulations for polymer models in which artificial energies between two Kuhn segments had to be introduced (Hu, 2000). Because of the deficiency of the ideal models normally used in MC and the huge amount of computational time of atomic models for MD, simulation of polymer crystallization in the presence of additives is still difficult to compromise between the molecular model and the calculation time. Alternatively, simulations of the coarse-grained (CG) model that can capture the chemistry of real polymer chains and the nature of the nanofiller surface with reasonable accuracy should be able to overcome these problems (Mandal, 2017).

In this work, this simulation method is used to study the crystallization of PNC filled with a nanofiller with three different shapes (so-called nanostick, nanoplate and nanosphere) upon stepwise cooling from the melts. In particular, PNCs filled with nanofiller of comparable size with the same energetics between polymer-nanofiller and polymer-polymer interaction are studied. The conformational characteristics, intra/intermolecular structures and the chain/bond orientation of the ordered structure formed at the same crystallization temperature are determined and compared.

2.3 Coarse-grained polymer nanofilm models between impenetrable walls: Effect of surface affinity

In general, the presence of nearby solid surfaces has a substantial impact on the structure of macromolecular fluids. The solid walls modify the segment density distribution, and the scale of this solid-induced inhomogeneity must be comparable to the correlation length in the macromolecular fluid (Gennes, 1979). Therefore, only over a distance equivalent to the segment size in a melt has wall's impact on the resulting density. This solid wall-polymer matrix material may be understood as a polymer-matrix composite, whereby an amorphous polymer matrix (such as epoxies, polyesters, and polyimides) is embedded with a fiber component (such as glass, Kevlar, or graphite). Combining a polymer system with a fiber has the benefit of creating a new material with unique qualities that none of the constituent parts could have on its own.

The solid-polymer melt interface can be represented from the perspective of simulation works by a hard neutral wall (i.e., no attraction with the monomers). Two opposing variables, the loss in configurational entropy and packing constraints, define the melt structure near a hard wall. Because of the impenetrable wall, there are fewer accessible chain configurations, which leads to a decrease in configurational entropy. In an attempt to push the polymers into the bulk-like matrix and away from the interface, it generates an effective force. This effective force must compete with another force exerted by the chains in the matrix on the polymers at the interface, which tends to pack them against the wall.

The polymers in the matrix push the chains close to the wall against the interface at melt-like densities, somewhat forcing them to align parallel to the wall. Molecular dynamics simulations (Bitsanis, 1990), off-lattice Monte Carlo simulations (Kumar, 1990; Hertanto, 1990; Dickman, 1992; Yethiraj, 1994; Phan, 1995), lattice Monte Carlo (Bitsanis, 1993; Brinke, G, 1988, Pakula, 1991), and theoretical analysis (Brazhnik, 1994; Theodorou, 1988) have all been observed to have an impact on the polymer structures resulting from the interaction of density and chain entropy close to a hard wall.

The benefit of the aforementioned simulations is that appropriately specified quantities allow for the simultaneous analysis of structural (and dynamical) characteristics at the polymer-wall interface on various length scales. Among these are, for example, several profiles, such as the radius of gyration, the monomer density profile, and the chain density profile, which describe how the wall's impact progressively disappears with farther away from the wall. Whereas most of the mentioned simulations study the variation of these profiles with chain length (Lai, 1994), density (Dickman, 1992), and overall distance between the walls (Yethiraj, 1994). Though this polymer contained between the solid substrate is widely recognized for its technological significance, the variation of wall interactions with two solid barriers has received little attention. To address this challenge, the coarse-grained polymer model on the high coordination lattice has been simulated using Monte Carlo (MC) techniques, which have been used in the study of polymers confined between two impenetrable walls (Baschnagel, 2000; Doruker, 1998; Vao-soongnern, 2001; Baschnagel, 1995).

2.4 Multiscale simulation of Poly(propylene oxide)

The backbone structure of Poly(propylene oxide) (PPO) is comparable to that of PEO, and it may serve as a host polymer. Because PPO has an additional methyl group in its repeating unit compared to PEO, which makes it naturally amorphous, adding PPO might prevent the matrix polymer from crystallizing (Nishimoto, 1999). According to Ahlstrom (2000), PPO is highly flexible at room temperature and transitions to a glassy form.

For a deeper comprehension of the conductivity and ion-polymer interaction of SPEs, the polymer's conformation is important. The Rotational Isomeric State (RIS) theory will be examined in this regard to study the conformational characteristics and conformational dependent properties of polymers. This theory enabled quick and precise calculations by producing properties specific to a single chain and a precise depiction of the conformational statistics of chains for molecules (Tao, 1999). Furthermore, as polymeric materials include many polymer molecules at bulk density,

a realistic molecular model-generating technique must be developed in order to predict material characteristics.

Abe published the first Rotational Isomeric State (RIS) model of PPO in 1979. Based on the semiempirical potential energy functions for short representative segments of PPO, the study of conformational energy calculation was used to build the model. Their study was undertaken to determine the best possible set of conformational energies through critical rotational isomeric state analysis in comparison to experimentally reported molecular dimension, dipole moment, and conformation fractions about skeletal C-C bonds which were reported for isotactic PPO samples. Comparison of theoretical and experimental values of conformational energies thus derived provides a quantitative estimate of the *gauche* oxygen effect associated with PPO chain.

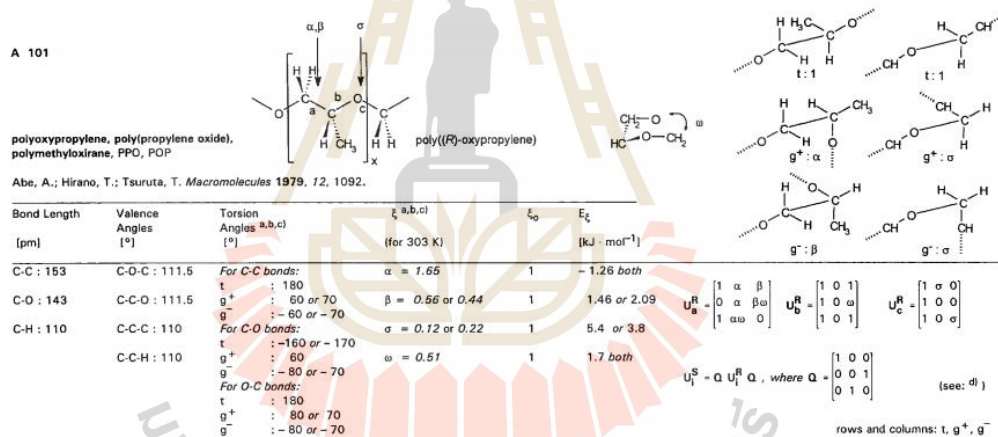


Figure 2.4.1 Rotational Isomeric State (RIS) model by Abe (1979).

In 1995, Sasanuma proposed a new RIS model to investigate the conformational characteristics of PPO based on the energy calculation of its model compound, 1,2-dimethoxypropane (1,2-DMP). The PPO chain possesses two stereochemical configurations (such as (R)- and (S)-optical forms) due to the asymmetric methine carbon, and the two *gauche* states around the skeletal C-C bond are not equivalent. Ab initio molecular orbital calculations at the MP4/6-31+G* level were performed for 1,2-DMP, and for every possible conformer in vacuo, its molecular structure was fully optimized using the Hartree-Fock (HF)/6-31G* level. The cavity radius needed for the self-consistent reaction field (SCRF) calculation (Wong, 1991) was

then estimated. The SCF and geometry optimization were performed using the default convergence conditions.

Positive values were discovered for every first-order interaction energy. However, it was discovered that the second- and third-order interaction energies, which represent unbonded C-H-O contacts, were negative. Conformational energies for the C-C bond were estimated to be $-0.3 \text{ kcal mol}^{-1}$ ($E\alpha$) for the g^+ state and $0.35\text{-}0.5 \text{ kcal mol}^{-1}$ ($E\beta$) for the g^- state by fitting the RIS analysis to the reported unperturbed dimensions and dipole moments of PPO. The characteristic ratio and dipole moment ratio of isotactic PPO were estimated using the RIS method up to third-order interactions and in good agreement with the experimental data.

The Flory (1989) RIS schemes for polymer chains are primarily based on the first- and second-order interactions with three rotating isomeric states (t, g^+ , and g^-). Then, all the statistical weight matrices assigned to the skeletal bonds are of 3×3 dimension. In particular, the latter conformer appears to be stable and highly populated. In actuality, the existence of these conformers is prevented by steric repulsion between the two terminal CH_3 groups. As a result, third-order interactions ought to be tracked.

For bonds a, b and c (C-O, O-C and C-C, respectively), inspection of the molecular model leads to 9×9 matrices of PPO as following

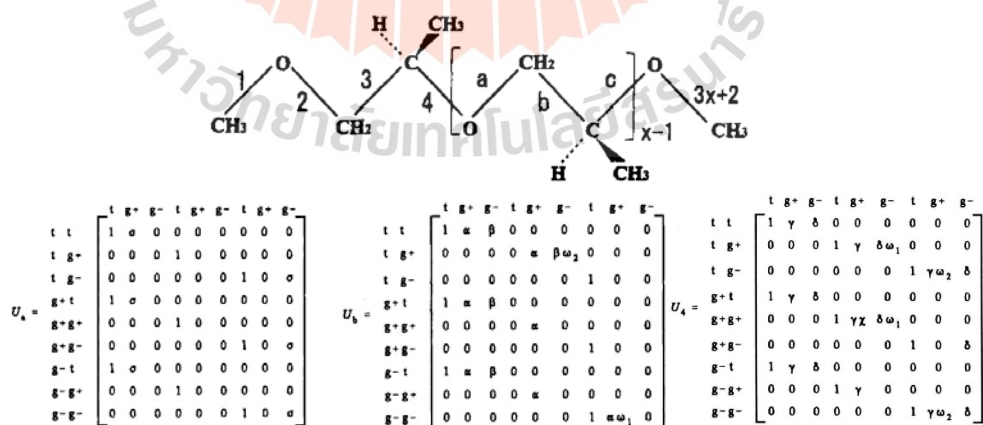


Figure 2.4.2 9×9 matrices for bonds a, b and c (C-O, O-C and C-C, respectively).

The geometrical parameters as suggested by Abe (1979) were employed in Sasanuma's study (1995) as

Bond lengths: C—C = 1.53 Å and C-O = 1.43 Å;

Bond angles: $\angle\text{COC} = \angle\text{CCO} = 111.5^\circ$ and $\angle\text{OCC} = 110^\circ$;

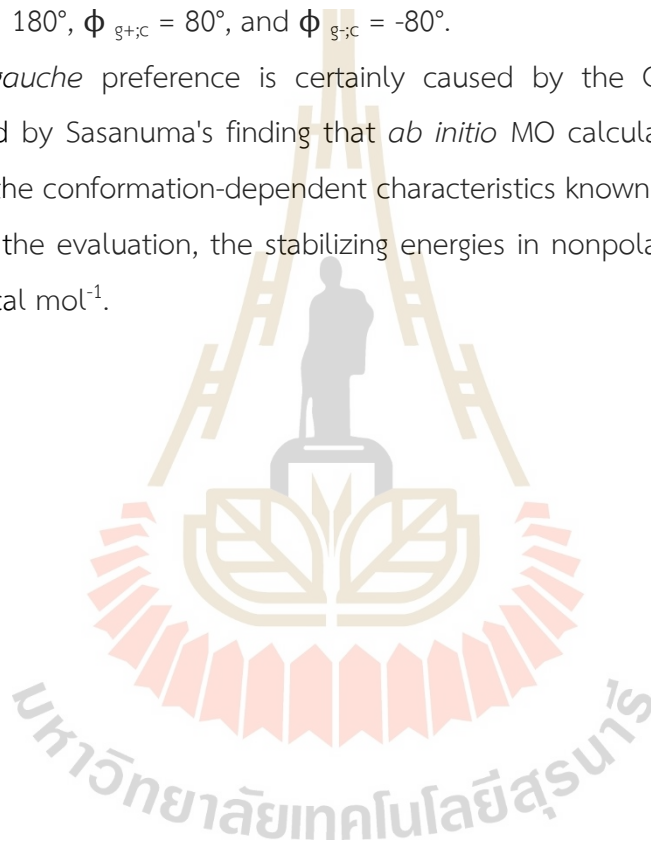
Dihedral angles:

$\phi_{t;a} = 180^\circ$, $\phi_{g+;a} = 60^\circ$, $\phi_{g-;a} = -60^\circ$,

$\phi_{t;b} = -160^\circ$, $\phi_{g+;b} = 60^\circ$, $\phi_{g-;b} = -80^\circ$,

$\phi_{t;c} = 180^\circ$, $\phi_{g+;c} = 80^\circ$, and $\phi_{g-;c} = -80^\circ$.

The *gauche* preference is certainly caused by the C-H* \cdots O attractions, as demonstrated by Sasanuma's finding that *ab initio* MO calculations may reproduce nearly all of the conformation-dependent characteristics known for 1,2-DMP and PPO. According to the evaluation, the stabilizing energies in nonpolar liquids ranged from -1.0 to -1.9 kcal mol⁻¹.



CHAPTER III

RESEARCH METHODOLOGY

3.1 Experiment: Effect of Si-based nanofillers

3.1.1 Apparatus

- Magnetic stirrer and magnetic bar
- Balance
- Vacuum oven
- Beaker

3.1.2 Chemicals

- Polyethylene oxide (PEO) Mw = 4,000,000 g/mol, (Aldrich)
- Montmorillonite (MMT), (Aldrich)
- Silicon Oxide Nanoparticles, (SSnano)
- Silicon Oxide Nanoparticles treated with silane coupling agents, (SSnano)
- Silicon Oxide Nanoparticles modified with amino group, (SSnano)
- PEG POSS cage, (Hybrid)
- Potassium thiocyanate (KSCN)
- Methanol, (QREC)

3.1.3 Sample preparation

The high molecular weight PEO (MW 4,000,000 g mol⁻¹) are dried at 50 °C under a vacuum for 24 hours. The nanofillers including neat SiO₂, A-SiO₂, Sil-SiO₂ and MMT are dispersed in a small amount of methanol using an ultrasonic bath. PEO and nanofillers (neat SiO₂, A-SiO₂, Sil-SiO₂, POSS and MMT) in a proper quantity are dissolved in methanol and vigorously agitated for 24 hours at room temperature. To aid in degassing, the solution is continuously stirred and then let to remain at room

temperature for an entire day. The gelatinous polymer solution is cast onto the glass plate to create a thin layer of the film samples. To remove the solvent, the films are dried for 24 hours at 50 °C in an oven.

3.1.4 Differential Scanning Calorimetry (DSC)

At Yamagata University in Japan's Matsuba laboratory, crystallization and nucleation were examined using a TA Instruments Perkin-Elmer Diamond differential scanning calorimeter Q2000, which was calibrated with indium for temperature and heat of fusion. Sample weights in standard aluminum pans ranged from 4.0 to 5.0 mg. To eliminate the thermal history and prevent PEO from self-seeding, the samples were kept at 90 °C for five minutes in a nitrogen environment. Non-isothermal crystallization kinetics of PEO and PEO/Silica-base nanofiller were investigated in this work. The analysis was conducted under heating rates of 20°Cmin⁻¹. The investigation was carried out at heating rates of 20°Cmin⁻¹. Then, cooling scans were performed from 90 to 30°C at speeds of 4, 6, and 8°Cmin⁻¹.



Figure 3.1 Differential Scanning Calorimetry (DSC) instrument.

3.1.5 Polarized optical microscopy (POM)

Transmission POM was used at the Matsuba laboratory at Yamagata University, Japan, utilizing an Olympus microscope BX53M (Figure 3.2), which was outfitted with a mechanism for quick sample transfer from the melting to the crystallization stage and

a cell containing silver heating stages. A digital camera was used to record image sequences. The cooling and heating scans were performed at a rate of $50^{\circ}\text{Cmin}^{-1}$ from 90°C (3 mins) to the crystallization temperature (48 and 52°C).



Figure 3.2 Optical microscopy (POM) instrument.

3.1.6 Small-angle X-ray scattering (SAXS)

Because SAXS's length scales overlap with those of semi-crystalline polymers, it is suitable for researching polymers. For semi-crystalline polymers, the correlation function analysis that follows is frequently used. The lamella d spacing and the diffraction maximum's location are connected. A MicroMax-007HF with a 40 kV tube voltage and a 30 mA tube current was used for SAXS.



Figure 3.3 Small angle X-rays scattering (SAXS) instrument.

3.2 Coarse-grained polymer nanocomposite models: Effect of nanofiller shapes on polymer crystallization from the melts

3.2.1 Monte Carlo Simulation

The coarse-grained polymer model was originally simulated using Monte Carlo methods on the second nearest neighbor diamond (*SNND* or *2nnd*) lattice by Rapold and Mattice in 1995. This broadens the observable time domain on the simulation length scale, which is highly helpful in polymer simulation. In the *SNND* simulation, the twist angle for polyethylene is restricted to the *trans* and two *gauche* states. The fast Monte Carlo technique that the *SNND* simulation employs to sample the conformational space is another benefit. Both short- and long-range interactions show the energy interaction in the *SNND* simulation. The rotating isomeric state (RIS) model serves as the foundation for short-range contact, while the virial coefficient and Leonard-Jones potential serve as the basis for long-range interaction.

3.2.1.1 Second Nearest Neighbor Diamond Lattice

The diamond lattice is an obvious option for the simulation as the torsional angles are 120 degrees and the bond angle between the three carbon atoms is about tetrahedral. Based on the diamond lattice and removed (white circle) lattice sites, the Second Nearest Neighbor Diamond (*SNND* or *2nnd*) lattice was created. A coarse-grained lattice, also known as a 'second nearest neighbor diamond lattice' is the closest arrangement of uniformly hard spheres.

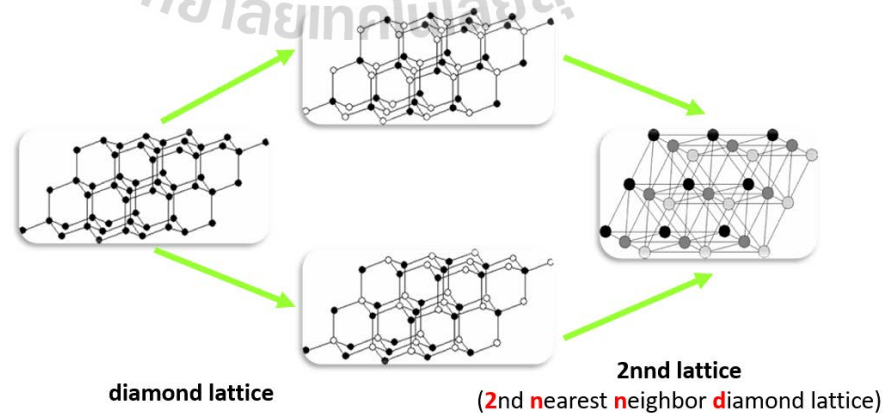


Figure 3.4 Change from diamond lattice to *SNND* lattice.

The coordination number of the diamond lattice is 4, but the *SNND* lattice has a coordination number of 12. With a 60 degree angle between the two axes, the *SNND* unit cell is a cubic that is deformed in every dimension. In n-alkane simulations, two main-chain carbon atoms and the hydrogen atoms that are connected to them, or (CH₂CH₂) units, are represented by each bead at a location on the *SNND* lattice. The *SNND* lattice spacing is set at 0.25 nm because the carbon-carbon bond length is 0.153 nm. At some point throughout the simulation, we may recover completely atomistic features by reverse mapping.

3.2.1.2 Moves on the *SNND* Lattice

On the *SNND* lattice, the Monte Carlo movements might be either local or global. On the *SNND* lattice, both kinds of motions have been applied successfully. The placement of the two bonded neighbors determines the movement that is chosen for the *SNND* lattice in the current study, which consists of single beads. The bead cannot be moved if the conformation of the three beads, two attached neighbors and the center bead that needs to be moved, corresponds to an extended conformation. Otherwise, there are one or three possible sites for the beads to migrate. On the underlying completely atomistic diamond lattice, the movement of the single bead on the *SNND* lattice can shift the locations of two or three successive carbon atoms. Three distinct conformational changes can be attributed to each of these two potential movements.

3.2.1.3 Metropolis Monte Carlo Algorithm

The technique of Monte Carlo sampling has gained popularity for simulating polymeric systems. Conformations would be selected at random by a basic Monte Carlo sampling technique, and they would then be weighed using $e^{-\Delta E/KT}$. The following is the algorithm's flow:

$$P = \begin{cases} \Delta E \leq 0 \rightarrow \text{Accept Move} \\ \Delta E > 0 \rightarrow \exp(-\Delta E/KT) > \lambda \rightarrow \text{Accept Move} \end{cases} \quad (3.1)$$

The energy difference, ΔE , between the old and new conformations, encompasses both short- and long-range interactions. T is the absolute temperature, while K is the universal gas constant. The movement is available if $\Delta E \leq 0$. Otherwise,

a random number is created to indicate whether the location change was successful or not.

3.2.1.4 Short-Range Interactions

The RIS model developed by Rapold and Mattice is used to calculate the short-range interactions. The nature of bead polymer chains is described using RIS models. The following statistical weight matrix defines RIS model for PE (Abe, 1966).

$$\mathbf{U} = \begin{bmatrix} 1 & \sigma & \sigma \\ 1 & \sigma & \sigma\omega \\ 1 & \sigma\omega & \sigma \end{bmatrix} \quad (3.2)$$

where σ and ω are the first-order ($\sigma = \exp(-E_\sigma/RT)$) and second-order interactions ($\omega = \exp(-E_\omega/RT)$). E_σ is 2.1 kJ/mol and E_ω is 8.4 kJ/mol for PE.

The $(i-1)^{\text{th}}$ and i^{th} bonds conformation states are represented by the rows and columns of the matrix, respectively. The indexing sequences are t , g^+ and g^- . In Doruker (1996), the statistical weight matrix for coarse-grained PE bonds was thoroughly explained and summarized.

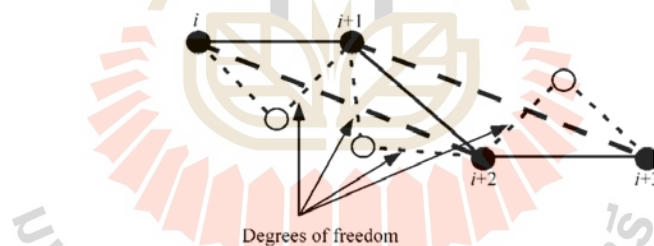


Figure 3.5 Polyethylene chain represented on the SNND lattice and its detailed conformation corresponding to the diamond lattice.

3.2.1.5 Long-Range Interaction

Long-range interactions originate from a discretized form of the Lennard-Jones (LJ) potential, wherein the second virial coefficient (B_2) for polymers is estimated comparable to a nonideal gas using the Mayer f function by the imperfect gas theory (Cho, 1997):

$$B_2 = \frac{1}{2} \int \{ \exp [-\beta u(r)] - 1 \} dr = \frac{1}{2} \int f dr \quad (3.3)$$

where $\beta=1/kT$, f is the Mayer function and $u(r)$ is the inter-particle LJ potential of the form

To ensure the volume exclusion in this simulation, the LJ potential energy function with hardcore is employed.

$$u = \begin{cases} \infty & r < 2.5\text{\AA} \\ u_{\text{LJ}} = 4\epsilon \left[\left(\frac{\sigma}{r}\right)^{12} - \left(\frac{\sigma}{r}\right)^6 \right] & r \geq 2.5\text{\AA} \end{cases} \quad (3.4)$$

where the collision diameter and the well depth are denoted by σ and ϵ , respectively

On the 2nd lattice, the prohibition of double occupancy of any site implies $u=\infty$, $r < 2.5\text{\AA}$, and u at the remaining sites can be represented by a truncated Lennard-Jones potential energy function. r is the distance between two interacting beads. On the lattice, B_2 is expressed in a discretized form by splitting the integral into the sub-integral for each lattice cell and regrouping the integrals for each neighbor.

3.2.2 Nanocomposite Models with different nanofiller shapes

The *polymer forcefield* to describe intra- and intermolecular interaction is composed of the rotational isomeric state (RIS) model of PE and the Lennard-Jones (LJ) potential energetics of ethylene units, respectively. For intramolecular interaction, the repulsive first-order interactions are variants of the one that occurs in the *gauche* conformations of *n*-butane. The second-order interaction included is the one commonly described as the *pentane effect*, which is generated by the repulsive interaction of the terminal methyl groups in the conformations of *n*-pentane with *gauche* placements of opposite signs. The energetics for the RIS model of PE chains were represented by the first- and second-order interaction energies of $E_\sigma = 2.1$ and $E_\omega = 8.4$ kJ/mol, respectively (Flory, 1969; Mattice, 1994). The CG chains were done by grouping every CH_2CH_2 monomer as one bead and then these CG chains were mapped to the 2nd lattice sites (Baschnagel, 2000). For intermolecular interaction, non-bonded and long-range intramolecular interactions are incorporated via a pair-wise interaction potential *i.e.* Lennard-Jones (LJ) function. All pairs of beads from different chains are included in the intermolecular interaction. The intramolecular interaction

of next-nearest beads has already been counted in the RIS model and ignored in the construction of the non-bonded interaction, to avoid double counting. The intermolecular interaction between CG beads was represented by the discretized LJ energy of ethylene monomer ($\epsilon/k_B = 185$ K, $\sigma = 0.44$ nm), with the energy parameters at each temperature presented in Table 3.1 To speed up the simulation, only the first three shells were used for CG beads separated by 0.25, 0.50 and 0.75 nm, respectively. Hence, the cut-off distance is 0.75 nm and the calculation of non-bonded energies beyond the third shell (> 0.75 nm) was simply neglected (Baschnagel, 2000).

In addition to spherical nanofillers, two nanofillers with different geometry were studied for their effect on the structural formation of PE nanocomposite. The polymer matrix was filled by these nanofillers by having an impenetrable volume with the corresponding shape. Three kinds of nanofillers were created to have almost the same number of beads as denoted by nanostick (S1), nanoplate (S2) and nanosphere (S3). Each CG bead in nanofillers is equivalent to ethylene unit as used in the description of PE model.

Figure 3.6 illustrates the characteristics of these nanofillers and Table 3.2 presents a detailed description for all simulated systems. During simulation, polymer chains can be moved with every single bead hopping to the vacant site with the constraint of chain connectivity. The bead moves were accepted or not follow the Metropolis criteria (Baschnagel, 2000). The nanofillers were at a fixed position and inaccessible to PE chains. This model was acceptable as the mass of the nanofiller was much higher than that of the polymer. All PNC models consisted of one nanofiller and 60 C_{40} chains (20 CG beads) placed in the $2nd$ lattice with the dimension of $18 \times 18 \times 18$ lattice units (each lattice unit = 0.25 nm). A reference bulk system without a nanofiller (65 chains of C_{40}) was also simulated for comparison.

PE chains in the periodic box were generated initially based on the self-avoiding walk chains in which no walk was allowed to penetrate the nanofiller volume. Then the RIS model and LJ energies were incorporated into PNC models and the structures were then equilibrated at 473 K. The bead fraction in the $2nd$ lattice was 0.2246 or the density of 0.95 g/cm³ (close to the density of crystalline PE). MC simulations were

run for 10^6 Monte Carlo steps (MCS) at 473 K, 400 K and 350 K. Finally, simulations were continued at 298 K for a total run of 10^8 million MCS. By definition, one MCS is equal to an average attempt to move each monomer bead in the system. Data were analyzed in the total trajectory of 10^8 million MCS recorded every 10^4 MCS. Simulations were repeated 3 times starting from different initial structures and similar results were obtained so that only one representative trajectory in each system is presented in the results and discussion part.

Table 3.1 Parameters for polymer-polymer and polymer-nanofiller interaction.

Temperature (K)	First shell (kJ/mol)	Second shell (kJ/mol)	Third shell (kJ/mol)
473	15.048	0.620	- 0.625
400	12.835	0.388	- 0.630
350	11.281	0.220	- 0.635
298	9.625	0.038	- 0.642

Table 3.2 Description of the simulated systems.

System Identifier	Nanofiller Geometry	Dimension in x, y and z direction (lattice units)	Number of total beads	Number of surface beads
S0	-	-	0	0
S1	nanostick	3 x 3 x 9	81	74
S2	nanoplate	6 x 7 x 2	84	84
S3	nanosphere	5 (diameter)	84	54

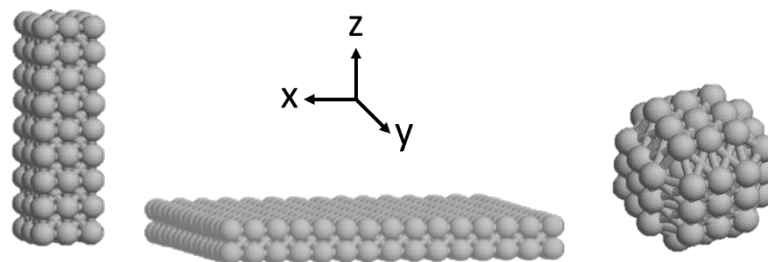


Figure 3.6 The geometry of nanofillers used in this simulation (left) S1-nanostick (middle) S2-nanoplate and (right) S3-nanosphere.

3.3 Coarse-grained polymer nanofilm models between impenetrable walls: Effect of surface affinity

3.3.1 Nanofilm models

Simulations were carried out using the Metropolis Monte Carlo technique on a high coordination lattice known as the second closest neighbor diamond (*2nd* or *SNND*) lattice (Rapold, 1996). The lattice constant of the high coordination lattice is 0.25 nm, and there are 60° angles between any unit vectors along the axes. In this work, the periodic box dimension is $28 \times 28 \times 33$ lattice units. The systems are composed of 200 PE models with 20 repeating units and the impenetrable wall has the thickness of 5 lattice units placed at $0 \leq Z \leq 4$. The impenetrable walls were fixed during the simulations. The energetics include the long-range interchain interaction relying on the 6-12 Lennard-Jones (LJ) potential and the short-range intrachain interaction depending on the rotational isomeric state (RIS) model. The classic RIS model for PE, as defined by Abe (1966) utilized intramolecular short-range interactions with the first- and second-order interaction as $\sigma = 2.1$ and $\omega = 8.4$ kJ/mol, respectively. The long-range interaction in the polymer was treated with a discretized Lennard-Jones (LJ) potential energy that describes the pairwise interactions of ethylene ($\epsilon/k_B = 185$ K, $\sigma = 4.4$ Å). The wall's surface affinity is controlled by the factor (w), as shown in Eq. 3.5 The repulsive, neutral, and attractive interactions were represented by w values of 0.1, 1.0, and 2.0, respectively. The distance between the bead centers

is denoted by r in this equation, σ is the location at this minimal energy, and ϵ is the depth of LJ potential energy.

$$u = \begin{cases} \infty & r < 2.5\text{\AA} \\ u_{\text{LJ}} = 4\epsilon \left[\left(\frac{\sigma}{r}\right)^{12} - \left(\frac{\sigma}{r}\right)^6 \right] & r \geq 2.5\text{\AA} \end{cases} \quad (3.5)$$

In this study, the effect of polymer-wall interaction on the structures and properties of the confined PE nanofilms are investigated by comparing 4 systems with different kinds of solid substrates denoted by 20x, 20n, 20a and 20r, respectively, where the alphabet letters represent the wall interaction in each system (x:no interaction, n:neutral, a:attractive, r:repulsive) and 20 is the number of beads in PE. Data analysis was performed from the taken snapshots every 10,000 MCS from subsequent 40 million MCS trajectories after equilibration.

3.4 Multiscale simulation of Poly(propylene oxide)

3.4.1 Rotational Isomeric State (RIS) model

The RIS model is a useful tool for quickly and simply calculating a single polymer molecule's conformationally dependent characteristics and accounting for the chain's detailed chemical structure. Rotational isomers are local minima produced by internal rotation about main-chain bonds. These are considered to be discrete states, so the degree of freedom in this problem will be significantly reduced. Focus on relative energies of the states that determine the probability at a particular conformation, Under an additional assumption of fixed bond lengths and bond angles, a set of rotation states along a chain's bonds completely represents the chain geometry. The RIS model enables quick and precise computations by producing attributes of a single chain and an accurate representation of chain conformational statistics for a molecule.

The most commonly utilized theoretical quantities in RIS Theory, such as the proportion of bond conformer for a polymer chain, are conformational dependent properties that may be compared with an experimentally quantifiable quantity. These

properties are highly dependent on the quality of statistical weights used in the computation. Statistical weight is found by deriving from sections of the conformational energy map. The contour map indicates a variation in a molecule's energetics for every two consecutive pairs of torsion angles.

The RIS program computes a flexible polymer chain's characteristic using Flory's RIS theory. In situations when long-range excluded volume effects may be disregarded, this theory takes into consideration the effects of the torsional states of the bonds in the chain on their adjacent. The RIS model attempts to determine the conformational partition function using the energy resulting from the polymer chain's torsion angle under theta or undisturbed conditions.

Then, the partition function can be written as the product of these weights sum across all rotational states. This may be represented as a matrix as

$$Z = \prod_i U_i \quad (3.6)$$

Where U_i is the statistical weight matrix

In this work, we try to simplify the RIS representation of PPO by including only the first- and second-order interaction. It is then possible to reduce the original 9x9 statistical weight matrices proposed by Sasanuma (1995) to 3x3 dimension in order to comply with our scheme. The condensed form of 3x3 matrices can be illustrated as following:

$$U_{\bullet} = \begin{array}{c} \begin{array}{cccccc} & t & g+ & g- & t & g+ & g- & t & g+ & g- \\ \begin{array}{l} t & t \\ t & g+ \\ t & g- \\ g+t \\ g+g+ \\ g+g- \\ g-t \\ g-g+ \\ g-g- \end{array} & \begin{array}{|cccccc|} \hline 1 & \sigma & 0 & 0 & 0 & 0 & 0 & 0 & 0 \\ \hline 0 & 0 & 0 & 1 & 0 & 0 & 0 & 0 & 0 \\ \hline 0 & 0 & 0 & 0 & 0 & 0 & 1 & 0 & \sigma \\ \hline 1 & \sigma & 0 & 0 & 0 & 0 & 0 & 0 & 0 \\ \hline 0 & 0 & 0 & 1 & 0 & 0 & 0 & 0 & 0 \\ \hline 0 & 0 & 0 & 0 & 0 & 0 & 1 & 0 & \sigma \\ \hline 1 & \sigma & 0 & 0 & 0 & 0 & 0 & 0 & 0 \\ \hline 0 & 0 & 0 & 1 & 0 & 0 & 0 & 0 & 0 \\ \hline 0 & 0 & 0 & 0 & 0 & 0 & 1 & 0 & \sigma \\ \hline \end{array} \end{array} \end{array}$$

Figure 3.7 The reduction of 9 x 9 matrices.

From this reduction scheme, the 3x3 statistical weight matrices (neglecting the third order interaction) can be obtained for bond co-oc, oc-cc and cc-co as:

$$U_{\text{co-oc}} = \begin{pmatrix} 1 & \sigma & 0 \\ 1 & 0 & 0 \\ 1 & 0 & \sigma \end{pmatrix}$$

$$U_{\text{oc-cc}} = \begin{pmatrix} 1 & \alpha & \beta \\ 0 & \alpha & \beta\omega_2 \\ 1 & \alpha\omega_1 & 0 \end{pmatrix}$$

$$U_{\text{cc-co}} = \begin{pmatrix} 1 & \gamma & \delta \\ 1 & \gamma & \delta\omega_1 \\ 1 & \gamma\omega_2 & \delta \end{pmatrix}$$

Table 3.3 Energy parameters and geometry for two RIS models of PPO.

Parameters	α	β	σ	γ	δ	ω_1	ω_2
E(kJ/mol)	3.2	5.99	6.28	12.82	1.5	-5.15	-7.82

3.4.2 Long-Range Interaction

From eq 3.4, the σ and $\epsilon/k_B T$ are estimated from ethane (CH_3CH_3) and methyl ether (CH_3OCH_3) (Mark, 1965). For ethane, the $\sigma = 4.443 \text{ \AA}$ and $\epsilon/k_B T = 215.7 \text{ K}$. For methyl ether, the $\sigma = 4.307 \text{ \AA}$ and $\epsilon/k_B T = 395.7 \text{ K}$, respectively. The σ and $\epsilon/k_B T$ for PPO can be estimated from ethane (CH_3CH_3) and methyl ether (CH_3OCH_3) as follows

$$\sigma_{\text{PPO}} = (\sigma_{\text{ethane}} + \sigma_{\text{methyl ether}})/2 = 4.375 \text{ \AA} \quad (3.7)$$

$$\epsilon_{\text{PPO}} = (\epsilon_{\text{ethane}} \times \epsilon_{\text{methyl ether}})^{1/2} = 292.15 \text{ K} \quad (3.8)$$

The energy of long-range interactions are obtained by the discretization of this LJ potential. For instance, at 373 K, the first three shell parameters of PPO are 11.745, -0.353, and -1.011 kJ/mol. The interaction parameter for the second neighbor shell is negative, whereas the first neighbor shell is extremely repulsive. This interaction parameter covers the distance 2.4 - 4.8 \AA , which includes the collision diameter, 3.76 \AA . As a result, the second neighbor shell has the majority of the attractions. In this work, only the first three shells are applied.

3.4.3 Monte Carlo simulation of coarse-grained PPO model

Monte Carlo technique was performed on coarse-grained PPO chains that were mapped onto the second nearest diamond (*2nd*) lattice. The 3x3 RIS model (Sasanuma, 1995) and LJ potential were used to describe short- and long-range interaction. Each occupied site has a $-\text{CH}_2\text{-CH}(\text{CH}_3)$ or $-\text{CH}_2\text{-O}$ unit, linked by coarse-grained bonds of 2.39 Å in length. Each bead received the same treatment. The PPO melt density was simulated at 373 K, which is near the temperature utilized in the neutron scattering experiment and molecular dynamic modeling (Bolodin, 2003; Chen, 2006). The torsional angles are restricted to *trans* and two *gauche* states. Throughout the simulation, the completely atomistic model system is recoverable at any point of the simulation.

3.4.4 Reverse-mapping procedure of PPO to fully atomistic model

After generated the diamond lattice from reverse mapped, the coordinates of the carbon, oxygen, and hydrogen atoms within the polymer chains were obtained. The energy of the selected snapshot was minimized using a PCFF force field in Xenoview, a free molecular dynamics and mechanics simulation software, until the gradient was less than 0.1 kcal/(mol Å). The steepest descents method is used if the gradient is greater than 1000 kcal/(mol Å), and the conjugate gradient is used otherwise. To acquire the structures with the appropriate periodic box in this case, a brief *NPT* molecular dynamics performed 500 ps at a temperature of 373 K. Next, 1000 ps of *NVT* simulations are performed at 373 K. The example snapshot for the coarse-grained PPO chains is shown in Figure 3.8 before the reverse-mapping process that creates the fully atomistic model.

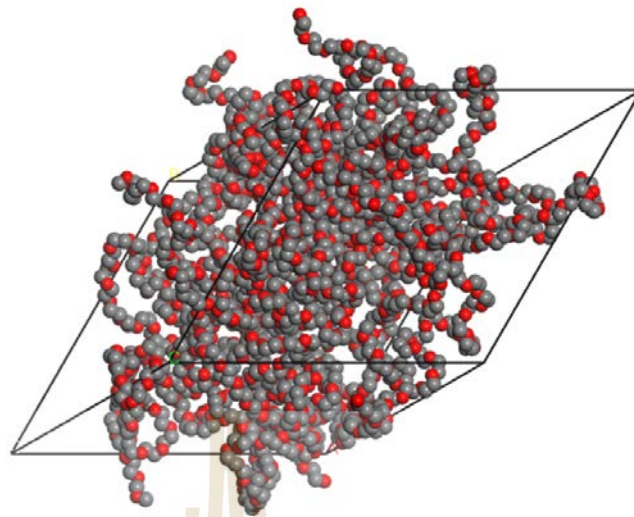


Figure 3.8 A particular snapshot from the coarse-grained PPO Monte Carlo simulation on the *2nd* lattice.

Then added alkaline salt including LiSCN and KSCN to see the dynamic of cations in polymer electrolyte. Here, *NVT* simulations are carried out at 373 K for 1000 ps.

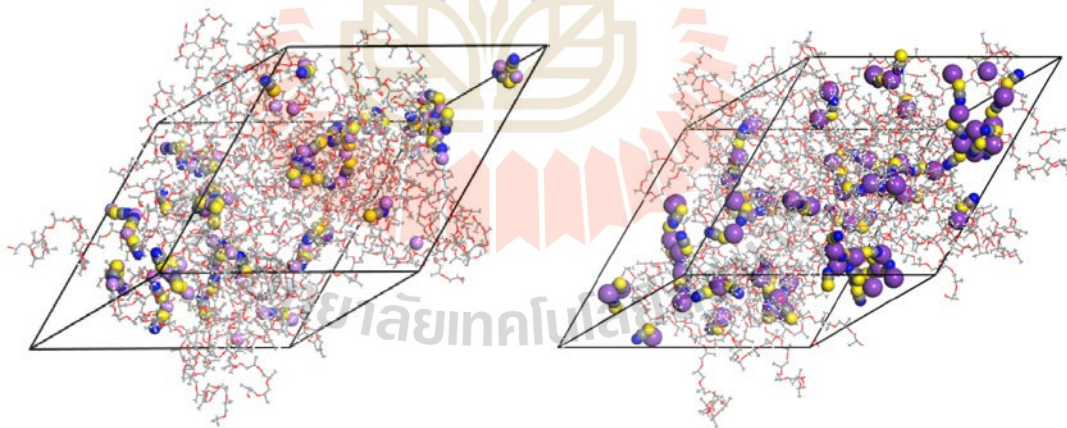


Figure 3.9 Specific snapshot from the Monte Carlo simulation of fully atomistic PPO on the *2nd* lattice with the addition of (a) LiSCN and (b) KSCN.

3.4.5 System Description

A periodic box with 20 unit lengths on each side of the lattice was used for the simulations; i.e., $L_x = L_y = L_z = 20$ which is equivalent to 47.8 Å. For all systems, a total of 1260 beads are put into this box to achieve the density of 0.98 g/cm³ which is close to the experimental density (1.06 g/cm³) for PPO at 373 K. The system is composed of 28 chains with $N = 45$ units. Each chain can be reverse-mapped to 90 backbone atoms which is equivalent to CH₃(OCH(CH₃)CH₂)₂₉OCH₃. The initial configuration was randomly distributed in the periodic box. To ensure the equilibrium, about 90 million MCS were performed at 373 K and data were recorded every 10,000 MCS for subsequent analysis. After that added LiSCN and KSCN in to the polymer matrix with the ratio of M:O=1:16. Following energy reduction, MD simulations were carried out for 1ns at 373 K using NVT ensemble.

Table 3.4 The simulation's charge parameters.

Atoms	q (e)
K	+1.000
S _{SCN}	-0.746
C _{SCN}	+483
N _{SCN}	-0.737

CHAPTER IV

RESULTS AND DISCUSSION

4.1 The Effect of Adding Si-based Nanofillers on Polyethylene Oxide

This section will mainly focus on the addition of silica-based nanoparticles which have a spherical shape like silica (SiO_2). The silica was modified surface (A- SiO_2 , SiL- SiO_2) in order to study more on the surface effect. Moreover, MMT and POSS were used to compare to see some relation for shape effect.

4.1.1 Polarized Optical Microscopy (POM)

Effect of Silica nanofiller content on isothermal crystallization of PEO

Optical microscopy was used to investigate the crystallization of SiO_2 /PEO nanocomposites between 48 and 52°C, a temperature range where spherulites of appropriate dimension form. Spherulites of PEO with varying concentrations of untreated SiO_2 nanoparticle (NPs) develop isothermally at 52°C, as shown in Figure 4.1.1.

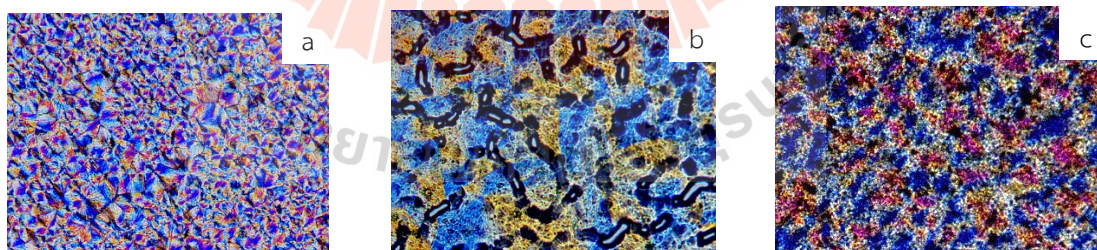


Figure 4.1.1 PEO/ SiO_2 nanocomposite film optical micrographs using crossed polarizers during isothermal crystallization at 52°C (a) neat PEO; (b) 10 wt% SiO_2 /PEO; (c) 20 wt% SiO_2 /PEO.

Lauritzen-Hoffman kinetics were used to investigate the SiO₂/PEO nanocomposites spherulite growth rate, G. The radius of the spherulites is plotted against crystallization time to calculate their growth rates. These graphs for SiO₂ NP content from 0 to 20 wt% are displayed in Figure 4.1.2. Each line denotes a distinct crystallization temperature.

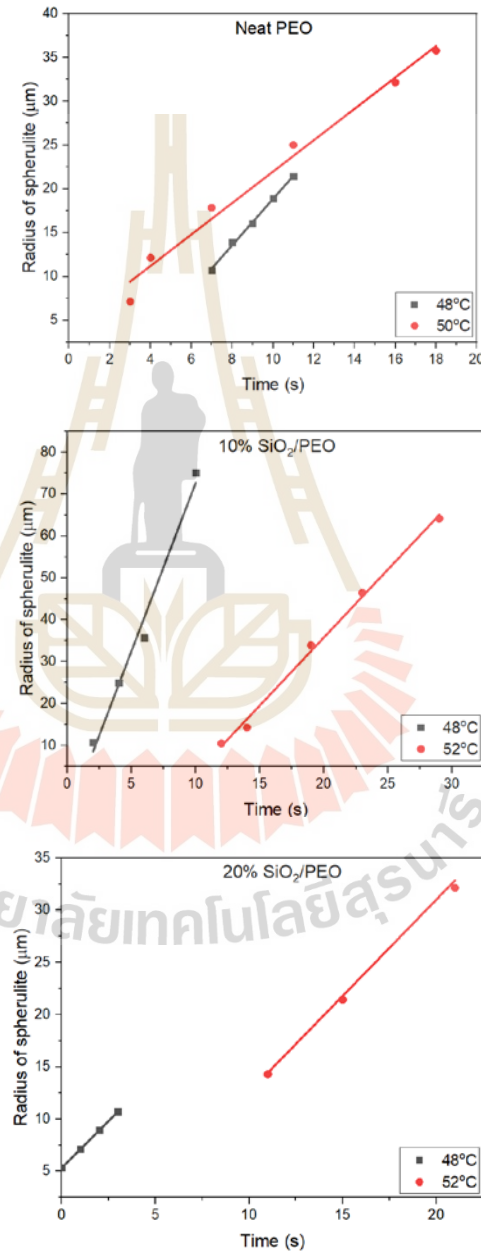


Figure 4.1.2 Spherulite radius plots for SiO₂/PEO nanocomposites versus time with different crystallization temperature (a) neat PEO; (b) 10 wt% SiO₂/PEO; (c) 20 wt% SiO₂/PEO.

The spherulite development rate is indicated by the slope. Figure 4.1.3 illustrates how the rate of spherulitic development rises when the crystallization temperature drops from 52 to 48°C. This is because the driving force increases and the polymer's mobility in the melt reduces.

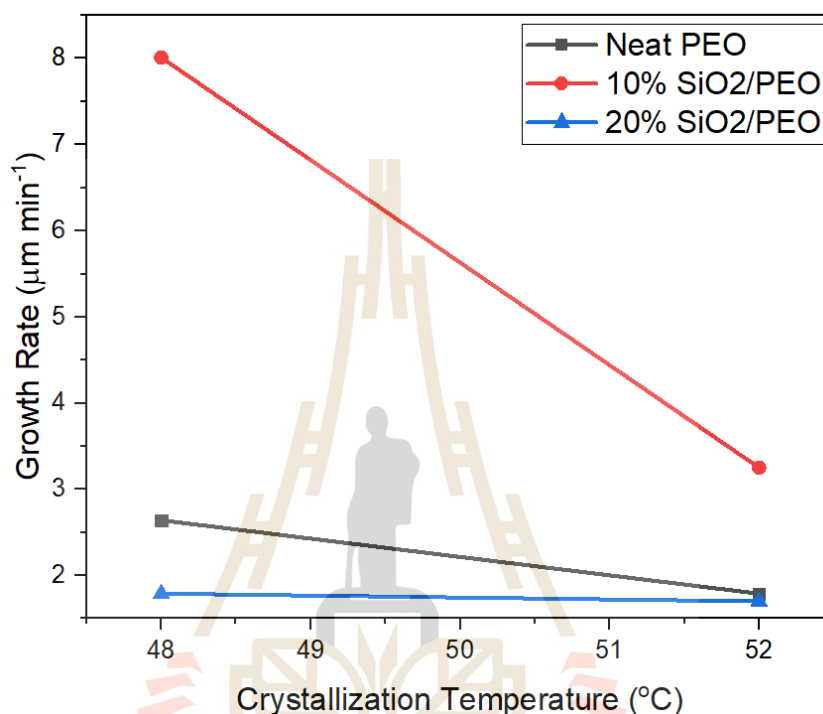


Figure 4.1.3 Plots of logarithm of spherulite growth rate *versus* crystallization temperature for SiO₂/PEO nanocomposites as a function of SiO₂ content.

As the SiO₂ concentration increases, the observed spherulite growth rate (G_0) decreases, suggesting that the SiO₂ NPs are interfering with the spherulites ability to grow (Figure 4.1.3). The spatial constraints on crystallizing units caused by limiting them to the confined space between SiO₂ NPs can account for the decrease in the linear growth rate.

Effect of silica-base nanofiller on isothermal crystallization of PEO

The crystallization of a polymer matrix may be significantly impacted by the surface functionality of nanofillers. Silica modified with amino (A-SiO₂) and silane (Sil-SiO₂) were used and also compare to another silica-base nanofiller including POSS and MMT.

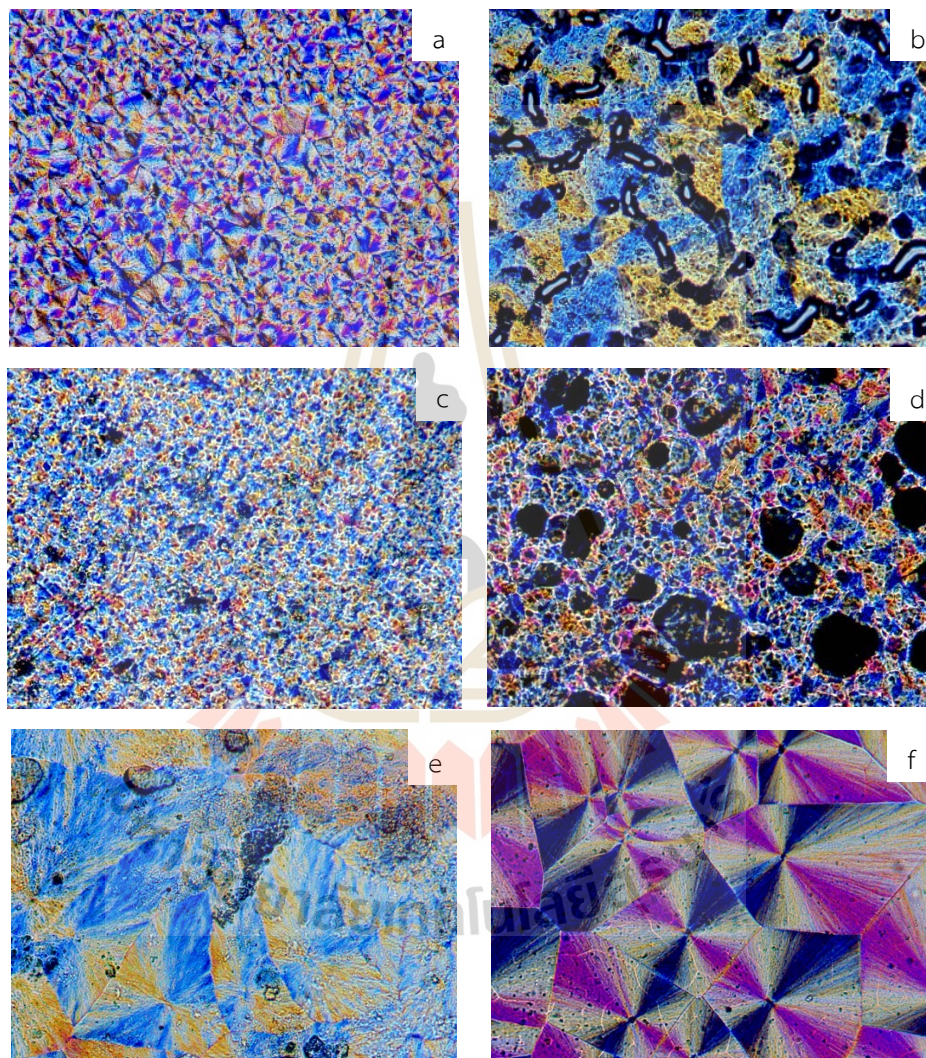


Figure 4.1.4 Optical micrographs of 10 wt% PEO/Si-based nanocomposite films after isothermal crystallization at 52 °C with crossed polarizers: a) pure PEO, b) SiO₂/PEO, c) Sil-SiO₂/PEO, d) A-SiO₂/PEO, e) MMT/PEO and f) POSS/PEO.

POM was used to analyze the silica-base filler/PEO nanocomposites (Figure 4.1.4). Higher nucleation density is shown by the fact that Sil-SiO₂ and A-SiO₂ offer more spherulites in the area of view among the NPs. Furthermore, compared to the utilization of non-functionalized SiO₂, the spherulite diameters of the Sil-SiO₂ and A-SiO₂ nanocomposites are lower. Regretfully, in comparison to other NPs, SiO₂ NPs and A-SiO₂ NPs provide comparatively non-uniform spherulite size and spacing between spherulites. This can be attributed to co-aggregation of SiO₂ NPs and A-SiO₂ NPs due to hydrogen bonding between OH-OH in SiO₂ NPs and NH₂-NH₂ in A-SiO₂ NPs. This is the reason why studies generally use Sil-SiO₂, because Sil-SiO₂ NPs have non-reactive end group that allows good dispersion with no aggregation occurring. For both MMT/PEO POSS/PEO show large spherulite.

The radius of the spherulites was displayed as a function of annealing time in order to examine the rate of spherulite development. The dependence of spherulite development on the nanofiller is seen in Figure 4.1.5.

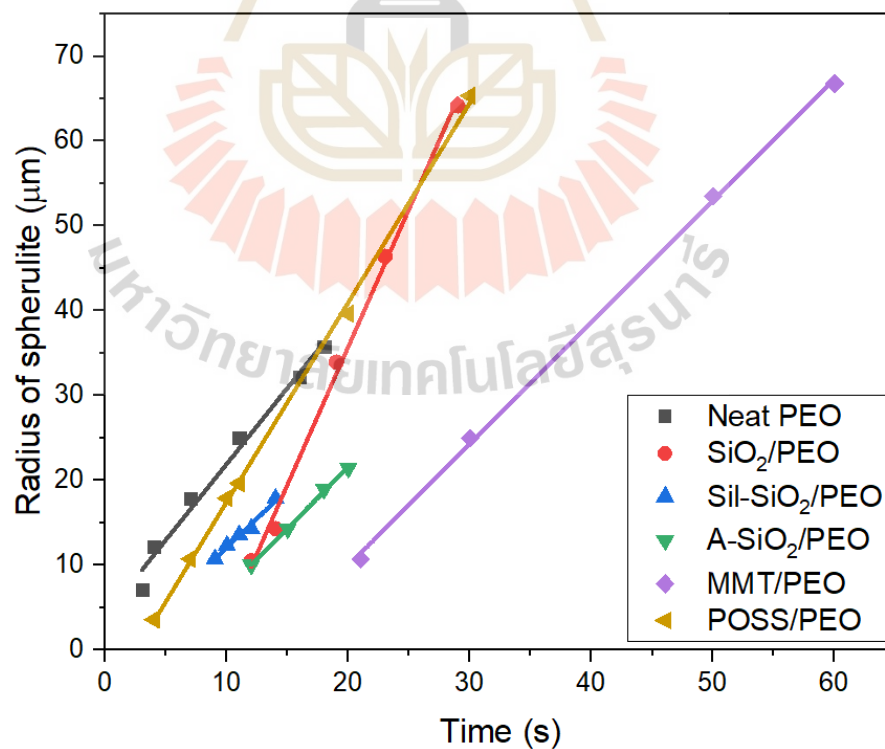


Figure 4.1.5 Plots of spherulite radius versus time for PEO nanocomposites at 52°C.

Table 4.1.1 Growth rate of polymer nanocomposite with 10% filler at 52°C.

Sample	Growth rate ($\mu\text{m/s}$)
Neat PEO	1.79
SiO ₂ /PEO	3.25
Sil-SiO ₂ /PEO	1.38
A-SiO ₂ /PEO	1.45
MMT/PEO	1.43
POSS/PEO	2.35

The spherulite growth rate follows the order SiO₂ > POSS > PEO (without NPs) > A-SiO₂ > MMT > Sil-SiO₂. If not focusing on the SiO₂ NPs and A-SiO₂ NPs due to their aggregation, MMT and Sil-SiO₂ induce a slower growth rate of spherulite than neat PEO without NPs.

4.1.2 Differential Scanning Calorimeter (DSC)

Non-isothermal crystallization kinetics

When it comes to polymer crystallization, investigations into the process are often restricted to isothermal settings, theoretical analysis is straightforward, and issues with cooling rates and temperature gradients inside the specimens are unconcerned.

But in reality, as industrial processes typically take place in non-isothermal environments, the crystallization in a constantly changing thermal environment is of more relevance. The melting crystallization DSC curves and the relative degree crystallinity values at various cooling speeds as a function of temperature are shown in Figure 4.1.6.

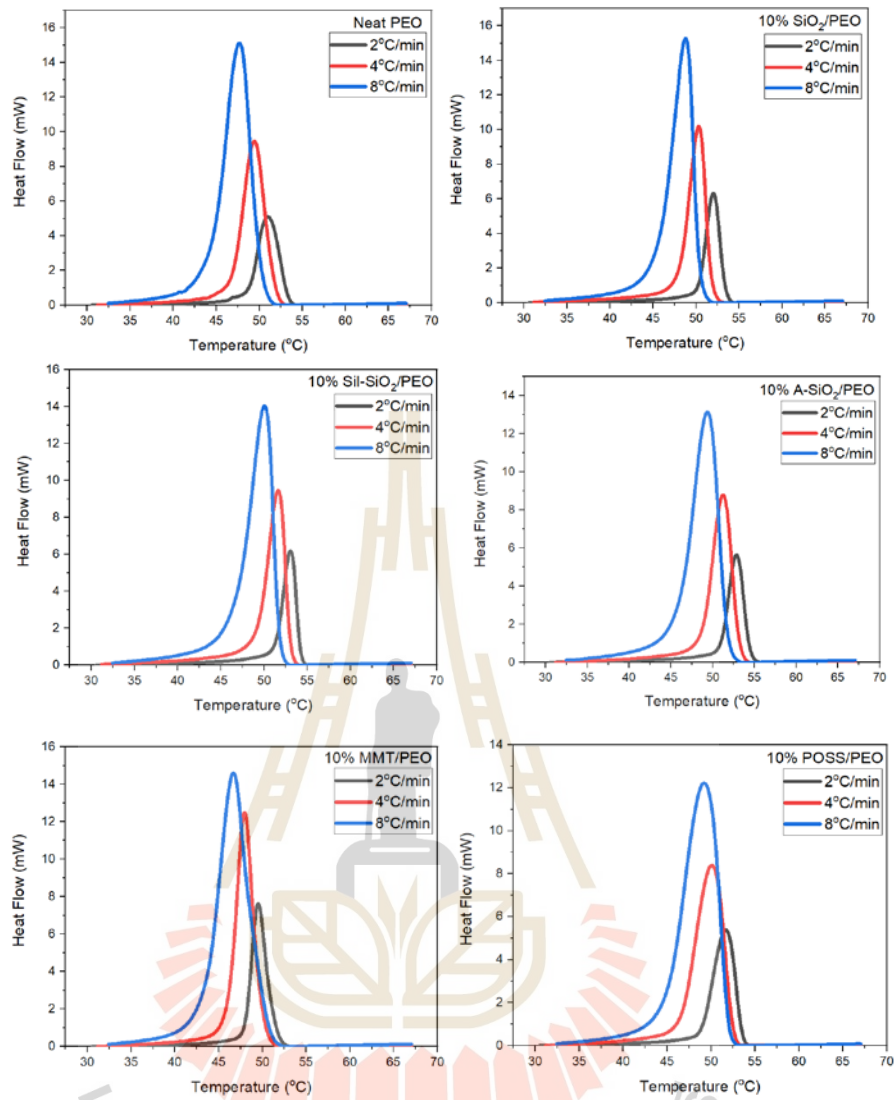


Figure 4.1.6 DSC thermograms of a) PEO, b) 10% SiO₂/PEO, c) 10% SiI-SiO₂/PEO, d) 10% A-SiO₂/PEO, e) 10% MMT/PEO and f) POSS/PEO at various cooling rates: 2 °C/min, 4 °C /min and 8 °C /min.

During the non-isothermal crystallization process, Eq. 4.1.1 provides the connection between the crystallization temperature T and time t .

$$t = \frac{|T_0 - T|}{a} \quad (4.1.1)$$

Where a is the cooling rate, T is the crystallization temperature, T_0 is the temperature at which crystallization starts ($t=0$), and t is the crystallization duration.

Eq. 4.1.1 states that the crystallization time t may be obtained from the value of T on the X-axis. The results for the sample crystallinity change over time are shown in Figure 4.1.7. All curves are sigmoidal. It appears that the cooling rate affects the changes in the percent of crystallinity. The time required for crystallization to complete decreases with increasing cooling rate.

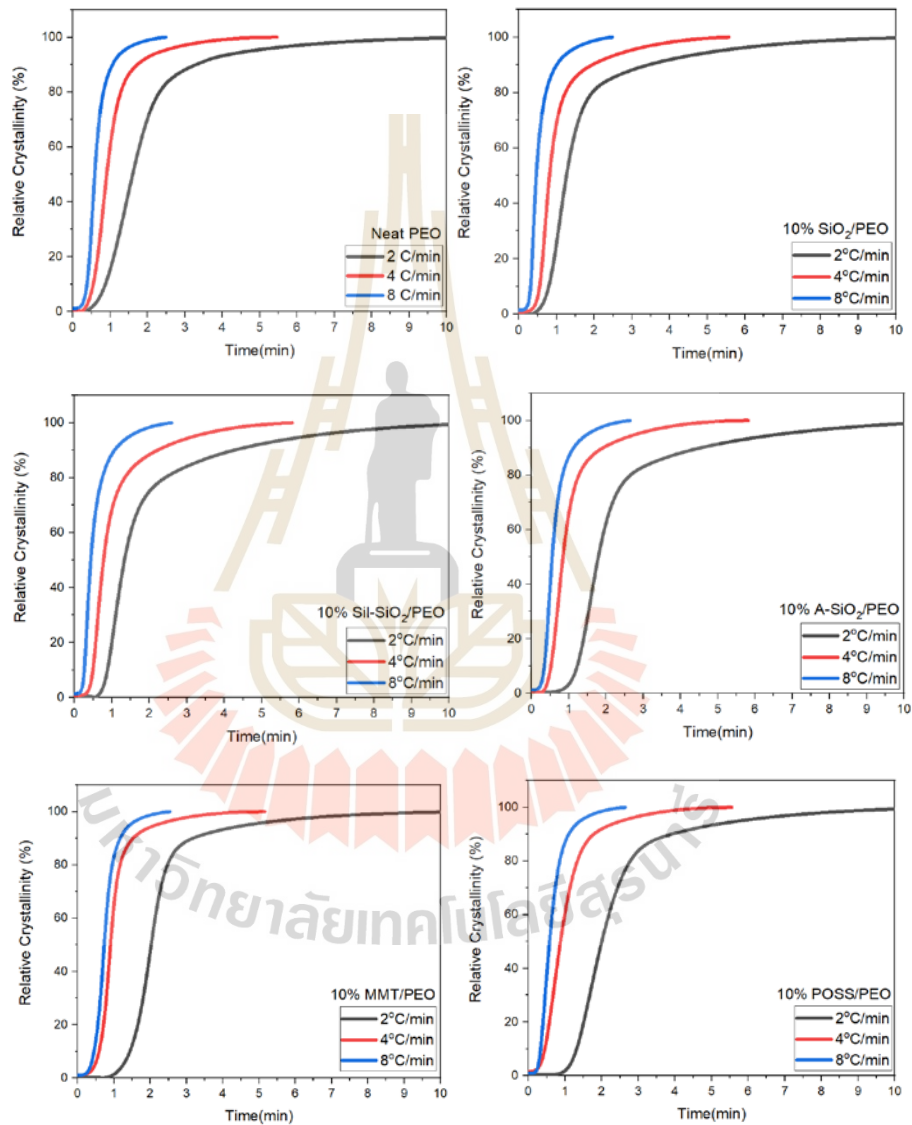


Figure 4.1.7 Plots of X_t versus time for crystallization of a) PEO, b) 10% SiO₂/PEO, c) 10% Sil-SiO₂/PEO, d) 10% A-SiO₂/PEO, e) 10% MMT/PEO and f) POSS/PEO at various cooling.

The half-time ($t_{1/2}$) of non-isothermal crystallization of PEO, 10% SiO₂/PEO, 10% SiI-SiO₂/PEO, 10% A-SiO₂/PEO, 10% MMT/PEO and 10% POSS/PEO could be obtained from Figure 4.1.8, and the results are listed in Table 4.1.2 which can be plot between $t_{1/2}$ and scan rate in Figure 4.1.8. As expected, the order of $t_{1/2}$ decreases with the increasing cooling rates.

Table 4.1.2 Half-time of polymer nanocomposite with 10% filler.

Sample	Scan Rate	$t_{1/2}$ (min)
Neat PEO	2	1.60
	4	0.91
	8	0.58
10% SiO ₂ /PEO	2	1.26
	4	0.81
	8	0.46
10% SiI-SiO ₂ /PEO	2	1.33
	4	0.77
	8	0.43
10% A-SiO ₂ /PEO	2	1.79
	4	0.84
	8	0.55
10% MMT/PEO	2	2.02
	4	0.90
	8	0.73
10% POSS/PEO	2	2.00
	4	0.87
	8	0.57

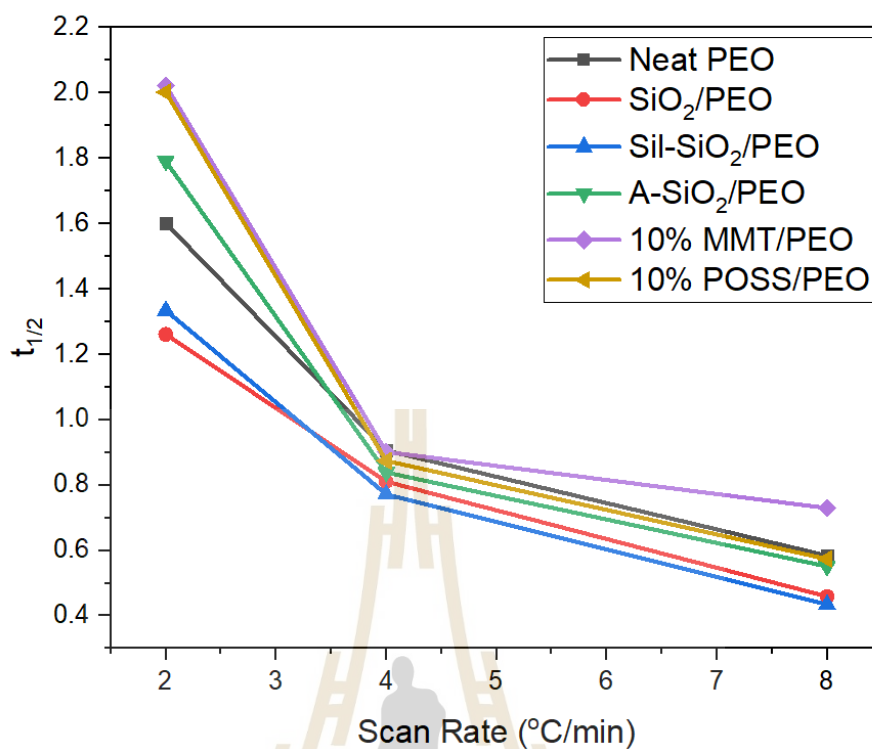


Figure 4.1.8 Plots of $t_{1/2}$ versus scan rate of a) PEO, b) 10% SiO₂/PEO, c) 10% Sil-SiO₂/PEO, d) 10% A-SiO₂/PEO, e) 10% MMT/PEO and f) POSS/PEO.

The $t_{1/2}$ follows the order MMT > POSS > PEO > A-SiO₂ > Sil-SiO₂ ≈ SiO₂. MMT, planar shape nanofiller, has the highest $t_{1/2}$ due to intercalation. On the other hand, A-SiO₂ NPs induce smaller half-time of crystallization compared to neat PEO. This may be because A-SiO₂ dispersion induce crystal nucleation throughout the sample resulting in lesser time use for the crystallization process.

4.1.3 Small Angle X-ray Scattering (SAXS)

Figure 4.1.9 displays the findings from all samples Lorentz-corrected small-angle X-ray scattering (SAXS).

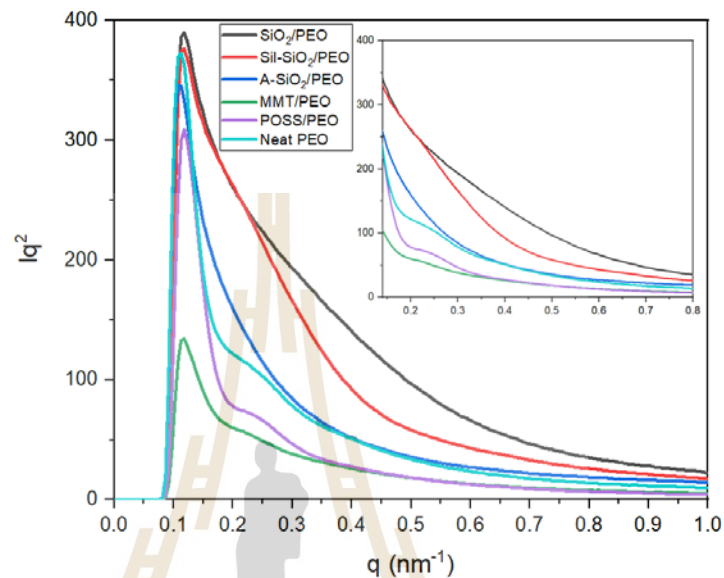


Figure 4.1.9 Semicrystalline PEO with silica-base nanofiller Lorentz-corrected SAXS as a function of the scattering vector, q .

The result shows that in the case of PEO, MMT/PEO and POSS/PEO, the primary scattering contrast is between the crystal and amorphous phase. However, the dominant contrast in PEO/SiO₂, PEO/Sil-SiO₂ and PEO/A-SiO₂ are between the silica and the polymer. Using the relationship

$$h_{\text{eff}} = \frac{2\pi}{q_m} - d_{\text{eff}} \quad (4.1.2)$$

where h_{eff} is the effective surface-to-surface separation between the particles and d_{eff} is the effective particle diameter (15 nm), h_{eff} was determined to be 38, 38, and 43 nm for SiO₂, Sil-SiO₂, and A-SiO₂ filler loadings, respectively. This shows a high degree of confinement for these filler loadings. To see more results, the dilution of NPs are important.

4.2 Coarse-grained polymer nanocomposite models: Effect of nanofiller shapes on polymer crystallization from the melts

4.2.1 Equilibration

Structural relaxation can be evaluated using the rotational and translation motions defined by the orientational auto-correlation function (OACF) and the mean-squared displacement (MSD), respectively. The OACF can be applied for the end-to-end vector, $\langle R(t) \cdot R(0) \rangle / \langle R^2 \rangle$ and the bond vector, $\langle m(t) \cdot m(0) \rangle / \langle m^2 \rangle$. For the translational motion, the MSD of the center of mass (g_{cm}) and individual bead (g_{bead}) can be defined as

$$\begin{aligned} g_{cm}(t) &= \langle [r_{cm}(t) - r_{cm}(0)]^2 \rangle \\ g_{bead}(t) &= \langle [r_i(t) - r_i(0)]^2 \rangle \end{aligned} \quad (4.2.1)$$

Here, $r_{cm}(t)$ and $r_{cm}(0)$ are the coordinates of the chain center of mass; $r_i(t)$ and $r_i(0)$ are the location of the CG bead i at time t and 0 , respectively. The angle brackets are used to represent the ensemble average of these quantities.

From Figure 4.2.1(a), OACFs of the end-to-end vectors at 298 K imply that chains in the PNC tend to relax faster than those in the bulk system (except PNC with nanoplate filler) and can be ordered as: S3-nanosphere > S1-nanostick > S0-bulk > S2-nanoplate. From Figure 4.2.1(b), bond relaxation is faster than the end-to-end vector as expected. OACFs of the bond vector also suggest that faster dynamics are seen in PCNs in a similar pattern. For translation motion, g_{cm} for all systems have magnitudes exceeding their chain dimensions within simulation time (100 million MCS) but the order is different as: S1-nanostick > S2-nanosphere \geq S2-nanoplate \gg S0-bulk. Compared to the bulk system, the translational mobility of polymer chains in PNC is increased because more free volume can be formed near the nanofiller surface according to the same non-bonded LJ parameters for polymer-nanofiller and polymer-polymer interaction. PE chains in S2-nanoplate move slower than those of other PNCs because

chains can crystallize better so that there is smaller free space for chains to diffuse.

From Figure 4.2.1(c), the scaling behavior is observed for the $g_{cm}(t)$ of chains in S0-bulk system which is proportional to $t^{0.46}$ and $t^{0.85}$, respectively, before and after diffusive regimes in the long-time limit. For chains in PNCs, the scaling components become higher to $t^{0.71}/t^{0.63}/t^{0.69}$ and $t^{0.78}/t^{0.74}/t^{0.87}$ for S3/S2/S1 systems, respectively, in these two regimes. All the scaling numbers at 298 K are below 1.0 implying that the diffusion of polymer chains exhibit the non-Fickian behavior at this temperature. However, $g_{cm}(t)$ of PE chains in the bulk melts at 473 K can likely show the Fickian diffusion ($t^{0.96}$). A similar observation is seen for PNCs at 473 K when all scaling exponents are close to 1.0 *i.e.* $t^{1.06}/t^{1.01}/t^{0.92}$ for S3/S2/S1 systems.

In Figure 4.2.1(d), the local dynamics of individual monomer beads in PE chains for bulk and nanocomposites are analyzed and compared at 298 K for the total trajectory of 100 million MCS. Simulation results also suggest that monomers in PE nanocomposites can move faster than those in the bulk and can be compared in the order as $S0 < S1 < S2 < S3$. In general, the dynamics of beads near both ends of PE chains are increased significantly. Compared to the bulk, the dynamics of monomers in the middle position and near the chain end for PNCs become less different, especially nanofillers with planar surfaces. In general, polymer chains in the nanocomposites, with the same nanofiller-polymer and polymer-polymer interaction, exhibit faster mobility than those in the bulk system at the scale of bead, bond and the whole chain. The profiles in Figure 4.2.1(d) are not perfectly symmetric from these 100 million MCS trajectories. In principle, longer simulation run at 298 K should be necessary to fully equilibrate the systems. However, it is very difficult in practice as the magnitudes of the MSDs of beads are very small at 298 K. As the main focus of this work is to monitor the structural formation during the initial stage upon cooling from the melts, all subsequent results are then analyzed from these 100 million MCS trajectories. Note that polymer mobility may exhibit different behavior for rotational motion as chains are stretched at 298 K.

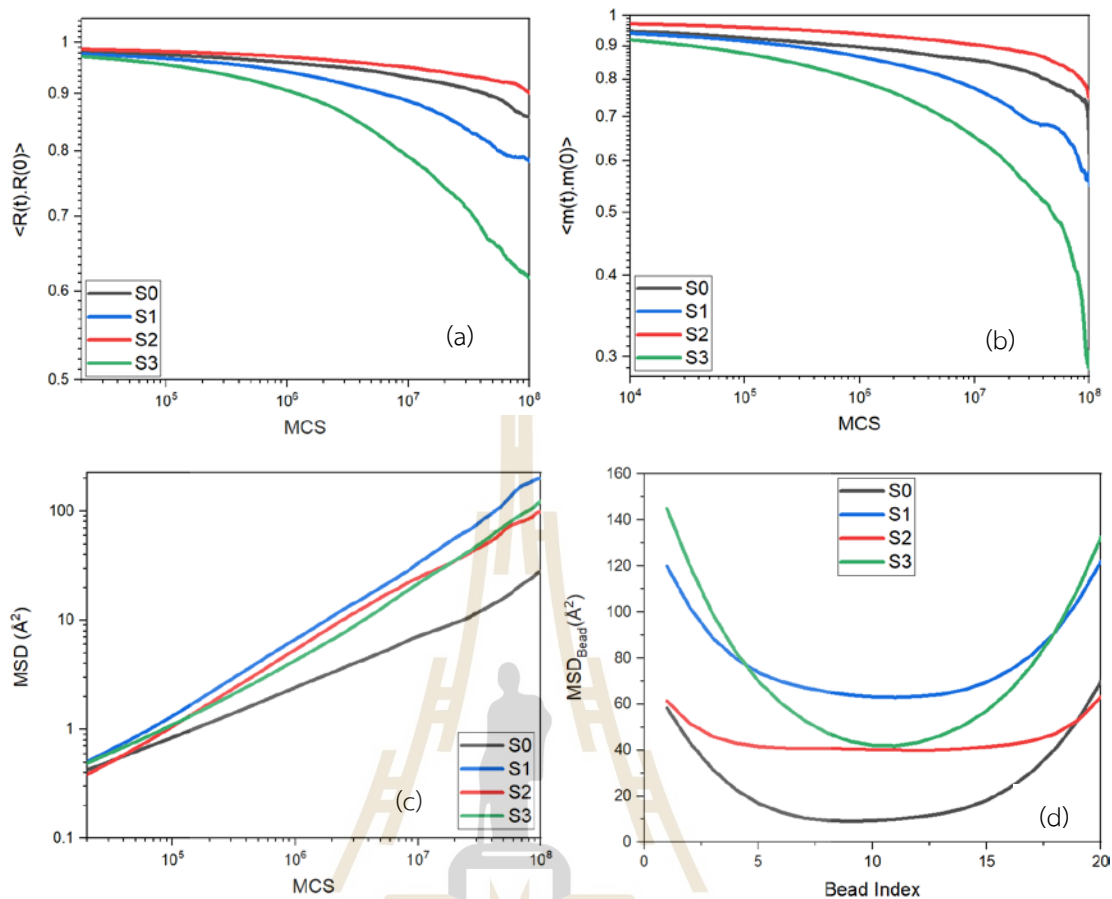


Figure 4.2.1 The orientational auto-correlation function of (a) polymer chains and (b) bonds, the mean-squared displacement of (c) polymer chains and (d) individual monomers at 298 K.

4.2.2 Energy

Figure 4.2.2(a) and 4.2.2(b) depict the change in the intra- and intermolecular energies of PNCs as a function of MCS. The energies for all systems are stable after around 50 million MCS. Intramolecular energetics are generally dropped at lower temperatures which are related to larger amount of *trans* state. The intrachain energies become higher for PE chains with larger amounts of *gauche* state and can be ordered as S2 (6972.38 ± 136.94 kJ/mol) < S1 (7286.00 ± 159.39 kJ/mol) < S0 (7645.00 ± 161.13 kJ/mol) < S3 (7899.90 ± 183.86 kJ/mol). For the intermolecular energies, the magnitudes are lower due to better chain packing in the order as: S0 (-4990.43 ± 57.50 kJ/mol) < S2 (-4622.83 ± 68.58 kJ/mol) < S1 (-4439.52 ± 73.30 kJ/mol) < S3 (-4290.47

± 76.15 kJ/mol). Intermolecular energies are normally related to the number of CG beads in the first, second and third shells that non-bonded interactions are included in this simulation. Their negative values suggest a larger number of CG bead pairs preferably located in the third shell. Hence, nanofillers with the planar surface can interact more effectively and can induce PE chains to be packed better to have smaller amplitude.

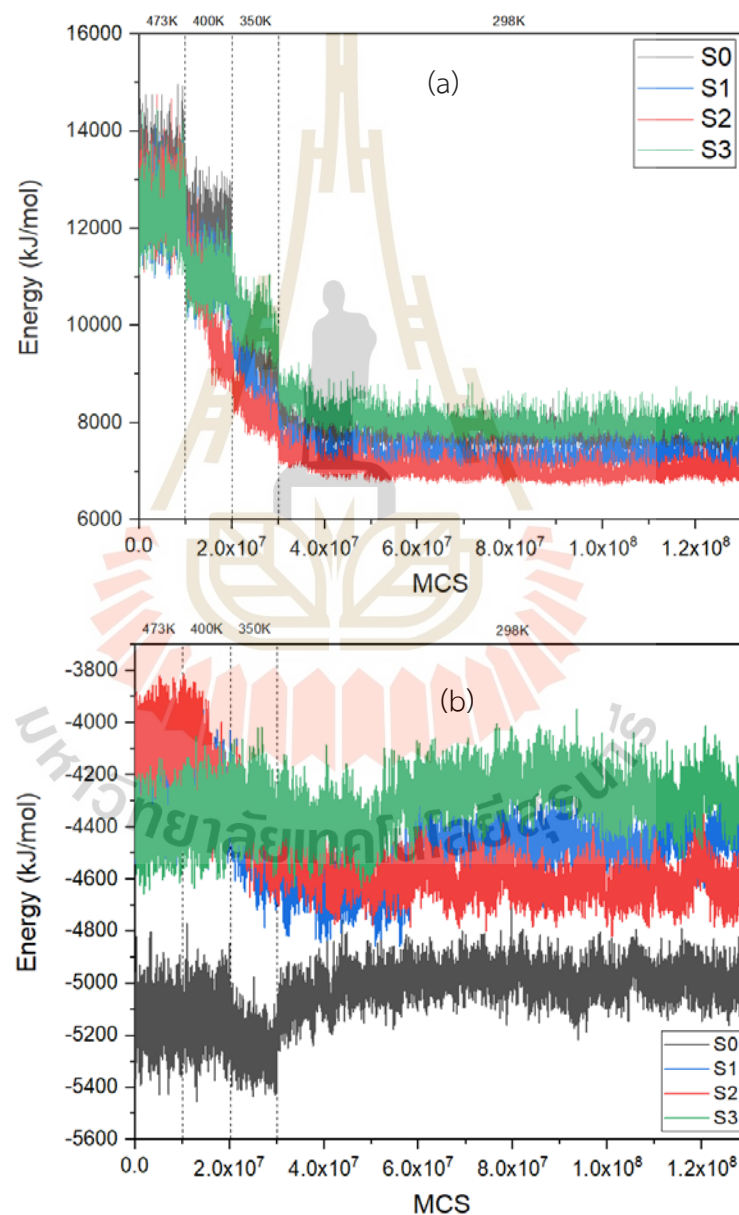


Figure 4.2.2 (a) Intramolecular and (b) intermolecular energy of PE chains in bulk and PNC at 473 K, 400 K, 350 K and 298 K.

4.2.3 Conformation

Figure 4.2.3 displays the final structures of PE chains in bulk and PNCs filled with nanofillers of different shapes at the end of 100 million MCS trajectories. The lattice parameters and packing of PE chains has a structure that is enforced by the geometry of the $2nd$ lattice on which simulation is performed. For all systems, the ordered structures with only one crystalline domain are observed in which PE chains have larger amount of *trans* state and are arranged in the same direction. Nevertheless, PE chains may adopt different orientations, specifically chains near the nanofiller surfaces. Compared among PE nanocomposites, the systems with nanoplate cause PE chains with the longest consecutive *trans* sequence and exhibit the most ordered structures.

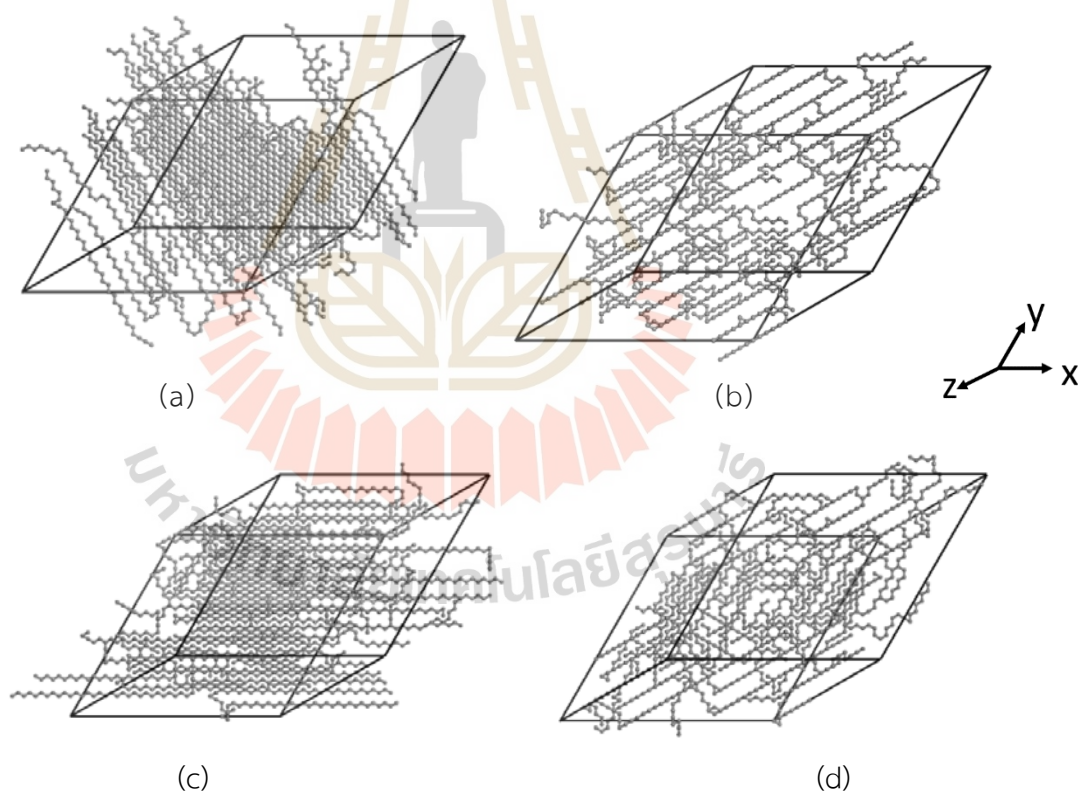


Figure 4.2.3 The final snapshots of PE chains (nanofillers are removed for clarity) at 298 K after 100 million MCS run for (a) S0-bulk (b) S1-nanostick (c) S2-nanoplate and (d) S3-nanosphere systems.

To monitor the change at the molecular level, the evolution of the *trans* conformation of PE chains at each temperature is determined and depicted in Figure 4.2.4. At a lower temperature, the *trans* fraction is usually increased. The magnitudes of *trans* fractions are sharply increased at 350 K except for chains in the S2-nanoplate system where chains can start to increase earlier from 400 K. The fractions of *trans* conformations reach the saturated values at 298 K for all systems. Compared among PNCs, the nanoplate filler can induce the highest magnitude of the *trans* fraction and close to that of the bulk system. In contrast, PE nanocomposite filled with the nanosphere filler induces the lowest amount of *trans* state due to its curve surface of the nanosphere. Their magnitudes can be in the order as S2 (0.87 ± 0.01) \geq S0 (0.86 ± 0.01) > S1 (0.85 ± 0.01) \gg S3 (0.80 ± 0.01) systems. According to these data, the nanosphere filler has the strongest effect on polymer conformation. For the conformational statistics of PE chains, the *trans* content of neat bulk and the S2 system are 86.2% and 86.6%, respectively, which are larger than 84.55% and 80.17% in the S1 and S3 systems. The fraction of *trans* state should be related to the ability of PE chains to form the ordered structure upon crystallization which will be discussed next.

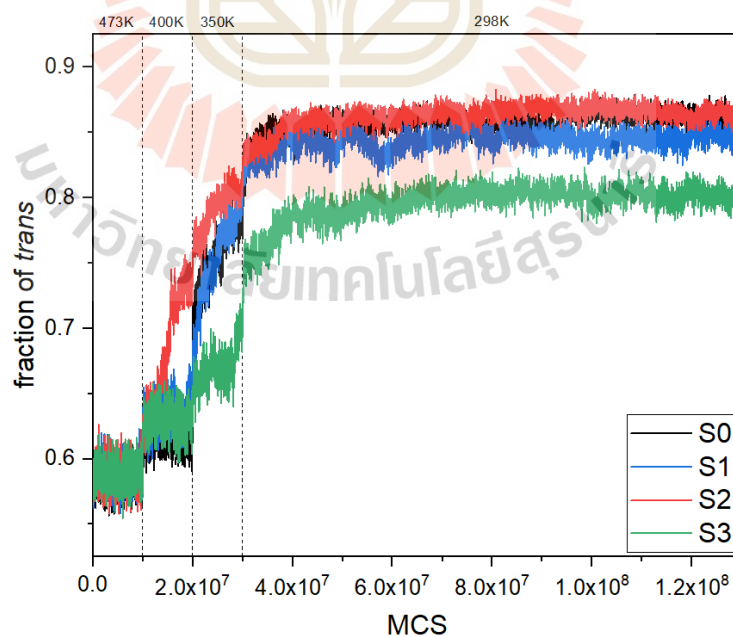


Figure 4.2.4 The evolution of *trans* conformation of PE chains in the neat bulk and with nanofillers of different geometry at 473 K, 400 K, 350 K and 298 K.

4.2.4 Chain dimension

The overall chain dimension was determined in terms of the mean square end-to-end distance, $\langle R^2 \rangle$, and the mean square radius of gyration, $\langle R_g^2 \rangle$, of PE chains in the bulk and PNCs. As shown in Figure 4.2.5(a) – 4.2.5(b), $\langle R^2 \rangle$ and $\langle R_g^2 \rangle$ in most nanocomposites (except spherical nanofiller) start to increase earlier in the order as $S2 > S1 \geq S0 > S3$. Thus, the shape of the nanofiller can impact the growth of the chain stretching such that the nanofiller with planar surface and larger cross-section area can induce better chain elongation.

Chain dimensions calculated at 473 K and 298 K are presented in Table 4.2.1. Both $\langle R^2 \rangle$ and $\langle R_g^2 \rangle$ are given as $\langle X^2 \rangle \pm \Delta X$ where ΔX does not represent the standard deviation, but rather represent the width of the distribution of these properties which the exact definition is $\Delta X = (\langle X^4 \rangle - \langle X^2 \rangle^2)^{1/2}$. The magnitude of $\langle R_g^2 \rangle$ and $\langle R^2 \rangle$ of PE chains for all the systems at 473 K are about the same while there are noticeable different at 298 K with the order similar to Figure 4.2.4 (the fraction of *trans* conformation) as: $S0 \gg S2 > S1 \gg S3$. The theoretical ratio of $\langle R^2 \rangle / \langle R_g^2 \rangle$ for polymer chains should be close to 6 which is the limited value from the theoretical Gaussian model for sufficient long-chain limit (Solc, 1971). Our data in Table 4.2.1 have quite bigger amplitudes because of relatively short chains used in the simulation ($N = 20$ beads or C_{40}). The $\langle R^2 \rangle / \langle R_g^2 \rangle$ ratio determined from the excluded volume (EV) model and MC simulation are presented for comparison. As expected, the EV chain gives the larger $\langle R^2 \rangle / \langle R_g^2 \rangle$ ratio (6.44) than that of the ideal chain model in the long chain limit. Simulation data at 473 K are within the range of 6.3 – 6.5. Nevertheless, simulation data at 298 K give larger values because polymer chains undergo crystallization and adopt more *trans* conformation.

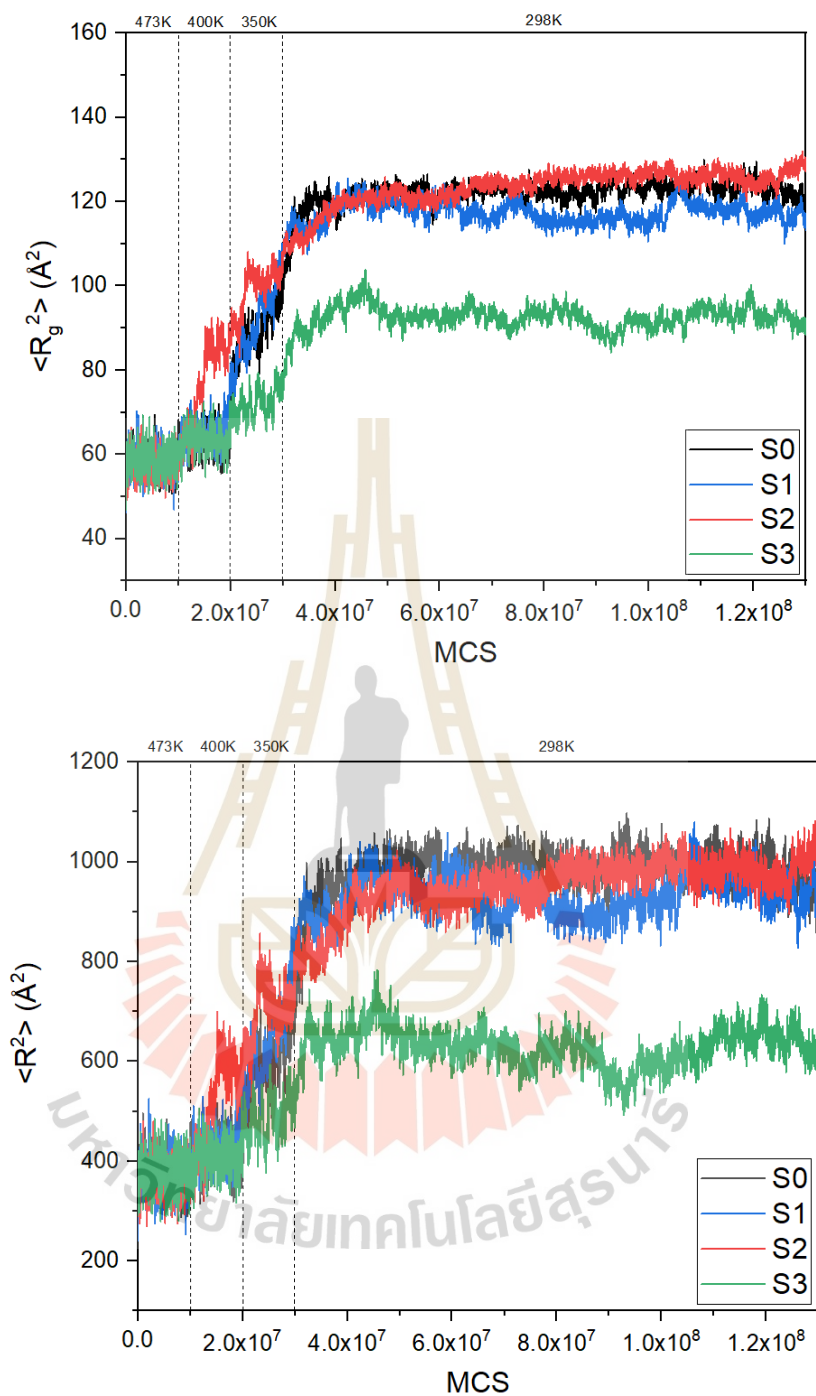


Figure 4.2.5 The evolution of (a) the mean square radius of gyration (b) the mean square end-to-end distance (c) the ratio of the mean square end-to-end distance and the mean square radius of gyration (d) the largest component of the mean square radius of gyration for PE chains in the bulk and nanocomposites (the direction of chain elongation is denoted by x, y or z) at 473 K, 400 K, 350 K and 298 K.

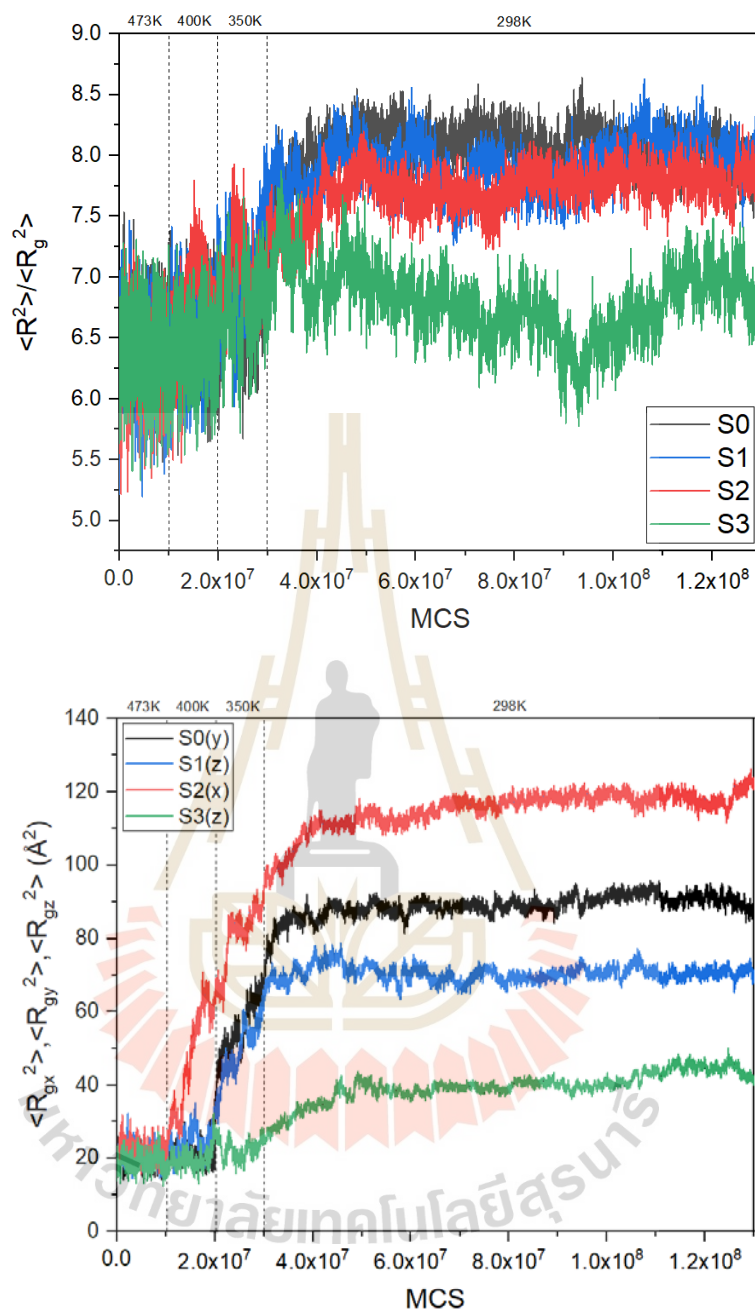


Figure 4.2.5 (Continued) The evolution of (a) the mean square radius of gyration (b) the mean square end-to-end distance (c) the ratio of the mean square end-to-end distance and the mean square radius of gyration (d) the largest component of the mean square radius of gyration for PE chains in the bulk and nanocomposites (the direction of chain elongation is denoted by x, y or z) at 473 K, 400 K, 350 K and 298 K.

Table 4.2.1 The mean square end-to-end distance, $\langle R^2 \rangle$, and the mean square radius of gyration, $\langle R_g^2 \rangle$, for PE chains in the bulk and nanocomposites with different nanofiller geometry.

System identifier	$\langle R^2 \rangle$ (\AA^2)	$\langle R_g^2 \rangle$ (\AA^2)	$\langle R^2 \rangle / \langle R_g^2 \rangle$
473 K			
S0	378.72 ± 251.98	58.35 ± 21.74	6.49
S1	371.80 ± 260.48	58.05 ± 22.79	6.40
S2	362.18 ± 261.38	57.63 ± 23.23	6.28
S3	375.91 ± 257.67	58.50 ± 22.63	6.43
298 K			
S0	984.14 ± 711.54	122.16 ± 49.43	8.06
S1	931.58 ± 727.21	117.53 ± 53.51	7.93
S2	954.35 ± 739.28	123.48 ± 55.27	7.73
S3	630.15 ± 492.18	92.63 ± 37.28	6.80
EV model*	NA	NA	6.44

* EV (excluded volume) model is referred to Eq. (14.36) in Yamagawa book (Modern Theory of Polymer Solutions, Electronic Edition) as $\langle R^2 \rangle / \langle R_g^2 \rangle = 6 (1 + 2z/35 - \dots)$ where z is the excluded-volume parameter which is proportional to the effective excluded volume for a pair of chain elements at infinite dilution and also to the square root of the number of elements in the chain. Here, $z = 134/105$ and $\langle R^2 \rangle / \langle R_g^2 \rangle = 6.44$ which should be the long chain limit.

As polymer molecules can be elongated in different directions upon the crystallization, Figure 4.2.5 presents the x, y and z components of polymer dimension in the laboratory coordinate system ($\langle Rgx^2 \rangle$, $\langle Rgy^2 \rangle$ and $\langle Rgz^2 \rangle$) for the direction where PE chains are stretched the most so that the anisotropic change of chain size can be observed. At 473 and 400 K, these quantities are almost the same in all directions. The chain dimension in S2-nanoplate system starts to increase even at 400 K followed by PE chains in S0-bulk, S1-nanostick and S3-nanosphere systems. The rate of structural formation can be estimated from the slope of an increase in chain dimension. Again, the rate can be arranged in the same manner as $S2 > S0 \geq S1 \gg S3$. $\langle Rgx^2 \rangle$ is increased significantly and reaches the highest value for S2 system while $\langle Rgz^2 \rangle$ of S3 can be increased but with the smallest magnitude. The numerical values of the anisotropic change of chain dimension can be order as $S2 (118.58 \pm 2.08) > S0 (91.07 \pm 1.83) > S1 (70.84 \pm 1.55) > S3 (43.54 \pm 2.04)$. It can be seen that the direction of chain stretching is affected by the shape of nanofiller. From Table 4.2.1, The longest dimensions of each nanofiller are in the z and x/y axes for S1-nanostick and S2-nanoplate, respectively. Consequently, $\langle Rgz^2 \rangle$ and $\langle Rgx^2 \rangle$ are the largest amplitude for PE chains in S1 and S2 nanocomposites. For S0-bulk and S3-nanosphere systems, there are no unique direction of polymer to stretch as the chains can be elongated in different direction as observed in the repeated runs.

4.2.5 Global orientation order parameter

The global intermolecular orientation correlation functions (S_G) used to determine the degree of PE crystallization can be calculated as:

$$S_G = \frac{1}{2} [3\langle \cos^2 \theta \rangle - 1] \quad (4.2.2)$$

Here θ is the angle between two largest molecular axes (L_1) polymer chains, which were represented as the ellipsoid obtained according to 3 molecular axes ($L_1 > L_2 > L_3$) which can be calculated from the radius of the gyration tensor. From Eq. (4.2.2), $S_G = 1$ and 0 for perfect parallel alignment and random orientation of all chains, respectively.

Figure 4.2.6 presents the development of the S_G as a function of MCS. PE chains have random orientations for all systems at 473 K and then the order parameter of the S2-nanoplate system can start to increase even at 400 K. When the temperature reaches 350 K, S_G in S0-bulk and S1-nanostick systems then start to increase. In the final period at 298 K, S_G reach saturated values with the overall magnitudes in the order as $S_0 (0.89 \pm 0.02) \geq S_2 (0.85 \pm 0.02) > S_1 (0.82 \pm 0.02) \gg S_3 (0.33 \pm 0.04)$. Similar to the behavior of chain stretching, the nanofiller with planar surface and larger cross-sectional area can induce better chain alignment during the crystallization compared to other systems.

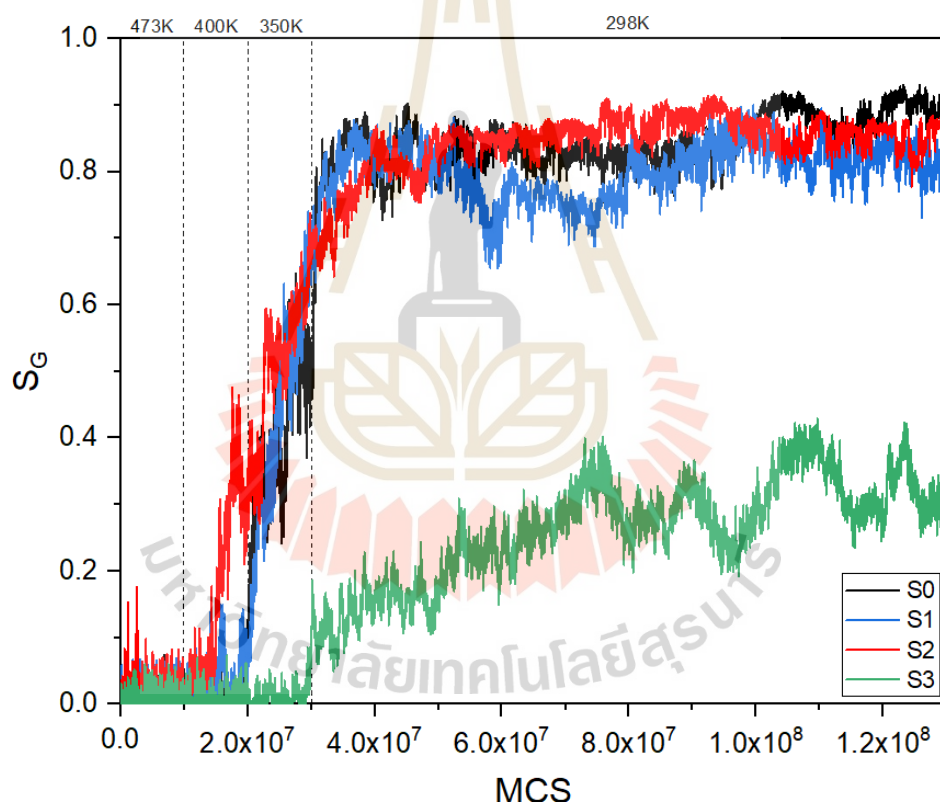


Figure 4.2.6 The evolution of the global orientation order parameter of PE chains in the bulk and PNCs with different nanofillers at 473 K, 400 K, 350 K and 298 K.

4.2.6 Bond orientation correlation function

Upon crystallization, PE chains gain more *trans* conformation and bonds in the chains can have high correlation even at the longer separation. The second order intramolecular bond orientation correlation function is defined to describe the change in the local conformation for chain ordering within the same chains as

$$M_2(j) = \frac{1}{2} [3\langle(m_i \cdot m_{i+j})^2\rangle - 1] = \frac{1}{2} [3\langle\cos^2\psi_{i,i+j}\rangle - 1] \quad (4.2.3)$$

If two bonds are perfectly parallel (the angle ψ between i and $i+j$ bonds is 0°) then M_2 equals to 1. When M_2 become lower than 1, bonds are less ordered arrangement. Figure 4.2.7 presents these functions at 298 K. The bonds in the same chain become more disordered orientation as a function of the separated bond index. The bond disordering as shown by M_2 can be ordered as $S3 > S1 \geq S0 > S2$. These findings suggest that nanofillers with the planar surface can induce bonds in PE chains to have more ordered orientation than other fillers or even bonds in the bulks.

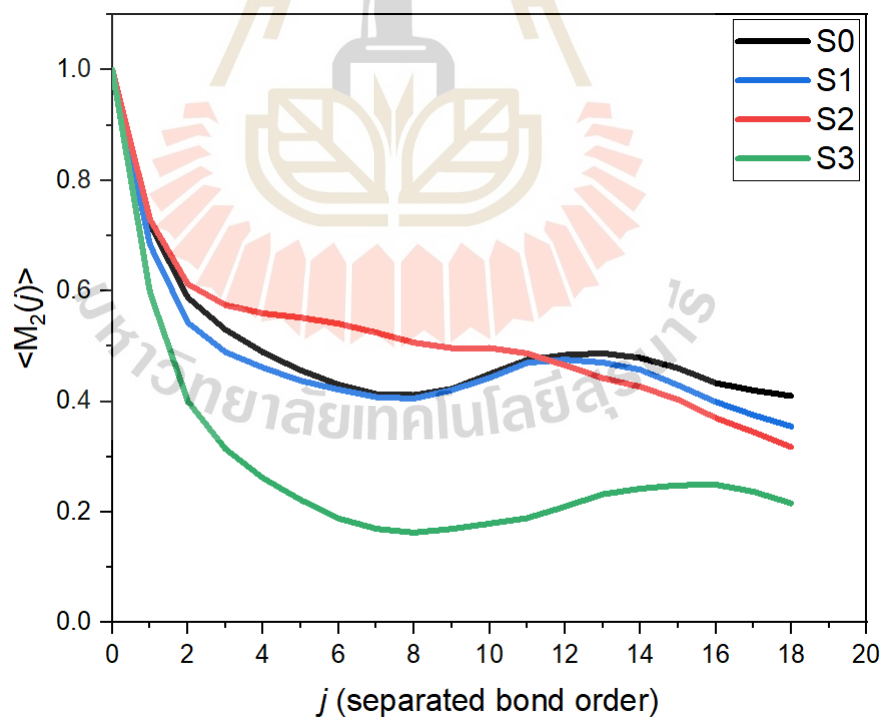


Figure 4.2.7 Intramolecular bond orientation as a function of the separated bond index at 298 K.

In addition to the bond order parameter within the same molecules, the intermolecular bond orientation correlation functions, S_L , determined for bonds in different chains can be calculated as

$$S_L(n) = \frac{1}{2} [3\langle \cos^2 \varphi(n) \rangle - 1] \quad (4.2.4)$$

Here $\varphi(n)$ is the angle for two separated bonds in the n th shell. Figure 4.2.8 depicts these correlation functions at 298 K for all polymer systems. The second shell has the highest magnitudes of S_L indicating bonds tend to have parallel orientation at this distance. For further shell numbers, S_L are systematically decreased as the bonds become more disordered orientation at larger separation. In general, the magnitude of the order parameters for all shell numbers can be ordered as $S_0 \geq S_2 > S_1 \gg S_3$. Thus, the bond ordering for both intra- and intermolecular orientation function in bulk and PNCs exhibits similar trends and are affected by the nature of nanofiller shapes.

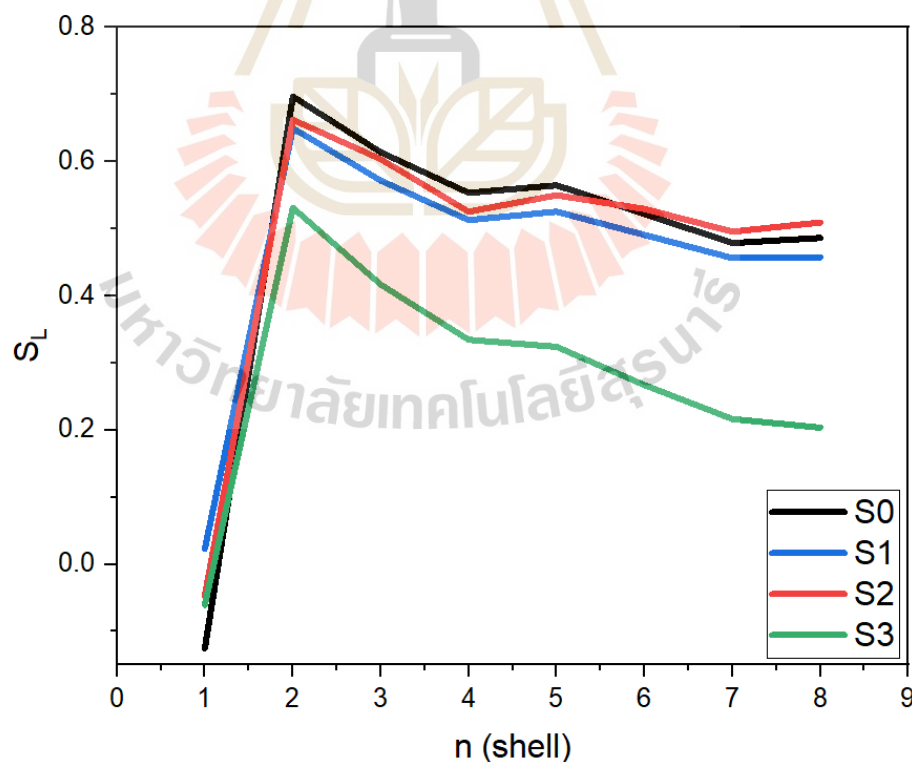


Figure 4.2.8 Local intermolecular bond orientation correlation functions of PE chains in the neat bulk and nanocomposites at 298 K.

4.3 Coarse-grained polymer nanofilm models between impenetrable walls: Effect of surface affinity

4.3.1 Chain dynamics and structural relaxation

Two kinds of dynamic properties are used to determine the equilibration for all systems. The first is the chain's center of mass's (g_{cm}) mean square displacement (MSD) defined as:

$$g_{cm}(t) = \langle [r_{cm}(t) - r_{cm}(0)]^2 \rangle \quad (4.3.1)$$

The coordinates of the chain center of the mass at times t and 0 are represented by the variables $r_{cm}(t)$ and $r_{cm}(0)$, respectively. The angle bracket denotes the ensemble average of the corresponding quantity.

An additional property to determine the equilibration is the orientation autocorrelation function (OACF), which is derived from the end-to-end vector of polymer chain

$$\text{OACF} = \langle R(t) \cdot R(0) \rangle / \langle R^2 \rangle \quad (4.3.2)$$

where $R(t)$ and $R(0)$ are the end-to-end vectors at time t and 0 . $\langle R^2 \rangle$ is the mean square value used to normalize the OACF so that this property is 1.0 at the starting time ($t = 0$).

As seen in Figure 4.3.1(a), the overall MSD increases without limit as the simulation proceed. The slope at long times is related to the diffusion coefficient. In general, polymer chains can be considered to have fully relaxed from their initial conformations when the MSD is larger than the molecular dimension. In our case, this equilibration is achieved when the MSD exceeds the mean square radius of gyration of the chains. The magnitudes of the overall MSDs are ordered as: $20x > 20a > 20r > 20n$. It is interesting to observe that the $20a$ gives a larger overall MSD than $20r$ and $20n$ systems. This is because when the wall becomes more attractive, some polymer chains stay closer to the interface so that the density in the inner region become lower and cause the rest of chains diffuse faster especially in the parallel direction (XY) to the wall. This result is consistent with Figure 4.3.1(b). For the chain mobility in the perpendicular (Z) direction to the wall, Figure 4.3.1(c) shows saturated values of MSD_z

due to confinement effect caused by the solid substrate to limit chain diffusion in this direction. In this case, diffusion of polymer chains in the perpendicular direction to the wall show different trend as: $20a > 20x > 20n > 20r$. The fastest/slowest mobilities for $20a/20r$ systems are due to the lower/higher density in the inner region of the confined polymers caused by the attractive/repulsive wall.

Mean square displacements (MSD) were used to assess structural equilibration when the center of mass of polymers moved larger than the chain dimension. Additionally, the normalized orientation autocorrelation functions (OACF) of the end-to-end vector are also monitored which ought to be smaller than $1/e$ (0.37). As shown in Figure 4.3.1, structural relaxation for PE chains for all systems should be satisfied within 40 million MCS. For OACF as shown in Figure 4.3.1(d), the rate of overall chain reorientation can be ordered as: $20x > 20r \geq 20a > 20n$. As the OACF is averaged from all the chains and there is a competition between the change in polymer densities near the wall and in the inner region. The behavior of the OACFs for $20r$ and $20a$ systems are difficult to correlate with the nature of polymer-wall interaction.

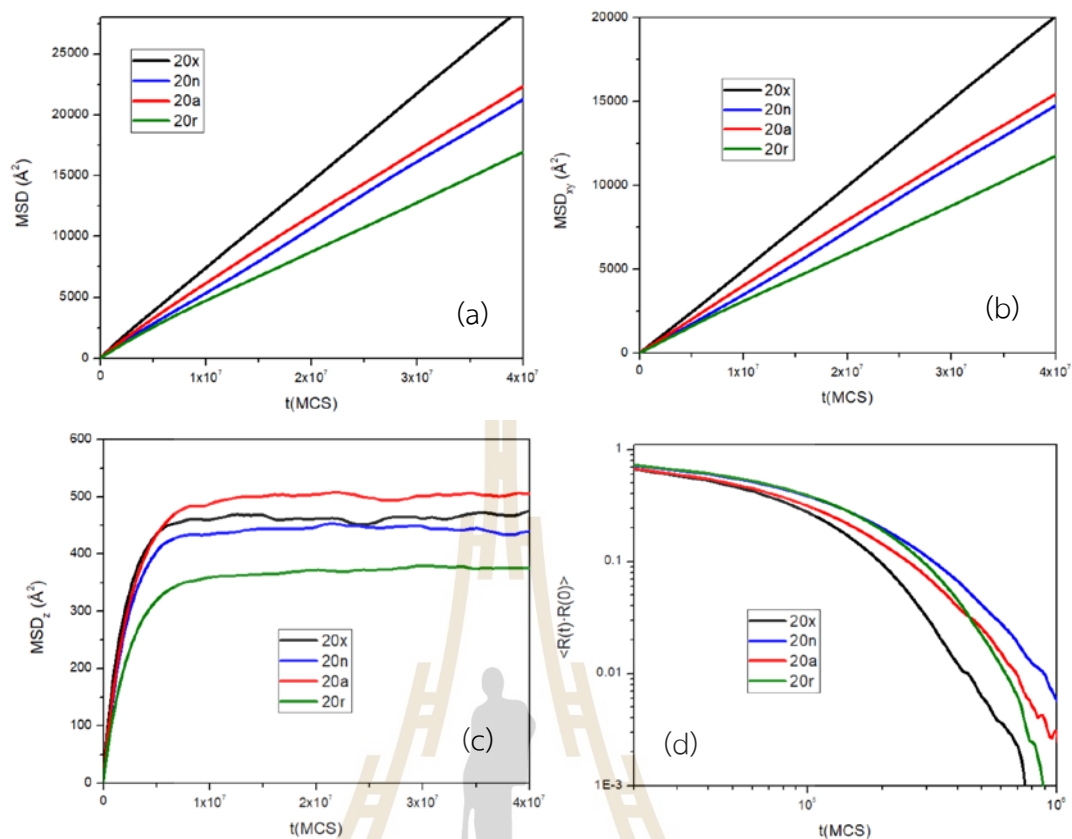


Figure 4.3.1 (a) The overall mean square displacement of the chain center of the mass (MSD) (b) in the parallel direction to the wall, MSD_{xy} (c) in the perpendicular direction to the wall, MSD_z and (d) the orientation autocorrelation functions (OACF) of the chain end-to-end vector.

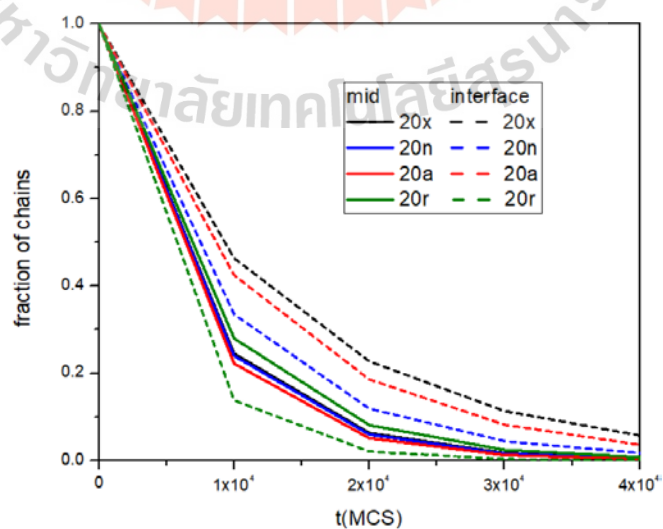


Figure 4.3.2 Fraction of the centers of mass of polymer chains which stay in their original bin in the middle and interface regions as a function of MCS.

Figure 4.3.2 shows the fraction of chains that stay in the same bin as a function of MCS, by looking at the center of mass of each chain in comparison between chains in the middle position and near the wall. In the bulk region (solid lines), there are slightly difference for all systems. In contrast, chains in the interface region (dashed lines), the fraction of chains within the same bin is decayed differently and can be order as: 20x (slowest) < 20a < 20n < 20r (fastest).

Figure 4.3.3 shows the comparison of the rotational diffusion of chains in the middle and interface regions as a function of MCS. The chain rotational diffusion should be enhanced in the lower density region. The result shows that chains in 20r and 20x systems in the innermost bulk region (solid lines) have a longer residence time compared to the chains near the interface especially for 20r system because the repulsive wall push polymers to the bulk region so that chains move slower due to higher density. For 20a and 20n systems, polymers in the interface region have longer residence time compared to bulk region as a result of the lower density near the interacting walls especially for 20a system. The rotational diffusion of chains can be order as: 20n (slowest) < 20a < 20r < 20x (fastest) in the interface region whereas different pattern can be seen in the bulk region as: 20r (slowest) < 20n = 20r < 20a (fastest) due to the local density effect.

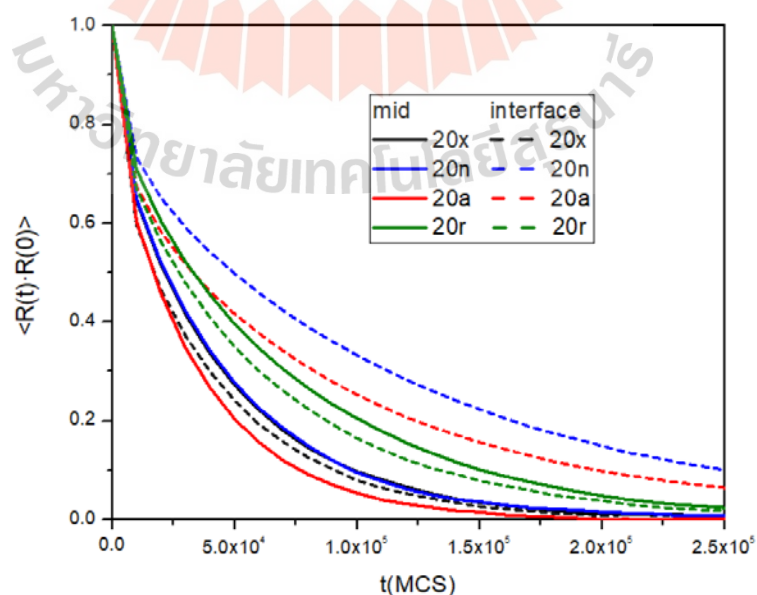


Figure 4.3.3 Normalized end-to-end vector autocorrelation function of the chains starting in middle and interface regions as a function of MCS.

The chain center-of-mass displacement may be subject to anisotropy imposed by the interfaces. As a result, the perpendicular (Z direction, normal to the contact) and lateral (average of X and Y directions, parallel to the interface) components of diffusion will be taken into account independently. It is possible to compute the "apparent diffusivity" in both the parallel and perpendicular directions as

$$\begin{aligned} D_Z^{\text{app}} &= \left(\frac{1}{2} t_f\right) \langle [Z_{c.m.}(t+t_f) - Z_{c.m.}(t)]^2 \rangle \\ D_{XY}^{\text{app}} &= \left(\frac{1}{4} t_f\right) \langle [XY_{c.m.}(t+t_f) - XY_{c.m.}(t)]^2 \rangle \end{aligned} \quad (4.3.3)$$

Here, $XY_{c.m.}$ and $Z_{c.m.}$ is the (X, Y) and Z coordinate of the chain center of mass and t_f is an arbitrary final time. Referred to Figure 4.3.3, at least half of the beads in each bin remain in that bin for the duration of the process, $t_f = 10,000$ MCS appears to be appropriate for this use. The center-of-mass displacements in the X and Y directions are averaged to determine the apparent diffusivity parallel to the surfaces, or D_{XY}^{app} .

Figure 4.3.4(a) shows the chain diffusion in the perpendicular direction to the wall (D_Z^{app}). The maximum density in the middle region and near the wall can be ordered as: $20x > 20a > 20n > 20r$ and $20x > 20r > 20n > 20a$, respectively. For $20a$ and $20n$, the diffusion is steadily increased until the maximum at the middle region of the confined films. For $20x$ and $20r$ systems, diffusion near the interface is enhanced followed by dropping to the minimum points and then increasing again until they reach the highest values in the bulk region. Compared to other systems, the highest diffusion is seen near the wall and in the bulk region for $20x$. For $20a$ and $20r$, slower diffusion is seen for polymers near the wall.

Figure 4.3.4(b) shows the diffusions in the parallel direction to the wall (D_{XY}^{app}) which exhibit the convex curves for $20x$ and $20r$ but concave curves for $20a$ and $20n$ systems. Polymer diffusion is increased progressively from the wall and reaches the maxima in the middle for the inert and repulsive walls. In contrast, polymer diffusion is decreased continuously from the wall and reaches the minima in the middle for the attractive and normal walls. The maximum density in the middle region and near the wall can be ordered as: $20a > 20x > 20r > 20n$ and $20x > 20n > 20a \geq 20r$, respectively. The increased/decreased diffusion rates should be related to the decreased/increased densities caused by the nature of wall interaction.

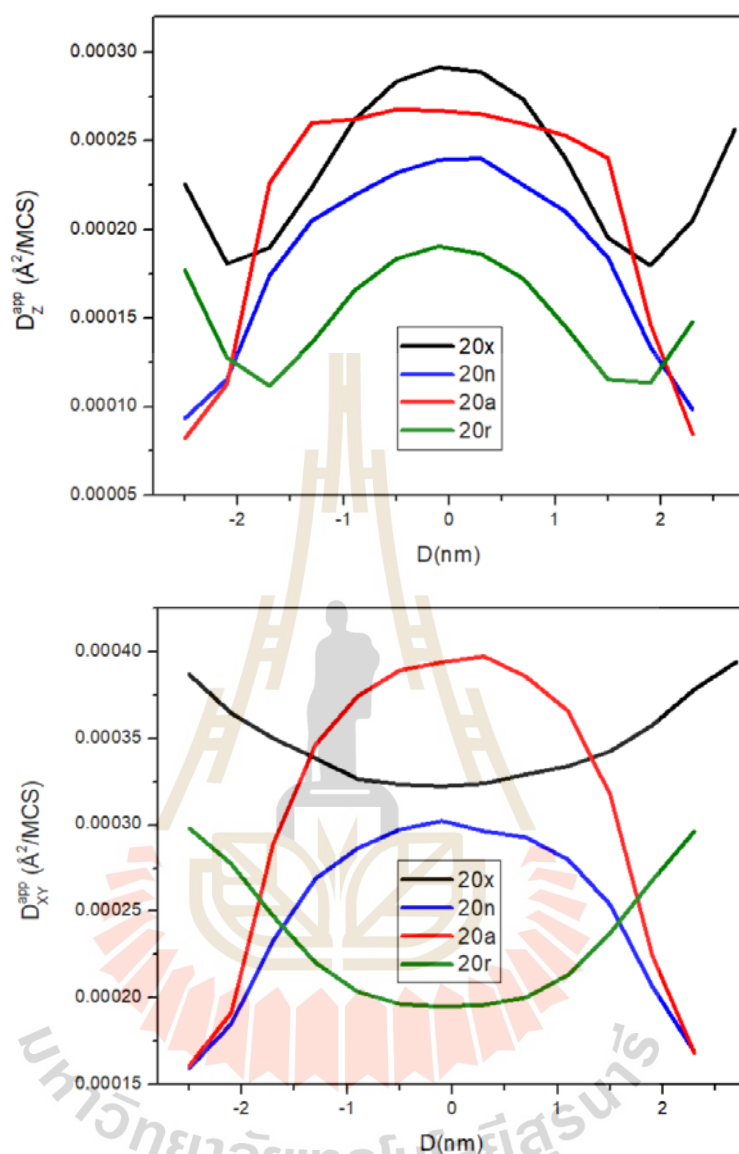


Figure 4.3.4 Apparent diffusivity in different bins of polymer film (a) D_z^{app} and (b) D_{xy}^{app} .

4.3.2 Density profiles

The representative structures of polymer and impenetrable walls with different polymer-wall interactions (in the order of the magnitude for polymer-wall interaction parameters, $w = 0.0$ (inert), 0.1 (repulsive), 1.0 (neutral), 2.0 (attractive)), are depicted in Figure 4.3.5. In general, when the substrate has stronger polymer-wall interaction, the confined films become denser, and more beads can stay closer to the wall. For weaker polymer-wall interaction, chains tend to stay more in the middle region. Next, the

density profiles are then calculated by finding the number of beads in each bin volume averaged for all trajectories as a function of the distance from the wall (Z). The density profiles of the confined PE structures with different polymer-wall interactions are compared in Figure 4.3.6.

The monomer density profile displays a significantly fluctuating structure in all systems, which may be explained by the depletion of the area near the wall caused by the loss of configurational entropy for chains approaching an impenetrable wall. However, collisions with chains farther from the interface also exert an effective average force on polymers, which pack them against the wall. Because of the excluded volume interaction, the enhancement near the wall causes the monomer density in the layer that follows to decrease, making possible for another enhancement in the subsequent layer. This sequence of enhanced and reduced monomer densities continues over a few lattice constants until the bulk value is recovered.

The density profiles demonstrate that the intensity of the density oscillations close to the wall rises significantly with increasing polymer-wall interaction except for 20x which is the inert wall that causes polymer arrangement near the surface. On the other hand, the densities in the bulk region are decreased as a function of the polymer-wall interaction and they are relatively constant for most of the system except 20a which has the strongest wall attraction. The arrangement of polymer chains to stay closer near the wall can be ordered as: $20x > 20a > 20n > 20r$.

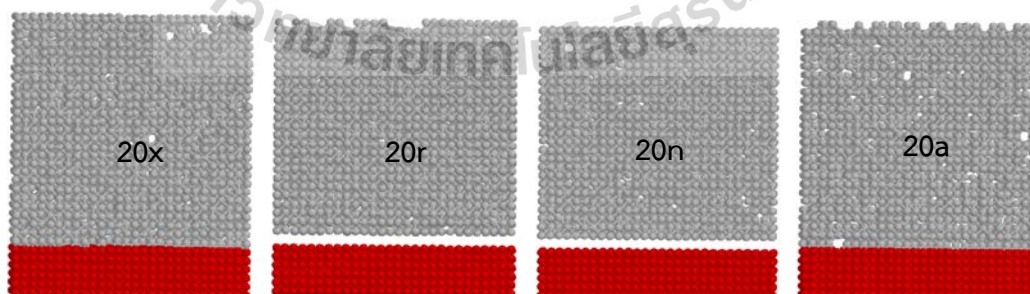


Figure 4.3.5 The representative snapshots of polymer-wall systems with different polymer-wall interactions, $w = 0.0$ (inert), 0.1 (repulsive), 1.0 (neutral), 2.0 (attractive). Grey and red colors are for the polymer and wall, respectively (the above walls are omitted due to periodic boundary conditions).

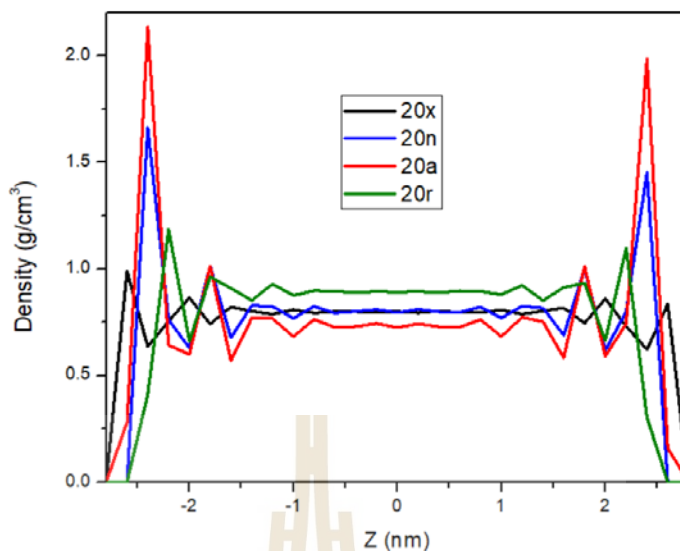


Figure 4.3.6 Density profiles of confined PE nanofilms with different wall interactions.

In addition to the bead distribution in polymer nanofilms, the distribution of polymer as the whole chain can be evaluated using the spatial distribution for the center of mass of polymer calculated by counting the number of chains per bin volume. As seen in Figure 4.3.7, the results are quite consistent with monomer density profiles. When the walls have stronger polymer-wall interaction, there is more tendency for higher chain distribution near the interface ($20r < 20x \leq 20n < 20a$), while the magnitude of chain distribution is lower in the bulk region ($20a < 20x \leq 20n < 20r$).

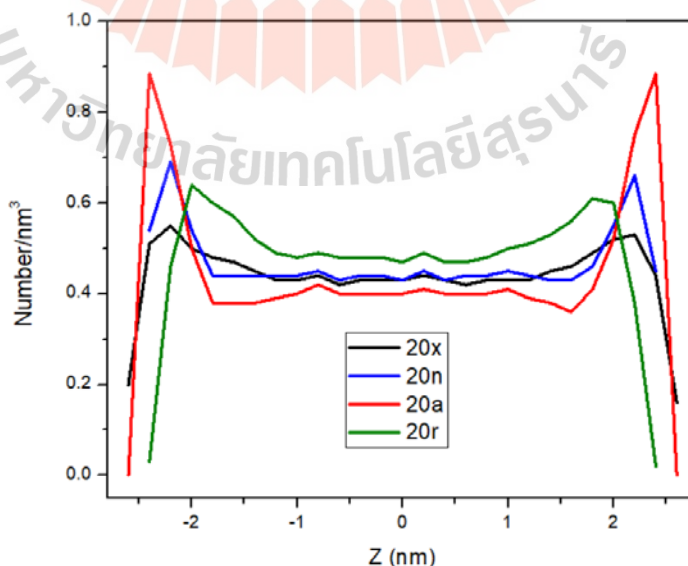


Figure 4.3.7 The distribution of chain center of mass for the confined polymers between two interactive walls.

Figure 4.3.8 shows the normalized middle- and end-bead distributions of polymer chains with various polymer-wall contacts, which may be used to study the distribution of monomer beads at different positions inside polymer molecules. Both bead densities have similarly dispersed magnitudes in the bulk area. Conversely, the middle bead profiles decrease while the end bead densities greatly rise when approaching the wall. For walls with stronger attraction, the segregation of end beads near the wall tends to enhance but the middle beads are more depleted. Since end beads often require a higher free volume and have faster mobility, it is preferable to place them close to the interface.

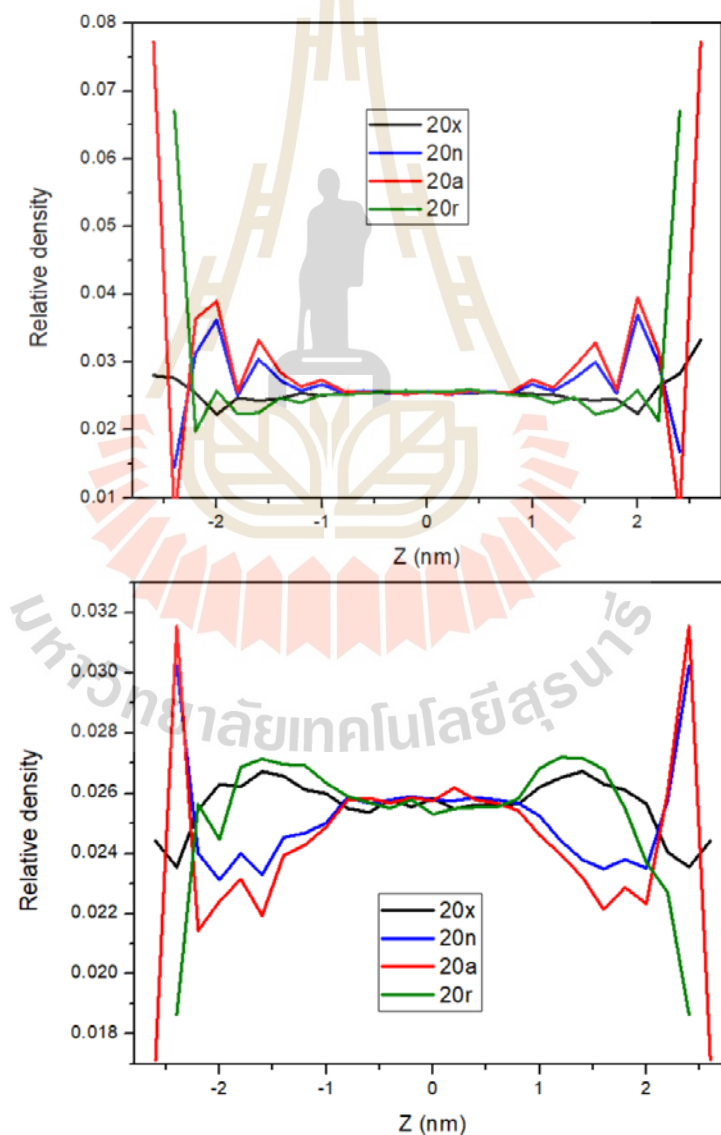


Figure 4.3.8 (a) Normalized end-bead and (b) middle-bead densities in the confined polymer films between two interactive walls.

4.3.3 Bond orientation

To characterize the bond arrangement inside the confined polymer structures, the bond order parameter, S_b , is calculated from

$$S_b = \frac{\langle 3\cos^2\theta - 1 \rangle}{2} \quad (4.3.4)$$

where θ is the angle between a bond vector with respect to the normal vector of the interface. $S_b = -0.5$, 0.0 and 1.0 when the bonds are parallel, random, and perpendicular orientations, respectively, to the wall. Figure 4.3.9 shows that the middle and end bonds of PE chain are randomly oriented in the bulk region inside the film structures. Nevertheless, near the surface, there is the tendency for bonds to orient parallel to the interface ($20n > 20x > 20r$) except the case for the attractive wall which the bonds prefer to orient normal to the wall.

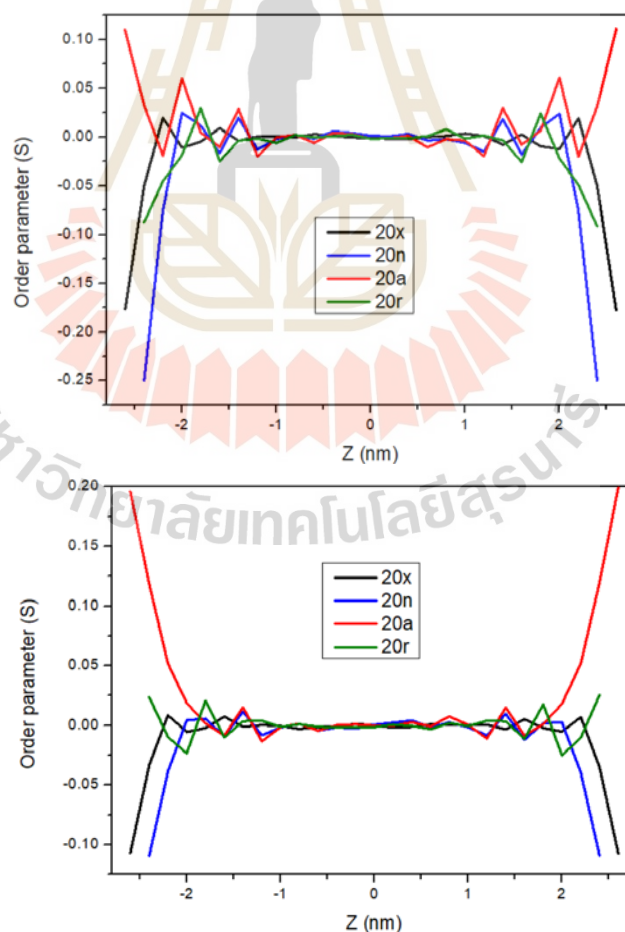


Figure 4.3.9 The local orientation of (a) the middle bonds and (b) the end bonds of PE chains with different wall interaction.

4.3.4 Chain properties

To evaluate the distortion of chain dimension inside confined polymer structures as a result of polymer-wall interactions, the mean square end-to-end vector, $\langle R_e^2 \rangle$, and the mean square radius of gyration, $\langle R_g^2 \rangle$, of polymer chains are calculated as presented in Table 4.3.1. Compared to chains in 20x (no wall interaction), the chain dimension tends to decreased for all kinds of polymer-wall interaction (20x > 20n > 20r > 20a). The theoretical ratio of $\langle R_e^2 \rangle / \langle R_g^2 \rangle$ should be 6.0 for the infinite chain length. However, these ratios are larger due to rather short chain length (20 monomers) used in this simulation.

In addition, a polymer chain can be approximated by an ellipsoidal shape defined according to three principal axes ($L_1 > L_2 > L_3$) which can be determined from the radius of the gyration tensor. For the freely jointed chain model, the $L_1^2 : L_2^2 : L_3^2$ ratio was theoretically estimated as 11.7 : 2.7 : 1 (Solc, 1971). The acylindricity ($c = L_2^2 - L_3^2$) and asphericity ($b = (L_1^2 - (L_2^2 + L_3^2))/2$) are calculated to determine how much polymer chain is deviated from the cylindrical and spherical shape and presented in Table 4.3.1. The $L_1^2 : L_2^2 : L_3^2$ ratios, the acylindricity and the asphericity from simulation data are in reasonably agreement with theoretical prediction.

To study the anisotropic change of chain dimension inside the confined polymer structures, Figure 4.3.10(a) and 10(b) depict the radius of the gyration component of polymer chains (XY and Z are the average components in the same and normal direction to the wall surface). In the interior of polymer films, these two components are almost equal and close to $(\langle R_g^2 \rangle / 3)^{1/2} \approx 4.49$. When chains are approached to the wall, the XY components significantly increase while the Z components are relatively decrease. These results suggest that polymer chains are elongated in the parallel direction to the wall but are contracted at the same time in the perpendicular direction. The changes in XY and Z components of polymer chain with different surface affinity near the surface are clearly seen as they are more perturbed due to the wall affinity. In parallel direction, the magnitude of chain stretching/shrinkage in the parallel/perpendicular direction near the wall tend to be more pronounced for more repulsive wall (20r > 20n > 20x > 20a).

Figure 4.3.10(c) presents the change in the longest and shortest principal axes normalized by $\langle R_g^2 \rangle$ of the confined polymer structures. L_1 is increased whereas L_3 is decreased. Both quantities are relatively constant in bulk region while L_1/L_3 is increased/decreased near the wall surface. The magnitudes of *principal axes* in all regions can be ordered as: $20r > 20n > 20x \approx 20a$ indicating chains are elongated in this direction for more repulsive wall.

Table 4.3.1 The mean square end-to-end vector, the mean square radius of gyration, the ratio of three principal axes, the acylndricity and asphericity of confined polymer chains between two walls.

Chains	$\langle R_e^2 \rangle$ (Å^2)	$\langle R_g^2 \rangle$ (Å^2)	$\langle R_e^2 \rangle / \langle R_g^2 \rangle$	$\langle L_1^2 \rangle : \langle L_2^2 \rangle : \langle L_3^2 \rangle$	$\langle c \rangle / \langle R_g^2 \rangle$	$\langle b \rangle / \langle R_g^2 \rangle$
20x	405.25 ± 270.75	62.07 ± 23.07	6.53	11.59:3.47:1.00	0.243	0.919
20n	396.37 ± 272.34	61.80 ± 23.56	6.41	11.03:3.38:1.00	0.228	0.846
20a	377.01 ± 258.47	58.90 ± 22.45	6.40	11.52:3.48:1.00	0.240	0.899
20r	385.23 ± 260.45	59.49 ± 22.46	6.48	10.83:3.27:1.00	0.216	0.828

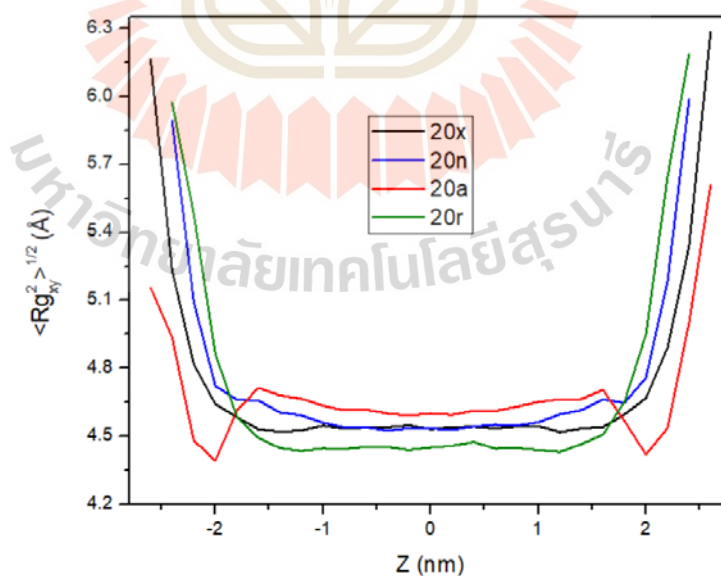


Figure 4.3.10 (a) The parallel (XY) and (b) the perpendicular (Z) components of the mean-squared radius of gyration and (c) the longest (left y-axis) and the shortest principal axes (right y-axis) of polymer chains confined between two hard walls with different polymer-wall interaction.

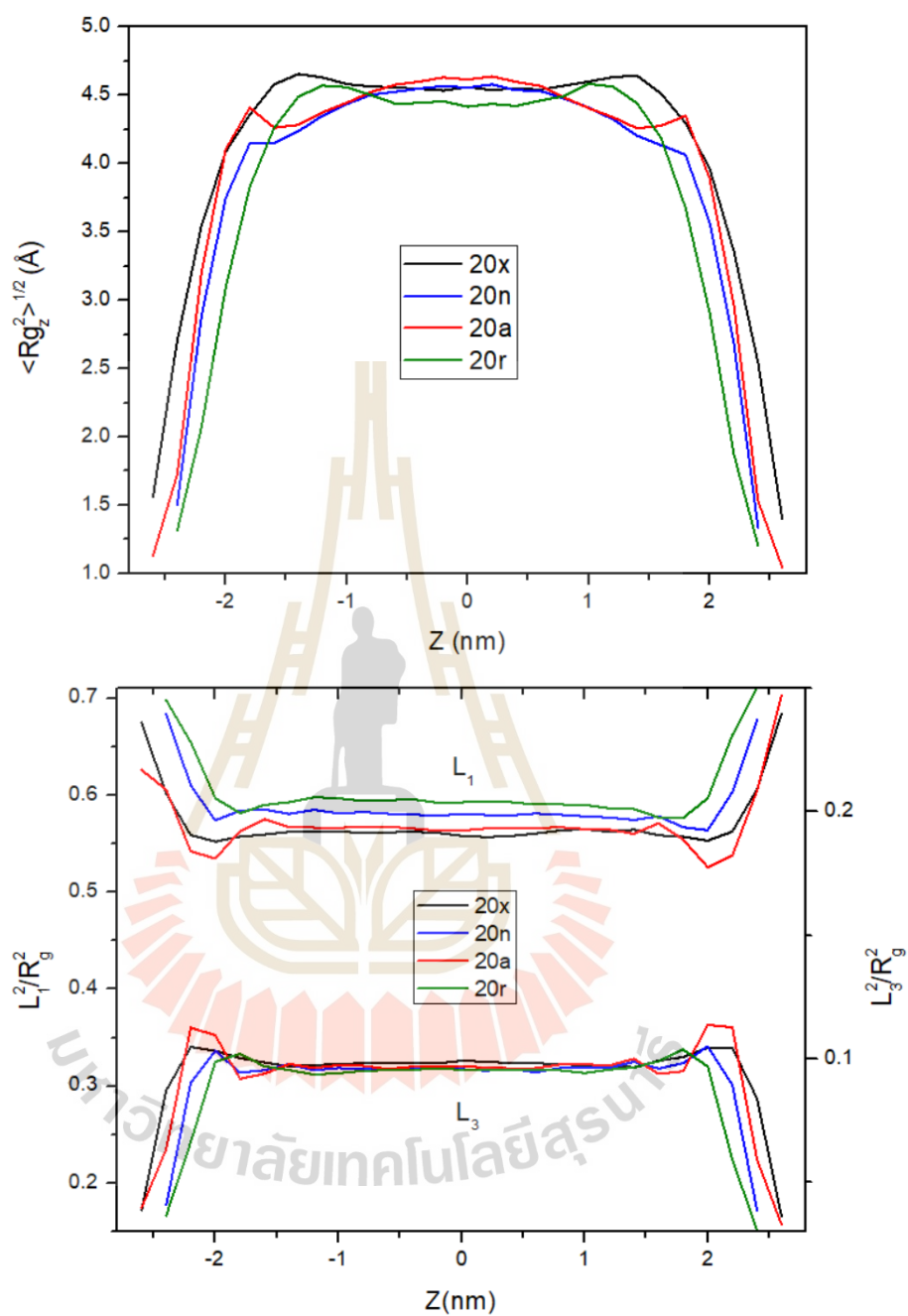


Figure 4.3.10 (Continued) (a) The parallel (XY) and (b) the perpendicular (Z) components of the mean-squared radius of gyration and (c) the longest (left y-axis) and the shortest principal axes (right y-axis) of polymer chains confined between two hard walls with different polymer-wall interaction.

4.3.5 Chain orientation

Similar to the definition of the bond orientation in Eq. (4.3.3), the orientation at the whole chain can be determined using the principal axes to represent the chain vector. Figure 4.3.11 presents the order parameter of the longest ($L1$) and the shortest ($L3$) axes relative to the normal vector of the wall. In the middle region of confined structures, both principal axes are not likely random orientation. The magnitude of $L1$ and $L3$ are in the range of -0.1 to -0.2 and $+0.1$ to $+0.2$, respectively indicating that the longest and shortest axes tend to have perpendicular and parallel direction to the wall surface.

When polymer chains are approached to the wall, $L1/L3$ tends to align more anisotropic arrangement in the perpendicular/ parallel direction to the wall surface. The relative magnitudes of chain orientation become more anisotropic for the more repulsive wall ($20r > 20n > 20a \geq 20x$).

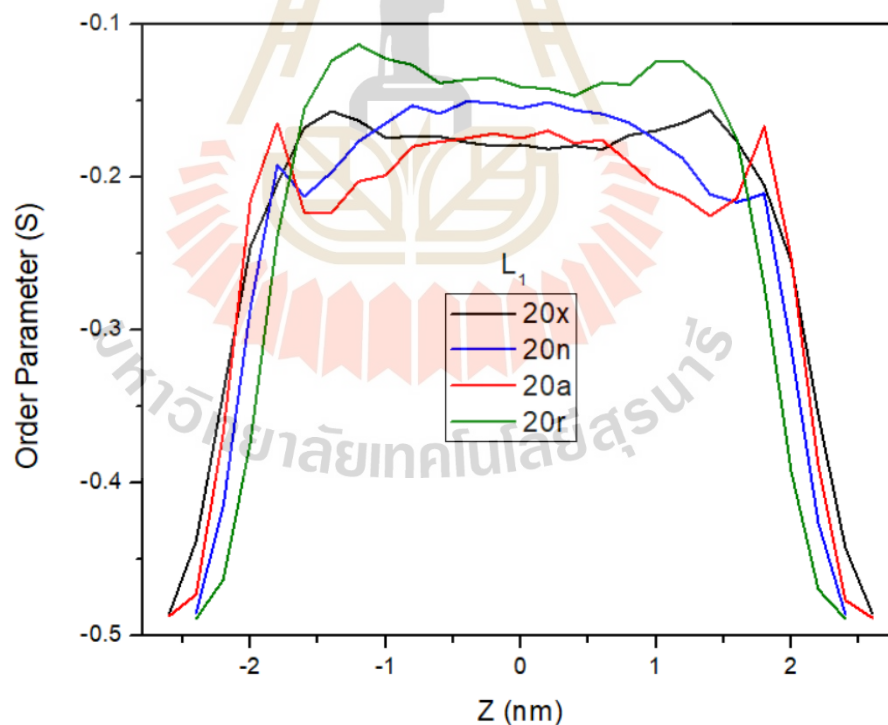


Figure 4.3.11 The order parameter of (a) the longest and (b) the shortest principal axes of polymer chains confined between two hard walls with different polymer-wall interaction.

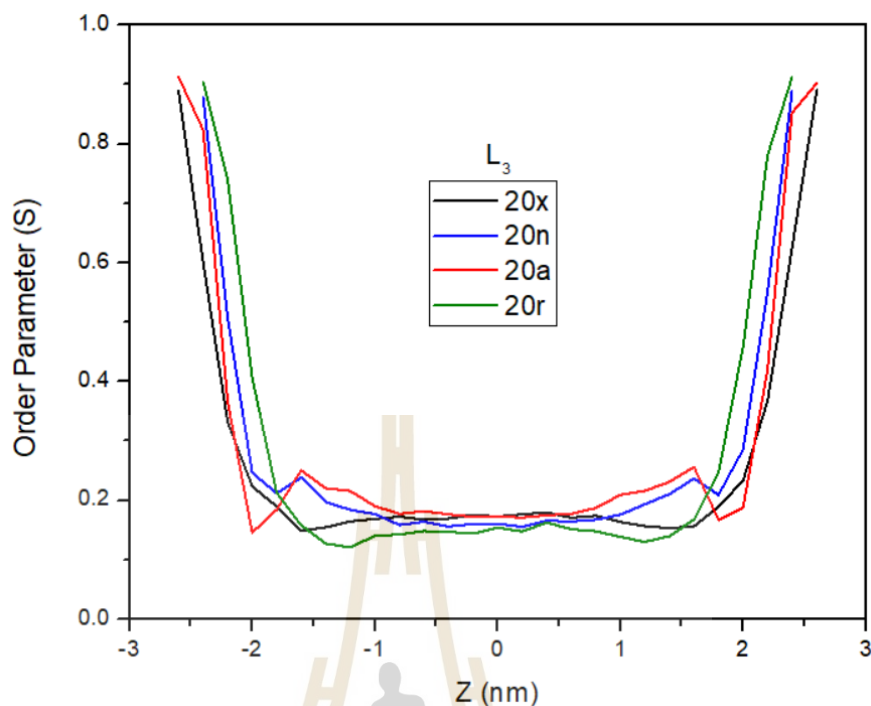


Figure 4.3.11 (Continued) The order parameter of (a) the longest and (b) the shortest principal axes of polymer chains confined between two hard walls with different polymer-wall interaction.

4.3.6 Energetics

The intra- and intermolecular energies of the confined polymer structures between two walls with different polymer-wall interaction are presented in Figure 4.3.12. In the bulk region, there is the systematic difference for intrachain energies in the order: $20r > 20x \approx 20n > 20a$. The lower intrachain energies are related to more *trans* conformation in the PE chains. Hence in the inner region, chains confined by the more repulsive wall can adopt more *trans* conformation. On the other hand, the existence of segment-wall attraction enhances the intrachain energy near the wall surface, as a result of attractive force induce *gauche* conformation.

Since the decreased magnitude of intermolecular energies is related the better chain packing, chains in the inner region with more *trans* conformation should be packed better and have lower intermolecular energies. In the bulk region, the intermolecular energies are lower for the chains confined by more repulsive wall as

they have more *trans* conformation. Near the wall surface, the the more attractive wall causes polymer chains to have more *gauche* conformation with less efficient chain packing so that both intra- and intermolecular energies become higher.

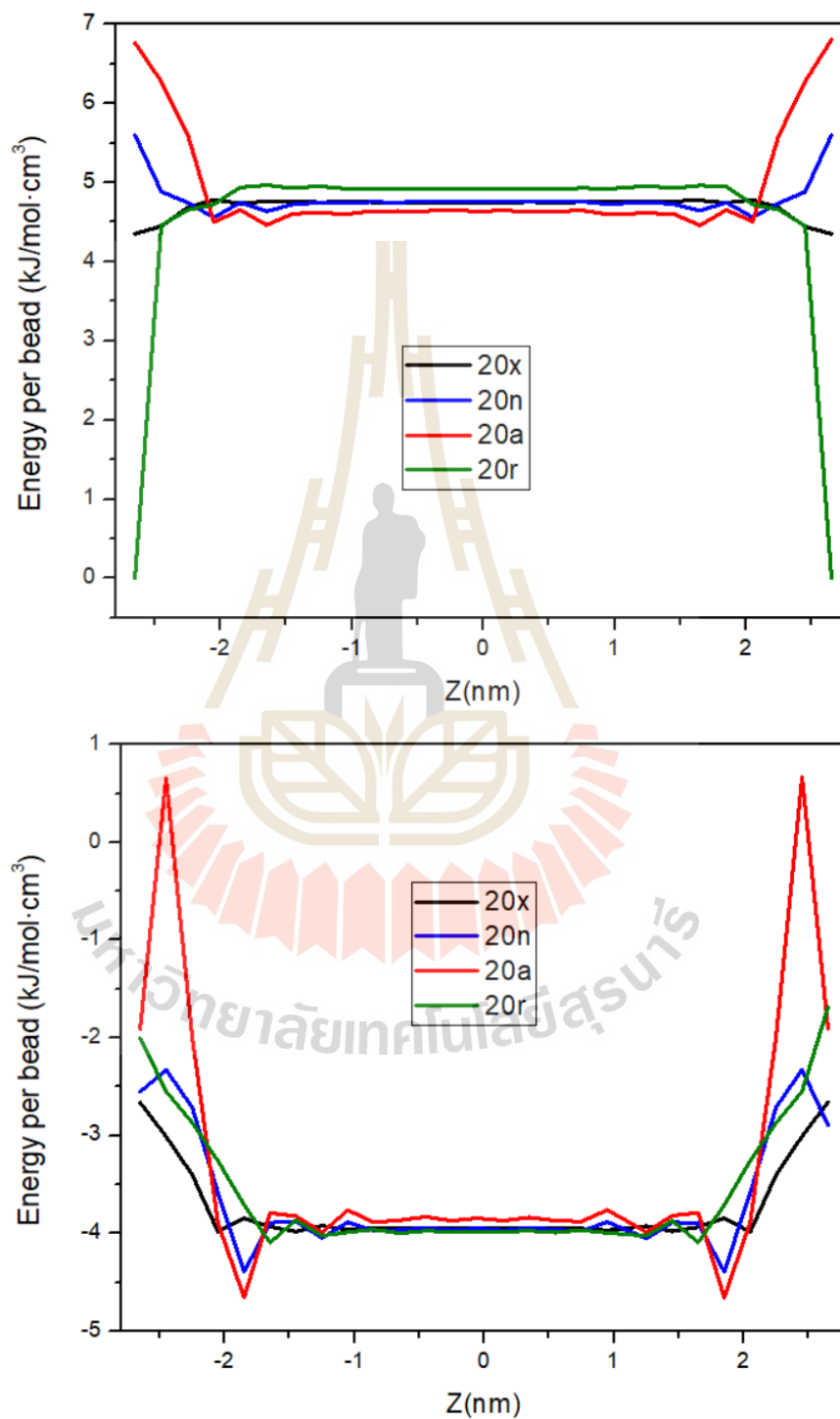


Figure 4.3.12 The average (a) intramolecular and (b) intermolecular energies of the confined polymers between two hard walls with different polymer-wall interaction.

4.4 Monte Carlo simulation of coarse-grained PPO model

4.4.1 Structural equilibration

There are two kinds of dynamic characteristics used to evaluate the equilibration. One is the mean square displacement of the center of the mass (MSD). Another property is the orientation autocorrelation function (OACF) formulated from the end-to-end vector as mentioned in Chapter 4.2

As seen in Figure 4.4.1(a), MSD increases without limit as the simulation continues. The slope at long times is related to the diffusion coefficient. In general, polymer chains can be considered to have fully relaxed from their initial conformations when MSD is larger than the molecular dimension *i.e* about two times the root mean square radius of gyration of polymer chains ($2\langle R_g^2 \rangle^{1/2} \approx 19.8 \text{ nm}^2$).

The normalized orientation autocorrelation functions (OACF), which are derived from the end-to-end vector, can also be used to track the equilibration of the conformations of the chains. Within 50 million MCS, the reorientation is finished, as Figure 4.4.1(b) illustrates.

The PPO model should to be fully equilibrated based on the results of MSD and OACF. Then the reverse-mapping back to the fully atomistic PPO models was performed using a selected final structure from MC simulation on the lattice. Figure 4.4.2 illustrates the final structures for the CG model before the reverse-mapping and the fully atomistic model of PPO after geometry optimization.

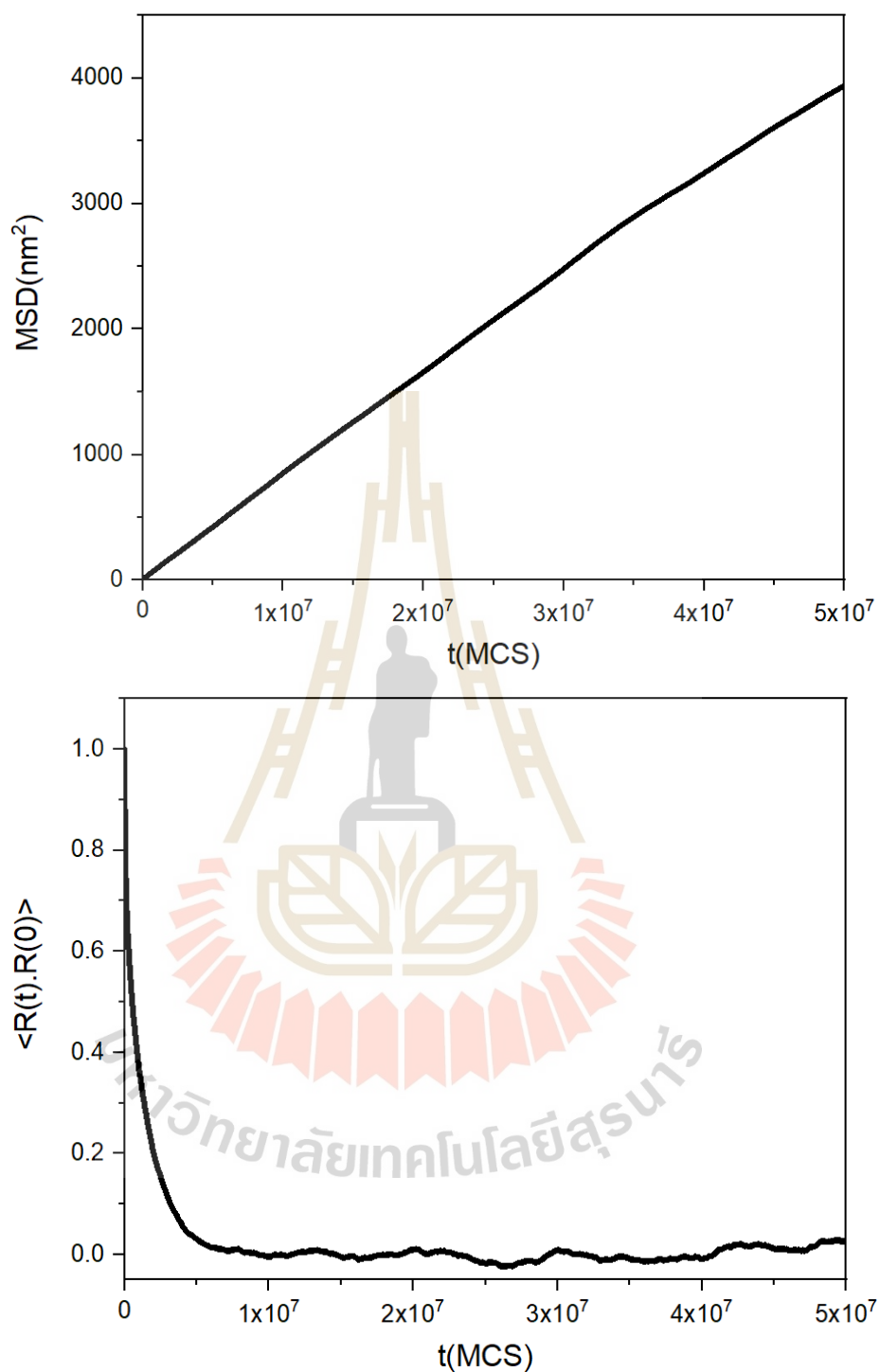


Figure 4.4.1 (a) The mean-square displacement for the chain center of mass and (b) The orientation autocorrelation functions (OACF) of the end-to-end vector of PPO models at 1000K for 50 million MCS.

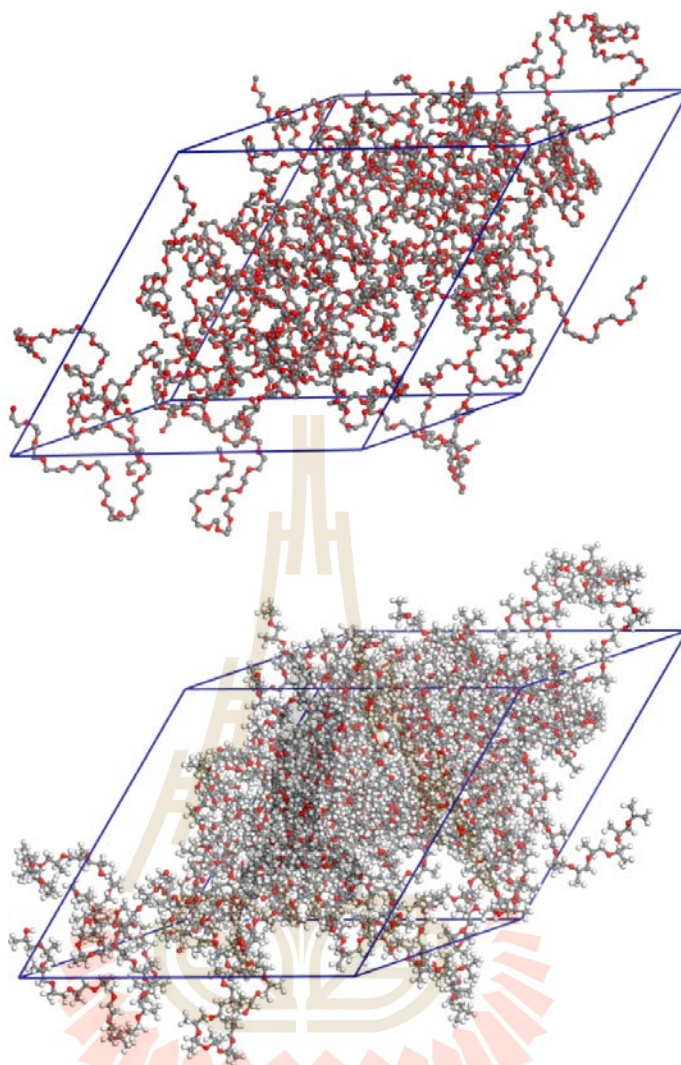


Figure 4.4.2 Example of the snapshot of (a) coarse-grained and (b) fully atomistic PPO models.

4.4.2 Conformational dependent properties of PPO

Some conformational dependent properties, such as the mean square unperturbed end-to-end distance and the mean-square unperturbed dipole moment (expressed as $\langle r^2 \rangle_0/nl^2$ and $\langle \mu^2 \rangle_0/nm^2$, respectively), can be predicted using the RIS model with statistical weight matrices obtained in this work. The number of skeletal bonds is represented by n , and the average values of the square of their bond lengths and dipole moments are represented by l^2 and m^2 , respectively.

From Table 4.4.1, the characteristic ratio, $C_n = \langle r^2 \rangle_0 / nl^2$ (at 323 K) for PPO determined from Sasanuma models gives a slightly smaller C_n compared to the experimental result. For the dipole moment ratio, $\langle \mu^2 \rangle_0 / nm^2$, values close to experimental data.

Table 4.4.1 Comparison of various PPO conformation-dependent characteristics calculated and actual values.

	Medium	$\langle r^2 \rangle_0 / nl^2$ (323 K)	$\langle \mu^2 \rangle_0 / nm^2$ (308 K)
This work Sasanuma (3x3)	-	5.30	0.31
Experiment	isooctane	6.01 (Allen, 1967)	
	C_6H_6		0.47 (Hirano, 1979)
	C_6H_{12}		0.52 (Hirano, 1979)

4.4.3 Chain dimension

The mean square radius of gyration ($\langle R_g^2 \rangle^{1/2}$) and the mean square end-to-end distance ($\langle R_E^2 \rangle^{1/2}$) can be used to calculate the molecular dimension. The findings are shown in Table 4.4.2. All parameters for PPO become larger as most atoms can be displaced to off-lattice positions after the reverse-mapping with geometry optimization through energy minimization followed by structural refinement with 1 ns NVT-MD simulation. The simulation ratio of $\langle R_E^2 \rangle / \langle R_g^2 \rangle$ for CG (fully atomistic) models with $N = 45$ are 5.97 (6.01) and very closed to the theoretical Gaussian model where $\langle R^2 \rangle / \langle R_g^2 \rangle$ approaches 6 for sufficient long-chain limit (Flory, 1969).

Table 4.4.2 The mean square end-to-end distance ($\langle R_E^2 \rangle^{1/2}$), The mean square radius of gyration ($\langle R_g^2 \rangle^{1/2}$) and the characteristic ratio (C_n) of PPO models.

Chain properties	On-lattice structure of coarse-grained PPO model	Geometry optimization of the fully atomistic model (energy minimization + NVT-MD simulation)
$\langle R_E^2 \rangle^{1/2}$ (nm ²)	24.19	27.03 ± 0.352
$\langle R_g^2 \rangle^{1/2}$ (nm ²)	9.90	11.02 ± 0.075
$\langle R^2 \rangle / \langle R_g^2 \rangle$	5.97	6.01

4.4.4 Conformational statistics

Usually, the torsional angle values provide a description of the conformational states of the polymer chain. Prior to the reverse mapping, the conformations of C*-C, O-C*, C-O bonds (the notation C* is used for the chiral carbon atom) are limited to the discrete states at g^+ , t and g^- (60° , 180° , and 300°), due to the underlying diamond lattice. During the geometry optimization, the torsional angles can displace from lattice sites and conformational distribution become continuous. The distribution of three different types of dihedrals along the main chain are presented and compared between CG and fully atomistic model of PPO are presented in Figure 4.4.3 and the population for each conformation state are determined and listed in Table 4.4.3.

For the fully atomistic model after geometry optimization, the torsional angles around the O-C* bonds prefer the *trans*-conformation which is dominating with 69% and while the C-O bond adopts about 40% of *trans* but with 54% predominant for the *gauche*⁺ state (the population are determined from the integrated areas after energy minimization of fully atomistic model). Around the C*-C bond, almost equal population of the dihedrals are in the *trans* (36%) and *gauche*⁺ (40%) state and the rest is in the *gauche*⁻ conformations. Data for bond population are also calculated for comparison

by the RIS a-priori probabilities of a single PPO chain. RIS results have similar trends and the amplitude for bond population. The difference in the bond population between RIS and fully atomistic models should be a consequence of the non-bonded interaction due to the methyl group in the side chain that are not present explicitly in the RIS calculations.

The explanation for preferred conformational states for backbone bond is that the methyl side groups make the chiral carbon atom have bulkier group compared to the oxygen atoms. This repulsive interaction causes the *gauche* state become less favorable for the O-C* bond. For C*C-OC* dihedral, the *trans*- and *gauche*⁺-conformation are dominated probably because of the steric and *gauche* oxygen effect. Thus, the relative stability for the conformation of the OC*-CO bond can be seen as: $g^+ \geq t > g^-$. Note that this tendency is observed by NMR data studied by Hirano (1972) and Oguni (1973). These results imply that the PPO model generated by this simulation method is consistent with experimental data for the bond conformation.

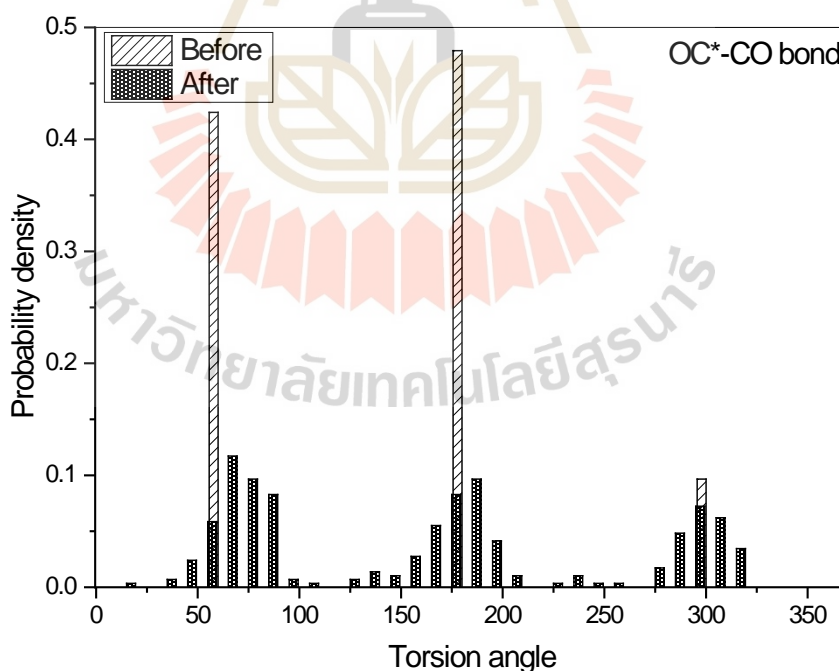


Figure 4.4.3 Population of the backbone torsional angles for the CG and fully atomistic PPO models at the bulk density during the reverse-mapping step before and after geometry optimization.

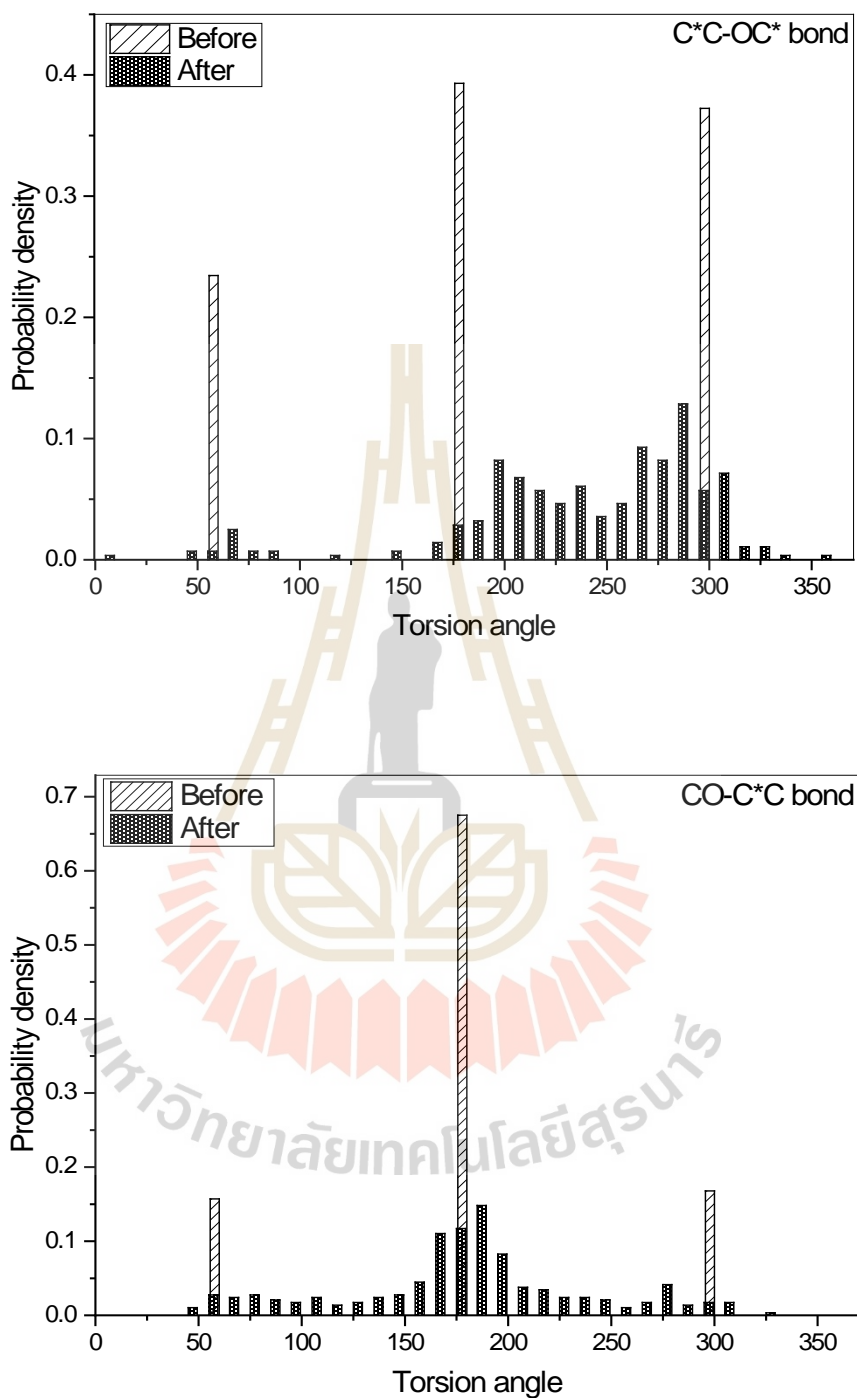


Figure 4.4.3 (Continued) Population of the backbone torsional angles for the CG and fully atomistic PPO models at the bulk density during the reverse-mapping step before and after geometry optimization.

Table 4.4.3 Population of the conformational states for PPO models.

	Bonds	Conformations		
		g^+	t	g^-
CG model (This work)	OC*-CO	0.42	0.48	0.10
	CC-OC	0.23	0.39	0.37
	CO-C*C	0.16	0.68	0.17
Fully atomistic model (This work)	OC*-CO	0.40	0.36	0.24
	CC-OC	0.06	0.40	0.54
	CO-C*C	0.17	0.69	0.14
RIS (Sasanama)	OC*-CO	0.49	0.40	0.11
	CC-OC	0.01	0.44	0.55
NMR (Hirano)	CO-C*C	0.07	0.88	0.06
	OC*-CO	0.52	0.38	0.10
NMR (Oguni)	OC*-CO	0.44	0.40	0.16

4.4.5 Solubility Parameters

By taking the square root of the cohesive energy density, one can determine the Hildebrand's solubility parameter (δ) from the completely atomistic model.

$$\delta = (\text{CED})^{1/2} = \left[\frac{U_{\text{coh}}}{V} \right]^{1/2} \quad (4.4.1)$$

Where V is the volume of the simulation box. The cohesive energy, or U_{coh} , may be estimated from the difference between the total energy of the model in the periodic box and that of the parent chains. After reverse-mapping and minimizing energy, the completely atomistic PPO models Hildebrand solubility parameter at the bulk density is $16.05 \pm 0.05 \text{ J}^{1/2}/\text{cm}^{3/2}$, which is close to the experimental value (Morales, 1996) of commercial PPO ($16.17 \text{ J}^{1/2}/\text{cm}^{3/2}$) at room temperature. In general, the calculated solubility parameters are quite sensitive to the quality of the forcefield used in the calculation of atomistic model especially the non-bonded interaction. Nevertheless, the calculated values from PPO models are very close to the experimental data and the simulation has a high level of confidence because the standard deviations are of small magnitude.

4.4.6 Structures

The radial distribution function (RDF) function can be used to characterize the structure of amorphous polymers and represented into total, inter- and intramolecular components. The intra- and intermolecular RDF gives information about polymer conformation and molecular arrangement in the amorphous structure, respectively.

Since PPO contains three different atomic species (C, H, and O), six distinct pair distribution functions can be established. Six alternative pairs of elements RDFs (C...C, C...O, O...O, O...H, C...H and H...H) for the atomistic PPO model were calculated and shown in Figure 4.4.4(a) - (f). The total RDF for C...C, C...O, and O...O, exhibit some sharp peaks at $r < 4 \text{ \AA}$, and reach 1.0 for $r > 5 \text{ \AA}$.

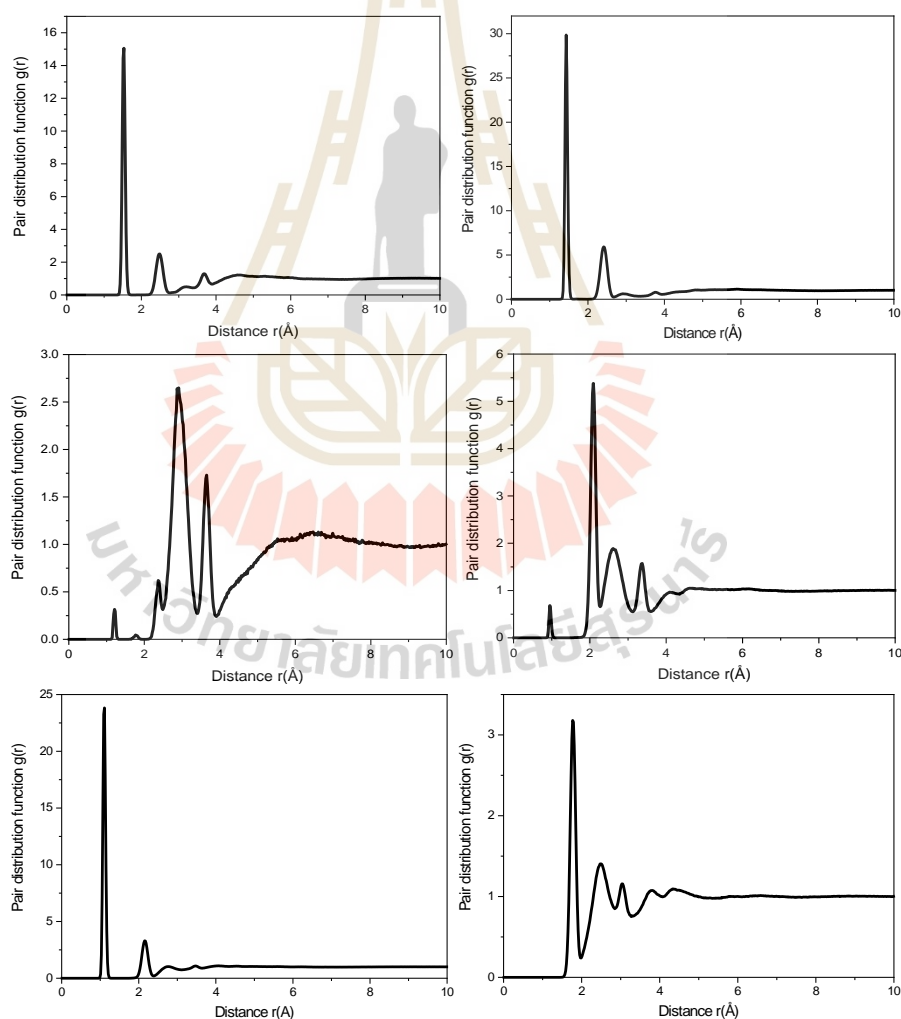


Figure 4.4.4 The total radial distribution function for different pairs of elements (a) C...C, (b) C...O and (c) O...O (d) O...H (e) C...H (f) H...H.

4.4.7 Scattering

The calculated X-ray and neutron scattering were determined and compared with the data published by Ahlstrom (2000) in order to validate the structure of the fully atomistic model of amorphous PPO at the bulk density with experiments. The heavy atoms have the largest atomic form factors in the case of X-ray scattering, and the various carbon and oxygen correlations contribute the majority of the scattering data. The enormous variation in coherent neutron scattering length between the two hydrogen isotopes causes a significant disparity in the associated static structural factors. On the other hand, neutron diffraction is more sensitive to the hydrogen content. By Fourier converting the entire RDF, the measured static structural factors can be evaluated from the simulation data. For X-rays scattering, Figure 4.4.5 presents the comparison between the calculated scattering curves of PPO models which exhibits good agreement to reproduce all the experimental data. The five experimental peaks are at $q = 1.35, 2.89, 5.58, 8.84$ and 10.53 \AA^{-1} and the five simulation peaks are at $q = 1.38, 3.15, 5.46, 8.82$ and 10.71 \AA^{-1} . For Neutron scattering, the models also show that the calculated profiles are in good agreement except the last two peaks. The six experimental peaks are at $q = 1.33, 5.10, 8.72, 10.67, 14.03$ and 16.64 \AA^{-1} and the six simulation peaks are at $q = 1.26, 5.15, 8.45, 10.52, 13.66$ and 17.01 \AA^{-1} .

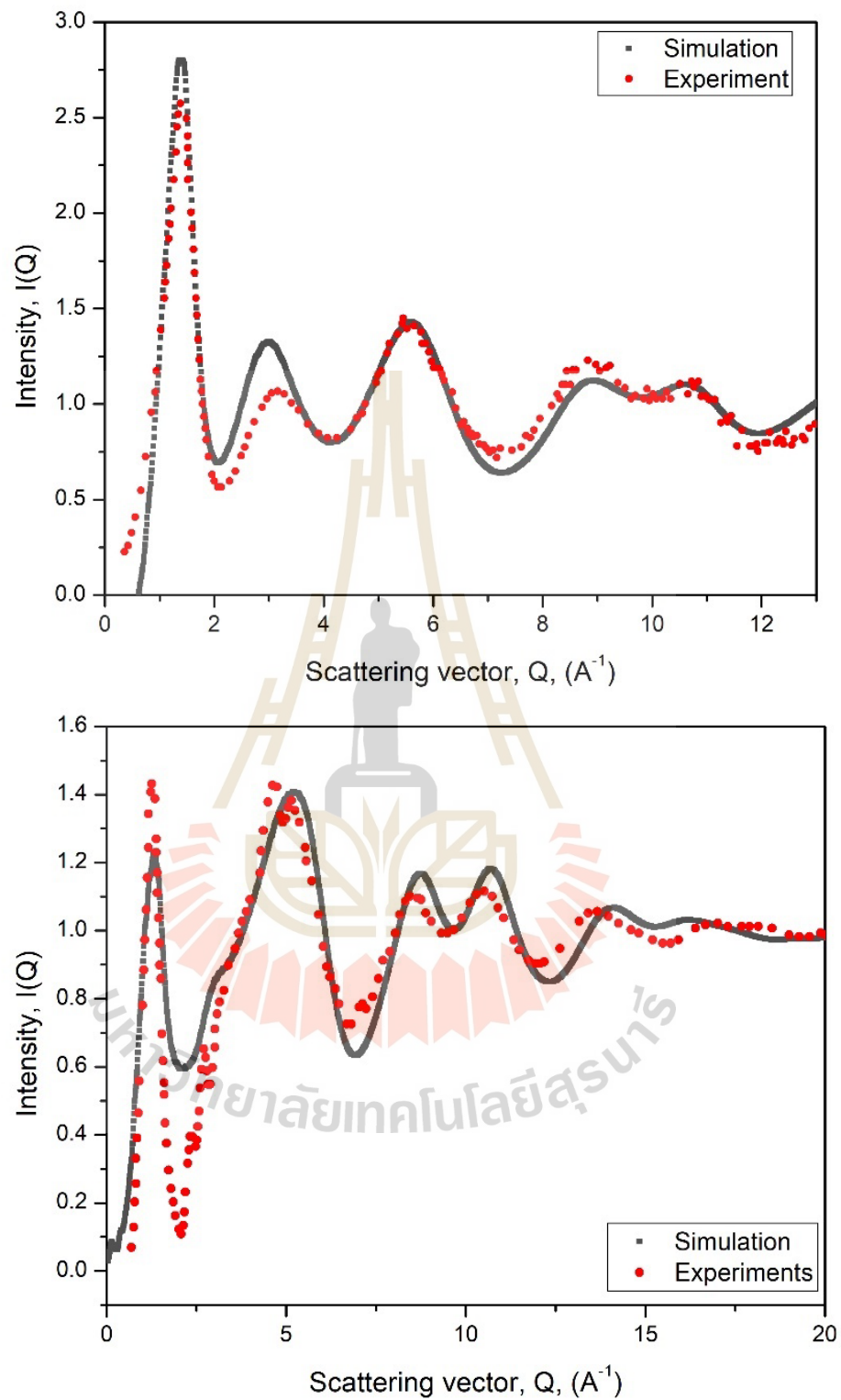


Figure 4.4.5 (a) X-rays and (b) Neutron scattering for PPO model.

4.4.8 Dynamics of alkaline metal salts in PPO

The dynamic behavior of alkali metal ions, Li^+ and K^+ in polymer matrix is one of the most important topics in solid polymer electrolytes. Since it is important to understand dynamic movement of cation over the whole battery. In order to see the properties of polymer electrolytes, the LiSCN and KSCN were added in polymer atomistic PPO model. The MD simulation were used to generate the trajectory at 373 K and study the properties of salt in the PPO matrix. Figure 4.4.6 presents the mean-square displacement (MSD) of Li^+ ion, K^+ ion, oxygen in PPO chains and anions. At the beginning, polymer (O) were high dynamic. But over time, the ion tends to diffuse faster. The movement of cations and anions in the LiSCN system tend to be higher than KSCN.

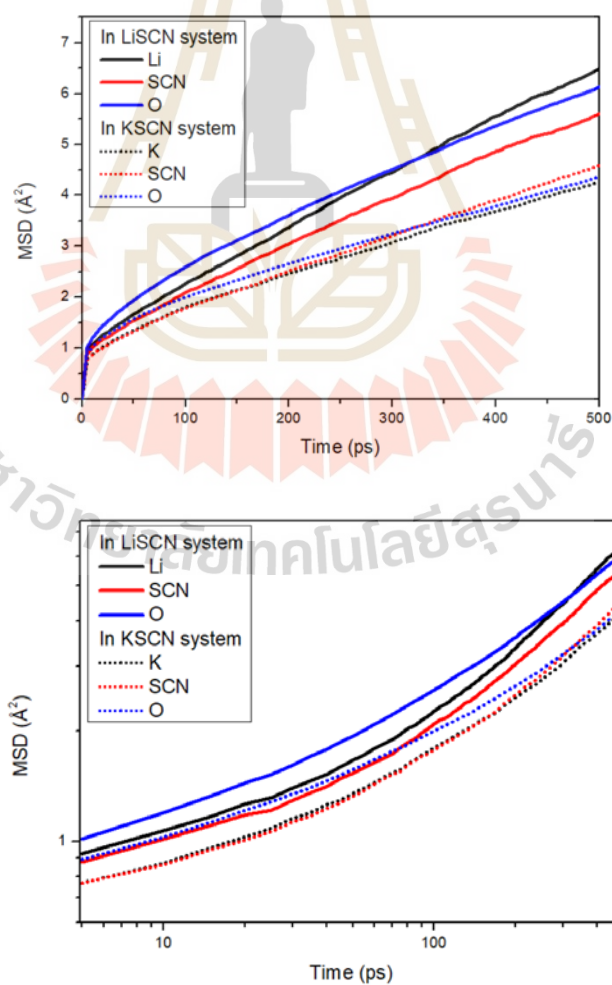


Figure 4.4.6 The mean square displacement of alkaline metal salts in PPO.

4.4.9 Structure of Alkaline Metal Salts in PPO

Based on the radial distribution functions (RDF) between the atoms and solvated ions, we first analyze the ion solvation structures (Li^+ and K^+) of the PPO chains, $g_{XY}(r)$, where $X = \text{Li}^+$ or K^+ and $Y = \text{O}_{\text{PPO}}, \text{S}_{\text{SCN}}, \text{C}_{\text{SCN}}$ or N_{SCN} . For the purpose of characterizing the ion solvation, the average ion-atoms distance, or r_X is an important parameter. As shown in Figure 4.4.7, the position and width of the $g_{XY}(r)$ first maximum follows the order: $\text{K}^+ > \text{Li}^+$. For example in Table 4.4.4, r_{XO} yielded values of 2.67 and 1.95 Å for K^+ and Li^+ , respectively. This ordering represents the trend in the ion radius and exhibits an increase in the size of the first solvation shell from Li^+ to K^+ . In order to better characterize the solvation geometries, we then analyze the distributions of N_{XO} , the oxygen coordination number in these PPO systems, in the first ion solvation shell. Our findings indicate that N_{XO} grows in proportion to the size of the ion solvation shell, with typical values for Li^+ and K^+ are 3.35 and 5.28, respectively.

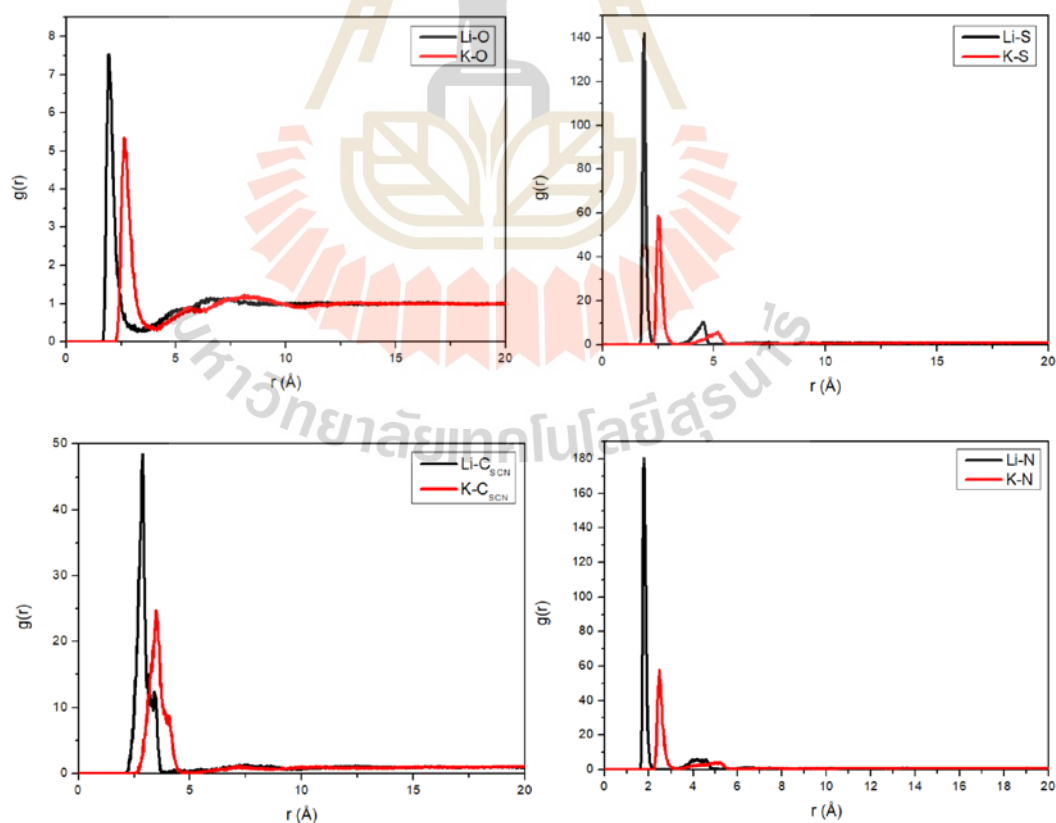


Figure 4.4.7 Ion-atoms radial distribution functions in PPO chains.

The results are consistent with the work on solvation in water (Savoj, 2024) and solvation in Ethylene Carbonate (EC) (Pham, 2017), where ion solvation in PPO is lower since the dimensions in PPO chains are higher.

Table 4.4.4 Parameter characterizing the first peak of RDFs.

Correlation	Li ⁺ -O _{PPO}	K ⁺ -O _{PPO}
r_{xO} (Å) in PPO (This work)	1.95	2.67
N_{xO} in PPO (This work)	3.35	5.28
r_{xO} (Å) in water (Savoj, 2024)	1.93	2.73
N_{xO} in water (Savoj, 2024)	4.1	6.7
r_{xO} (Å) in EC (Pham, 2017)	1.95	2.80
N_{xO} in EC (Pham, 2017)	4.0	7.6

CHAPTER V

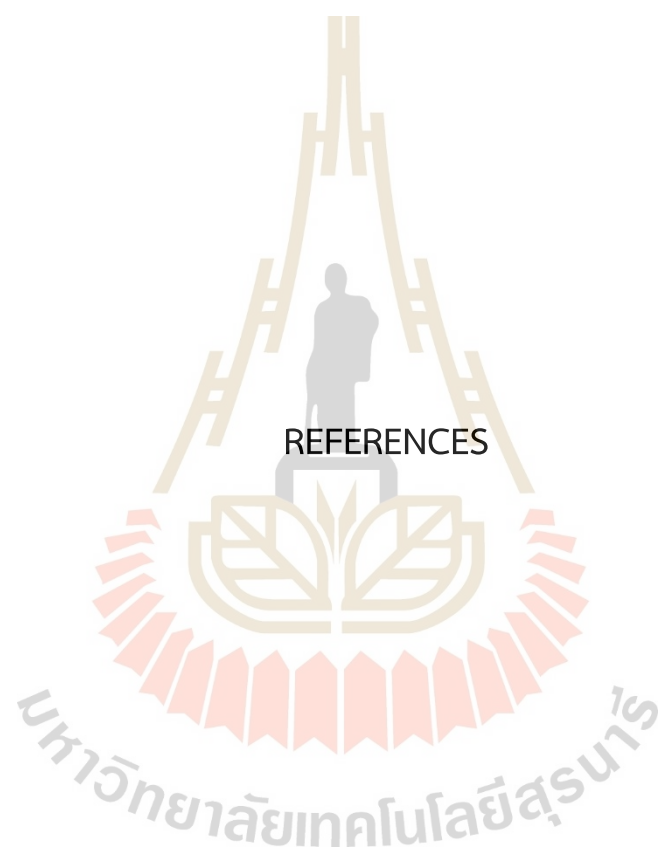
CONCLUSION

This thesis used instrumental analytical methods and computational molecular modeling to study the structure, interaction, thermal, and crystallization behavior of polymer nanocomposite. For the experimental part, PEO is host polymer and there are three types of silicon dioxide filler including silicon dioxide nanoparticles (SiO_2), silicon dioxide nanoparticles treated with silane coupling agents (Sil-SiO_2) and silicon dioxide nanoparticles surface modified with amino group (A-SiO_2). Then compare with MMT and POSS which are silica-based nanofiller. From POM result, spherulite growth rate, G_0 , decreases with increasing SiO_2 content. SiO_2 and A-SiO_2 NPs are aggregate while Sil-SiO_2 can disperse perfectly. From DSC studies, the half-time ($t_{1/2}$) of non-isothermal crystallization increases with adding MMT. Thus, MMT seems to act as good retarding agents for PEO assumed that intercalation occur. For SAXS data, SiO_2 and surface-modified SiO_2 show no peak may because the dominant contrast in these systems between the silica and the polymer.

For simulation, we propose the method of Monte Carlo simulation of coarse-grained polymer and filler model with different shape (nanostick, nanoplate and nanosphere) to study the structural formation and crystallization characteristics of polyethylene nanocomposites. The results imply that the PNCs filled with the nanofillers of planar surface, i.e., the nanoplate and nanostick, can induce faster crystallization and help to form better ordered structures. Due to the larger cross-section area, nanoplate exhibits more effective than nanostick to induce ordered structure formation. In contrast, PE nanocomposites filled with nanosphere (nanofiller with curve surface) exhibit slower crystallization with a lower amount of *trans* conformation, as a result, adopt more disordered orientation and form less ordered structures.

A series of Monte Carlo (MC) simulation of coarse-grained models were performed to investigate structures and dynamic properties of PE melts confined between two interactive solid walls with different polymer-wall interaction. The existence of the walls exhibits the following features. For PE films with stronger polymer-wall interaction, densities in the bulk area are reduced and chains prefer to remain near the wall surface. Anisotropy is greater for bond and chain orientation, particularly when oriented parallel to the wall surface. The polymer-wall interaction causes more shape and size distortion, particularly when the chain is oriented perpendicular to the interface. For films with stronger polymer-wall interaction, polymers adopt a more gauche conformation and worse chain packing. The confined films exhibit changed in properties related to the polymer-wall interaction, including molecular size and shape, bond and chain orientation, and energetics, near the wall surface. For dynamic properties, chains in the inner region have relatively faster chain mobility due to lower density. Chain dynamic decreases significantly due to attractive interaction from the wall surface.

In order to construct, equilibrate, and validate the amorphous PPO models at the bulk density, this work demonstrates a multiscale molecular modeling technique. Lattice Monte Carlo simulation of coarse-grained PPO chains and energy minimization for reverse-mapping to fully atomistic models were used to examine amorphous PPO structures at the bulk density. Monte Carlo simulation of CG model of PPO mapped on the $2nd$ lattice at the bulk density were generated and fully equilibrated. After the reverse-mapping back to the fully atomistic models, chain dimension, conformational statistics, structural, thermodynamic properties and X-ray/Neutron scattering were determined. Comparison of these properties with experimental data are in reasonable agreement. The addition of LiSCN and KSCN salt implies that smaller radius Li^+ ions show faster diffusion than K^+ . On the other hand, K^+ exhibits stronger solvation structure than Li^+ .



REFERENCES

REFERENCES

- Abe, A., Hirano, T., and Tsuruta, T. (1979). Conformational Energies and the Random-Coil Configuration of Poly(oxypropylene). *Macromolecules* 12(6), 1092-1100.
- Abe, A., Jernigan, R. L., and Flory, P. J. (1966). Conformational Energies of n-Alkanes and the Random Configuration of Higher Homologs Including Polymethylene. *Journal of the American Chemical Society* 88(4). 631-639.
- Ahlstrom, P., Borodin, O., Wahnström, G., Wensink, E. J. W., Carlsson, P., and Smith, G. D. (2000). Molecular-dynamics simulation of structural and conformational properties of poly (propylene oxide). *Journal of Chemical Physics* 112, 10669-10679.
- Ajayan, P., Schadler, L. S., and Braun, P. V. (2003). Nanocomposite Science and Technology, Wiley, New York.
- Allegra, G., and Raos, G. (2008). Theories and Simulations of Polymer-Based Nanocomposites: From Chain Statistics to Reinforcement, *Progress in Polymer Science* 33(7), 683-731.
- Anderson, B. J., and Zukoski, C. F. (2010). Rheology and Microstructure of Polymer Nanocomposite Melts: Variation of Polymer Segment-Surface Interaction, *Langmuir* 26(11), 8709-8720.
- Barrera, C. S., and Cornish, K. (2022). Fly ash as a potential filler for the rubber industry, *Handbook of Fly Ash*, 763-792.
- Baschnagel, J., and Binder, K. (1995). On the Influence of Hard Walls on Structural Properties in Polymer Glass Simulation. *Macromolecules* 28, 6808-6818.
- Baschnagel, J., Binder, K., Doruker, P., Gusev, A., Hahn, O., Kremer, K., Mattice, W. L., Muller-Plathe, F., Murat, M., Paul, W., Santos, S., Suter, U. W., and Tries, V. (2000). Bridging the gap between atomistic and coarsegrained models of polymers: status and perspectives. *Advances in Polymer Science* 152, 41-156.
- Billmeyer, F. W. (1984). Textbook of polymer science. (3rd ed). John Wiley & Sons, New York.

- Bitsanis, I. A., and Hadziioannou, G. (1990). Molecular dynamics simulations of the structure and dynamics of confined polymer melts. *Journal of Chemical Physics* 92, 3827-3847.
- Bitsanis, I. A., and Brinke, G. T. (1993). A lattice Monte Carlo study of long-chain conformations at solid-polymer melt interfaces. *Journal of Chemical Physics* 99, 3100-3111.
- Bolodin, O., Douglas, R., Smith, G. D., Trouw, F., and Petrucci, S. (2003). MD Simulations and Experimental Study of Structure, Dynamics, and Thermodynamics of Poly(ethylene oxide) and Its Oligomers. *The Journal of Physical Chemistry B* 107, 6813-6823.
- Brazhnik, P. K., Freed, K., and Tang, H. (1994). Polymer melt near a solid wall. *Journal of Chemical Physics* 101, 9143-9154.
- Brinke, G., Ausserre, D., and Hadziioannou, G. (1988). Interaction between plates in a polymer melt. *Journal of Chemical Physics* 89, 4374-4380.
- Bruce, P. G. (1995). Solid state electrochemistry. (1sted). United Kingdom: Cambridge University Press.
- Chabane, H., Livi, S., Duchet-Rumeau, J., and Francois Gerard, J. (2022). New Epoxy Thermosets Organic-Inorganic Hybrid Nanomaterials Derived from Imidazolium Ionic Liquid Monomers and POSS. *Nanomaterials* 12(550), 1-20.
- Chen, C. M., and Higgs, P. G. (1998). Monte-Carlo simulations of polymer crystallization in dilute solution, *Journal of Chemical Physics* 108, 4305-4314.
- Chen, C. X., Depa, P., Sakai, V. G., Maranas, J. K., Lynn, J. W., Peral, I., and Copley, J. R. D. (2006). A comparison of united atom, explicit atom, and coarse-grained simulation models for poly(ethylene oxide). *Journal of Chemical Physics* 124(23), 234901.
- Chintapalli, S. (1996). Structural characterization of polymer-salt complexes and the role of plasticizers in ionic transport. Ph. D. Dissertation, University of Oklahoma Graduate College, USA.

- Cho, J., and Mattice, W. L. (1997). Estimation of Long-Range Interaction in Coarse-Grained Rotational Isomeric State Polyethylene Chains on a High Coordination Lattice. *Macromolecules* 30(3), 637-644.
- Coleman, J. N., Khan, U., and Blau, W. J. (2006). Small but Strong: A Review of the Mechanical Properties of Carbon Nanotube–Polymer Composites, *Carbon* 44(9), 1624-1652.
- D'Haese, M., Langouche, F., and Van Puyvelde, P. (2013). On the Effect of Particle Size, Shape, Concentration, and Aggregation on the Flow-Induced Crystallization of Polymers, *Macromolecules* 46(9), 3425-3434.
- Dias, B. F., Plomp, L., and Veldhuis, J. B. J. (2000). Trends in polymer electrolytes for secondary lithium batteries. *Journal of Power sources* 88, 169-191.
- Dickman, R. J. (1992). Equation of state of two-dimensional lattice chains at the theta point. *Journal of Chemical Physics* 96(2), 1516-1522.
- Doruker, P., Rapold, R. F., and Mattice, W. L. (1996). Rotational isomeric state models for polyoxyethylene and polythiaethylene on a high coordination lattice. *Journal of Chemical Physics* 104, 8742.
- Doruker, P., and Mattice, W. L. (1998). Simulation of Polyethylene Thin Films on a High Coordination Lattice. *Macromolecules* 31(4), 1418-1426.
- Flandin, L., Brechet, Y., J., and Caviale, Y. (2001). Compos, Electrically Conductive Polymer Nanocomposites as Deformation Sensors, *Composites Science and Technology* 61(6), 895-901.
- Flory, P. J. (1969). *Statistical Mechanics of Chain Molecules*, Wiley, New York.
- Flory, P. J. (1989). *Statistical Mechanics of Chain Molecules*. Hanser-Gardner, Cincinnati, Ohio.
- Fu, S., Sun, Z., Huang, P., Li, Y., and Hu, N. (2019). Some Basic Aspects of Polymer Nanocomposites: A Critical Review, *Nano Materials Science* 1(1), 2–30.
- Fujiwara, S., and Sato, T. (1999). Molecular dynamics simulation of structure formation of short chain molecules, *Journal of Chemical Physics* 110, 9757-9764.
- Genies P. G. D. (1979). *Scaling Concepts in Polymer Physics*. Cornell University Press, Ithaca and London.

- Hertanto, A., and Dickman, R. (1990). Equation of state of athermal lattice chains: Effects of polydispersity. *Journal of Chemical Physics* 93, 774-778.
- Hirano, T., Khanh, P. H., and Tsuruta, T. (1972). Deuterated epoxides and their polymers. III. NMR study of poly(trans-propylene oxide-1-d) in various solvents: a preliminary report. *Die Makromolekulare Chemie* 153, 331-336.
- Hu, W. (2000). The melting point of chain polymers. *Journal of Chemical Physics* 113, 3901-3908.
- Jung, G. Y., Choi, J. H., and Lee, J. K. (2015). Thermal behavior and ion conductivity of polyethylene oxide/polyhedral oligomeric silsesquioxane nanocomposite electrolytes. *Advances in Polymer Technology* 34(21499), 1-6.
- Kawamata, M., and Yamamoto, T. (1997). Molecular dynamics simulation of surface ordering in liquid n-alkanes. *Journal of the Physical Society of Japan* 66, 2350-2354.
- Koo, J. H. (2006). Polymer Nanocomposites. In *Nanoscience and Technology*. McGraw-Hill, New York.
- Kumar, S. K., Vacatello, M., and Yoon, D. Y. (1990). Off-lattice Monte Carlo simulations of polymer melts confined between two plates. 2. Effects of chain length and plate separation. *Macromolecules* 23(8), 2189-2197.
- Kumar, S. K., Ganesan, V., and Riggelman, R. A. (2017). perspective: Outstanding Theoretical Questions in Polymer Nanoparticle Hybrids, *Journal of Chemical Physics* 147(2).
- Kuo, S. W., and Chang, F. C. (2011). POSS related polymer nanocomposites. *Progress in Polymer Science* 36, 1649-1696.
- Kwon, S. J., Kim, D. G., Shim, J., Lee, J. H., Baik, J. H., and Lee, J. C. (2014). Preparation of organic/inorganic hybrid semi-interpenetrating network polymer electrolytes based on poly(ethylene oxide-co-ethylene carbonate) for all-solid-state lithium batteries at elevated temperatures. *Polymer* 55, 2799-2808.
- Lai, P. Y. (1994). Statics and dynamics of a polymer chain adsorbed on a surface: Monte Carlo simulation using the bond-fluctuation model. *Physical Review E* 49, 5420-5430.

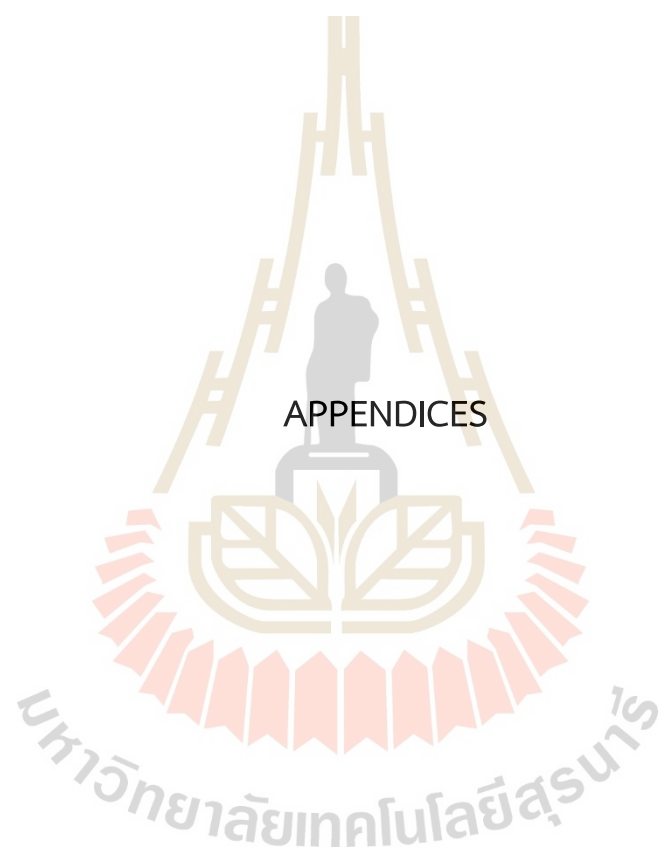
- Li, G., Wang, L., Ni, H., and Pittman, C. U. (2001). Polyhedral Oligomeric Silsesquioxane (POSS) Polymers and Copolymers: A Review. *Journal of Inorganic and Organometallic Polymers and Materials* *11*, 123-154.
- Mandal, T., Huang, W., Mecca, J. M., Getchell, A., Porter, W. W., and Larson, R. G. (2017). A Framework for Multi-Scale Simulation of Crystal Growth in the Presence of Polymers, *Soft Matter* *13*(9), 1904-1913.
- Mark, J. E., and Flory, P. J. (1965). The Configuration of the Polyoxyethylene Chain. *Journal of the American Chemical Society* *87*, 1415-1423.
- Mattice, W. L., and Suter, U. W. (1994). Conformational Theory of Large Molecules: The Rotational Isomeric State Model in Macromolecular Systems, Wiley, New York.
- Mittal, V. (2012). Modeling and prediction of polymer nanocomposite properties, John Wiley & Sons, New York.
- Moniruzzaman, M., and Winey, K. I. (2006). Polymer Nanocomposites Containing Carbon Nanotubes, *Macromolecules* *39*(16), 5194-5205.
- Morales, E. (1996). Polymer Solubility Parameters of Poly(propylene oxide) Rubber from Inverse Gas Chromatography Measurements. *Polymer Journal* *28*(2), 127-130.
- Nie, Y. J., Huang, G. S., Qu, L. L., Wang, X. A., Weng, G. S., and Wu, J. R. (2011). New insights into thermodynamic description of strain-induced crystallization of peroxide cross-linked natural rubber filled with clay by tube model, *Polymer* *52*(14), 3234-3242.
- Nishimoto, A., Agehara, K., Furuya, N., Watanabe, T., and Watanabe, M. (1999). High ionic conductivity of polyether-based network polymer electrolytes with hyperbranched side chains. *Macromolecules* *32*, 1541-1548.
- Pham, T. A., Kweon, K. E., Samanta, A., Lordi, V., and Pask J. E. (2017). Solvation and Dynamics of Sodium and Potassium in Ethylene Carbonate from ab Initio Molecular Dynamics Simulations. *Journal of Physical Chemistry C* *121*(40), 21913-21920.
- Phan, S., Kierlik, E., Rosinberg, M. L., Yethiraji, A., and Dickman, R. (1995). Perturbation density functional theory and Monte Carlo simulations for the structure of hard triatomic fluids in slitlike pores. *Journal of Chemical Physics* *102*, 2141-2150.

- Oguni, N., Maeda, S., and Tani, H. (1973). Structure Analysis of Poly(propylene- β -d oxide) by Proton Nuclear Magnetic Resonance Spectroscopy. *Macromolecules* 6(3), 459-465.
- Quartarone, E., Mustarelli, P., and Magistris, A. (1998). PEO – based composite polymer electrolytes. *Solid State Ionics*. 110, 1-14.
- Pakula, T. J. (1991). Computer simulation of polymers in thin layers. I. Polymer melt between neutral walls-static properties. *Journal of Chemical Physics* 95(6), 4685-4690.
- Pinnavaia, T. J., and Beall, G. W. (2000). *Polymer-Clay Nanocomposites*, Wiley, New York.
- Rapold, R. F., and Mattice, W. L. (1995). New high-coordination lattice model for rotational isomeric state polymer-chains. *Journal of the Chemical Society, Faraday Transactions* 91, 2435-2441.
- Rapold, R. F., and Mattice, W. L. (1996) Introduction of short and long range energies to simulate real chains on the 2nd lattice. *Macromolecules* 29, 2457-2466.
- Rueangsri, K., and Vao-soongnern, V. (2023). Molecular Simulation of the Crystallization of Polyethylene Nanocomposites: The Effect of Surface Affinity of Nanofillers. *Macromolecular Symposia* 409, 2200146.
- Sandler, J., Broza, G., Nolte, M., Schulte, K., and Lam, Y. M. (2003). Crystallization of Carbon Nanotube and Nanofiber Polypropylene Composites, *Journal of Macromolecular Science, Part B* 42, 479-488.
- Sasanuma, Y. (1995). Conformational Analysis of Poly(propylene oxide) and Its Model Compound 1,2-Dimethoxypropane. *Macromolecules*. 28(25), 8629-8638.
- Savoj, R., Agnew, H., Zhou, R., and Paesani, F. (2024). Molecular insights into the influence of ions on water structure. I. Alkali metal ions in solution. *ChemRxiv*. 1-32.
- Sheng, N., Boyce, M. C., Parks, D. M., Rutledge, G. C., Abes, J. I., and Cohen, R. E. (2004). Multiscale Micromechanical Modeling of Polymer/Clay Nanocomposites and the Effective Clay Particle, *Polymer* 45(2), 487-506.

- Shimizu, T., and Yamamoto, T. (2000). Melting and crystallization in thin film of n - alkanes: A molecular dynamics simulation. *Journal of Chemical Physics* 113(8), 3351-3359.
- Solar, M., and Paul, W. (2015). Dielectric α -relaxation of 1,4-polybutadiene confined between graphite walls, *The European Physical Journal E* 38(37), 1-12.
- Solc, K. (1971). Shape of a Random-Flight Chain. *Journal of Chemical Physics* 55, 335-344.
- Song, J. Y., Wang, Y. Y., and Wan, C. C. (1999). Review of gel type polymer electrolytes for lithium – ion batteries. *Journal of Power Sources* 77, 183-197.
- Tao, L., and Perla, B. B. (1999). Theoretical studies of lithium perchlorate in ethylene carbonate, propylene carbonate, and their mixtures. *Journal of The Electrochemical Society* 146, 3613-3622.
- Tokachenko, A. V., and Rabin, Y. (1996). Fluctuation-stabilized surface freezing of chain molecules. *Physical Review Letters* 76(14), 2527-2530.
- Tokachenko, A. V., and Rabin, Y. (1997). Theory of surface freezing of alkanes. *Physical Review E* 55(1), 778-784.
- Theodorou, D. N. (1988). Structure and thermodynamics of bulk homopolymer solid interfaces: a site lattice model approach. *Macromolecules* 21(5), 1400.
- Vao-songnern, V., Ozisik, R., and Mattice, W. L. (2001). Monte Carlo simulation of the structures and dynamics of amorphous polyethylene nanoparticles. *Macromolecular Theory and Simulations* 10, 553-563.
- Wong, M. W., Frisch, M. J., and Wiberg, K. B. (1991). Solvent effects. 1. The mediation of electrostatic effects by solvents. *Journal of the American Chemical Society* 113(13), 4776-4782.
- Yang, H., Zhao, X. J., Li, Z. S., and Yan, F. D. (2009). Molecular Dynamics Simulations on Crystallization of Polyethylene/Fullerene Nanocomposites, *Journal of Chemical Physics* 130(7), 074902.
- Yethiraj, A. (1994). Monte Carlo simulation of confined semiflexible polymer melts. *Journal of Chemical Physics* 101(3), 2489-2497.

- Zhu, P. W., Edward, G., and Nichols, L. (2009). Effect of Additives on Distributions of Lamellar Structures in Sheared Polymer: A Study of Synchrotron Small-Angle X-Ray Scattering, *Journal of Physics D: Applied Physics* 42(24), 245406.
- Zhang, Z., Kulkarni, S., and Wunder, S. L. (2006). Polyethylene Glycol Functionalized Polyoctahedral Silsesquioxanes as Electrolytes for Lithium Batteries. *Journal of The Electrochemical Society* 153(2), A239-A248.





APPENDIX A

PUBLICATION

Rueangsri, K., and Vao-soongnern, V. (2023). Monte Carlo simulation of the crystallization of polyethylene nanocomposites with different shape nanofillers. *Journal of Molecular Liquids* 390, 123134.



APPENDIX B
INTERNATIONAL CONFERENCE I
IUPAC-MACRO 2020+
The 48TH World Polymer Congress: Online Short Talks Sessions
May 16-20, 2021

Development a Multiscale Modeling of Poly(propylene oxide) Electrolytes

Kanokporn Rueangsri¹, Visit Vao-soongnern^{1*}

¹Suranaree University of Technology, Thailand

*Corresponding Author: visit@sut.ac.th

A method to generate the amorphous structures of polymer electrolytes at the bulk density is developed for polymer electrolytes composed of poly(propylene oxide), PPO, with structure of $(\text{CH}_3\text{O}-[\text{CH}_2-\text{CH}(\text{CH}_3)-\text{O}]_n\text{CH}_3)$ mixed with lithium salt. The model starts from the refinement of the rotational isomeric state (RIS) model of PPO determined from ab initio quantum chemistry. Multichains of PPO were then mapped to a coarse-grained model on the second nearest neighbor diamond ($2nd$) lattice. The average nonbonded interactions were treated by the discretized Lennard Jones (LJ) potential. Large amorphous PPO bulks was generated and equilibrated using Monte Carlo algorithm in the discrete space. Fully atomistic amorphous PPO structures can be obtained by the reverse mapping procedure to recover the missing atoms. Lithium salts were added to these initial PPO structures followed by energy minimization step. Molecular dynamic simulation was then employed to investigate the ensemble averaged properties (torsional angle distribution, solubility parameter and atomic pair correlation function and scattering structure factor) and dynamic aspects of ion and polymer mobility

APPENDIX C
INTERNATIONAL CONFERENCE II
National Graduate Research Polymer Conference 2021
(NGRPC2021), Virginia Tech., America: Poster presentation
July 26-29, 2021

Development a Multiscale Molecular Simulation of Poly(propylene oxide) and
Poly(epichlorohydrin) electrolytes

Kanokporn Rueangsri, Visit Vao-soongnern*

Laboratory of Computational and Applied Polymer Science (LCAPS)

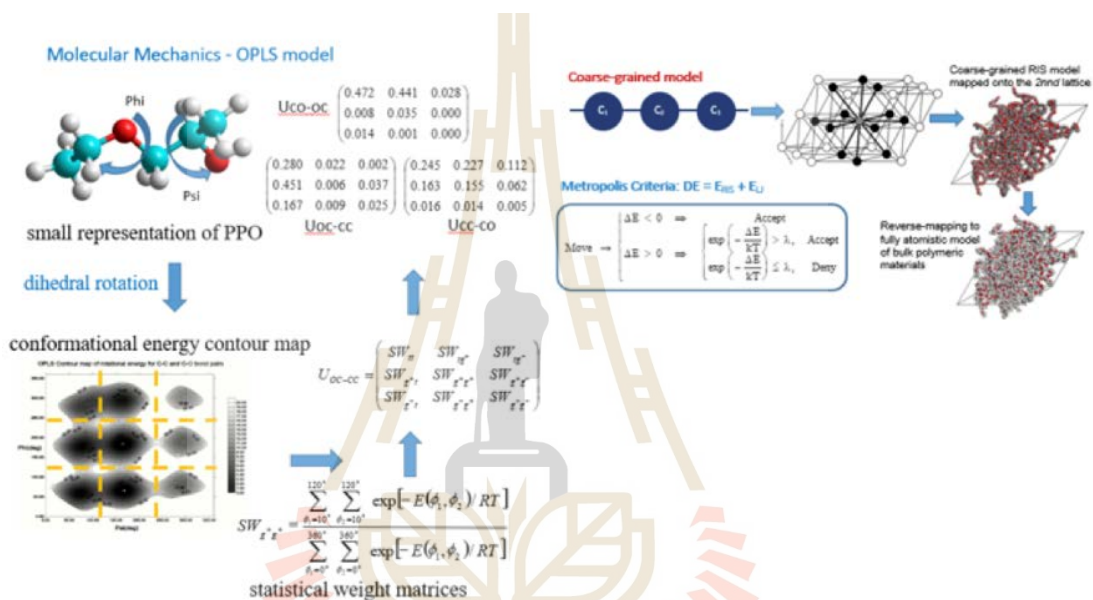
School of Chemistry, Institute of Science, Suranaree University of Technology

Nakhon Ratchasima 30000 THAILAND

Email: kanokporn.nok.nok@gmail.com and visit@sut.ac.th

A multiscale method to model the amorphous structures of molecularly similar polymers at the bulk density is developed for poly(propylene oxide), PPO, and poly(epichlorohydrin), PECH, with the structure of $(\text{CH}_3\text{O}-[\text{CH}_2-\text{CH}(\text{CH}_3)-\text{O}]_n\text{CH}_3)$ and $(\text{CH}_3\text{O}-[\text{CH}_2-\text{CH}(\text{CH}_2\text{Cl})-\text{O}]_n\text{CH}_3)$. The first step was to evaluate the conformational analysis of short representative segments of PPO and PECH from molecular mechanics calculation. These conformational energy maps were then used to construct the statistical weight matrices for the rotational isomeric state (RIS) model of PPO and PECH. Next, these polymers were mapped to the coarse-grained (CG) chains onto the second nearest neighbor diamond (*2nnd*) lattice. The average nonbonded interactions were treated by the discretized Lennard-Jones (LJ) potential of CG beads. Large amorphous PPO and PECH at bulk density were then generated and equilibrated using Monte Carlo algorithm in the lattice space. Finally, fully atomistic amorphous PPO and PECH structures were obtained by the reverse mapping procedure to recover the missing atoms. Lithium salts were added to these initial structures followed by energy

minimization. Molecular dynamic simulation was then employed to investigate the ensemble averaged properties (torsional angle distribution, solubility parameter and atomic pair correlation function and scattering structure factor) and dynamic aspects of ion and polymer mobility. Some features of molecular and material properties were compared between PPO and PECH electrolytes.



CURRICULUM VITAE

I joined the School of Chemistry at Suranaree University of Technology (SUT) in 2017. I entered SUT and passed the examination to study in the Honor Science Program which students can study some Master course level and have to do two research projects for 3 and 8 credits during the junior and senior year, respectively. Since my high school year, I has received the Development and Promotion of Science and Technology Talents Project (DPST) scholarship which is financially supported by the Thai Government until now as a Master's degree student at SUT. At the end of my second year, I was interested in the physical chemistry of polymeric materials and chose this area as my research project. I also took some advanced classes at the Master course level for research preparation such as 1. Computational Nanotechnology 2. Polymer Characterization and 3. Physical Chemistry of Polymer. I started my undergraduate research activities about molecular simulation of the crystallization of polyethylene nanocomposites: The effect of surface affinity of nanofillers (later published in Macromolecular Symposia in 2023).

After finishing my BSc degree with the second-class honor distinction in 2021, I continue my Master's degree in my research group working on molecular simulation and experimental studies of polymer nanocomposite electrolytes for energy storage application. I also got the special budget from DPST scholarship to support my research internship about 3 months at Yamagata University, Japan (the birthplace of OLED screen for Laptop computer). Up to now, I had already presented my thesis work in some international conferences including the IUPAC World Polymer Congress (IUPACMACRO2020+), IUPAC POLY-CHAR (Germany, online), and IUPAC-ICCT (Japan, onsite). In addition, I had already have 4 publications in the referee Journals (2 papers in Q1)